Doctoral Dissertations                                    Dissertations and Theses

March 2016

# (I) Polymer Nanocomposites: Rheology and Processing for Mesoporous Materials and (II) Nanopatterning of Metal Oxides Using Soft Lithography

Rohit Kothari

# (I) POLYMER NANOCOMPOSITES: RHEOLOGY AND PROCESSING FOR MESOPOROUS MATERIALS AND (II) NANOPATTERNING OF METAL OXIDES USING SOFT LITHOGRAPHY

A Dissertation Presented

By

ROHIT KOTHARI

Submitted to the Graduate School of the
University of Massachusetts Amherst in partial fulfillment
of the requirements for the degree of

DOCTOR OF PHILOSOPHY

February 2016

Polymer Science and Engineering

# (I) POLYMER NANOCOMPOSITES: RHEOLOGY AND PROCESSING FOR MESOPOROUS MATERIALS AND (II) NANOPATTERNING OF METAL OXIDES USING SOFT LITHOGRAPHY

A Dissertation Presented

By

ROHIT KOTHARI

Approved as to style and content by:

_____

James J. Watkins, Chair

_____

Samuel P. Gido, Member

_____

H. Henning Winter, Member

_____

David Hoagland, Department Head
Polymer Science and Engineering

DEDICATION

*To the memory of my late grandfather, Mr. Satya Prakash Baldwa.*

*He would have been very happy to see me get a Ph.D.*

# ACKNOWLEDGMENTS

researchers provided insightful comments during the group meetings and were always ready to offer help in the lab.

I would like to thank the facilities directors within the Polymer Science and Engineering Department, John Nicholson, Sekar Thirunavukkarasu, Jacob John, Louis Raboin and Jack Hirsch. Their expertise on characterization techniques is commendable, which proved very useful to me. I would specifically like to acknowledge John Nicholson, who trained me on cleanroom procedures and provided valuable suggestions for my experiments. John also went out of his way to help me fix instruments in Watkins Group. I would like to thank Graduate Program Manager, Lisa Groth and Watkins Group Coordinator, Jo-Ann for reminding me of deadlines pertaining to the Graduate School and assisting me in filing important paperwork.

I thank the NSF's Center of Hierarchical Manufacturing at UMass Amherst and for the financial support through my graduate studies. I would also like to acknowledge the Materials Research Science and Engineering Center at the UMass Amherst for access to the characterization instruments.

Center for UMass / Industry Research on Polymer director, Dr. David Waldman, spent time out of his busy schedule to edit my resume and cover letters. I thank him from the bottom of my heart for the great help he has provided during my job hunt.

I would like to thank Gajin Jeong in Russell Group for all the wonderful memories we have shared helping and caring for each other during the ups and downs in the grad life. Gajin has been an amazing companion and I wish her success and happiness for her future.

I made several good friends during the past five years at UMass. I would especially like to acknowledge Abid Mir, Amulya Gullapalli, Bharath Gopal, Feyza Dundar, Gautam

Nagar, Huong Phan, Mehernosh Dabhoiwala, Murtaza Merchant, Nidhin Joseph, Nihal Kanbargi, Rajiv Neal, Shilpa Saklani and Subrajeet Deshmukh for their friendship. I thank them for making my stay in Amherst enjoyable and I believe I will be in contact with many of them for the lifetime.

Lastly, I would like to acknowledge my parents and family for their unconditional love and support in every decision that I had made till now. I am very grateful to my parents for the sacrifice they had made by letting me come all the way to the United States, knowing that they will hardly be able to meet me once in a year.

# ABSTRACT

(I) POLYMER NANOCOMPOSITES: RHEOLOGY AND PROCESSING FOR
MESOPOROUS MATERIALS AND (II) NANOPATTERNING OF METAL OXIDES
USING SOFT LITHOGRAPHY

FEBRUARY 2016

ROHIT KOTHARI, INTEGRATED DUAL DEGREE (B.TECH.- M.TECH.), INDIAN
INSTITUTE OF TECHNOLOGY (BANARAS HINDU UNIVERSITY), VARANASI

M.S., UNIVERSITY OF MASSACHUSETTS AMHERST

Ph.D., UNIVERSITY OF MASSACHUSETTS AMHERST

Directed by: Professor James J. Watkins

The research in this dissertation is categorized into two parts. The first part is focused on investigation of order-to-disorder transitions (ODT) in nanocomposites of an amphiphilic block copolymer containing various hydrogen-bonded additives, and fabrication of novel mesoporous silica based materials by utilizing such nanocomposites as templates.

Disordered Pluronic®, poly(ethylene oxide) (PEO)−poly(propylene oxide) (PPO)−PEO triblock copolymer upon blending with small molecule additives containing hydrogen-bond-donating functional groups (carboxyl or hydroxyl) result into ordered nanoscale morphologies by preferentially interacting with the hydrophilic PEO chains in the Pluronic®. The dependence of ODT-temperature in these novel Pluronic®/small-molecule-additive complexes on composition, number and type of functional groups on the additive, and the phase behavior of complexes, is explored using rheology.

High loadings of metallic nanoparticles can be achieved in the hydrophilic PEO domain of the Pluronic® by taking the advantage of hydrogen bonding interactions. By utilizing Pluronic®/nanoparticle composites as templates, well-ordered mesoporous/nanoparticle composites (with up to 15 wt% nanoparticles) are fabricated using supercritical carbon dioxide ($scCO_2$) assisted infusion and phase selective condensation of a silica-precursor within the PEO phase of the template. Well-ordered mesoporous silica with such high concentrations of uniformly distributed nanoparticles are advantageous in catalysis, but are elusive using synthetic routes explored in the literature.

Hierarchically porous silica monoliths with high surface area mesopores interconnected through macropores are fabricated using $scCO_2$ assisted phase selective infusion and condensation of a silica-precursor in a Pluronic®/small-molecule-additive template coated on a macroporous template. The surface area of mesoporous silica prepared by the $scCO_2$ infusion process is reported for the first time using nitrogen physisorption experiments. A systematic study of various parameters pertaining to the $scCO_2$ infusion process on the final morphology and surface area of the mesoporous silica is carried out.

In the second part, a soft lithography technique is explored to fabricate nanostructures of inorganic oxides, for example ITO and $TiO_2$, using inks containing crystalline nanoparticles. The technique is evaluated based on its ability to imprint dimensionally stable high-aspect-ratio nanostructures. Rapid imprinting, residual-layer free imprinting and imprinting of sub-200-nm structures is also demonstrated. A layer-by-layer imprinting strategy is developed to realize all-solution processable 3D inorganic nanostructures.

# TABLE OF CONTENTS

# LIST OF FIGURES

CHAPTER 1

INTRODUCTION

## 1.1   Block Copolymers

Block copolymers (BCPs) are comprised of two or more chemically distinct polymer

chains attached covalently. Due to the incompatibility between the chains and the

attachment constraints, BCPs can spontaneously assemble into nano-sized domains

yielding well-ordered equilibrium nanoscale morphologies. The phase behavior of BCPs

with two chemically distinct polymer blocks (ex. A-B, A-B-A, A-B-A-B) is governed by

the relative volume fraction of the blocks and the segregation strength, $\chi N$, where $\chi$ and $N$

are the Flory-Huggins interaction parameter of the blocks and the degree of polymerization

respectively.[1] A typical phase diagram of an A-B type block copolymer is shown in Figure

1.1. Microphase separation into ordered morphologies (lamellar, bicontinuous, cylindrical

and spherical) occurs for sufficiently large $\chi N$.[2,3] The segregation strength required for

microphase separation is a minimum for block copolymers with equal volume fractions of

both blocks, yielding the lamellar morphology. As the blocks become asymmetric in their

volume fractions, segregation strength for microphase separation increases steeply as seen

in Figure 1.1. As the number of blocks increases, the segregation strength required for

microphase separation also increases. While A-B diblock copolymers require a minimum

$\chi N$ of 10.5 for microphase separation[1], A-B-A triblock copolymers require 18. These

predictions are based on the upper critical solution temperature (UCST), where transition

1

from a disordered to ordered (microphase separated) state is obtained upon cooling. The degree of polymerization, *N,* also governs the distance between the domains of a given morphology, also called the d-spacing.
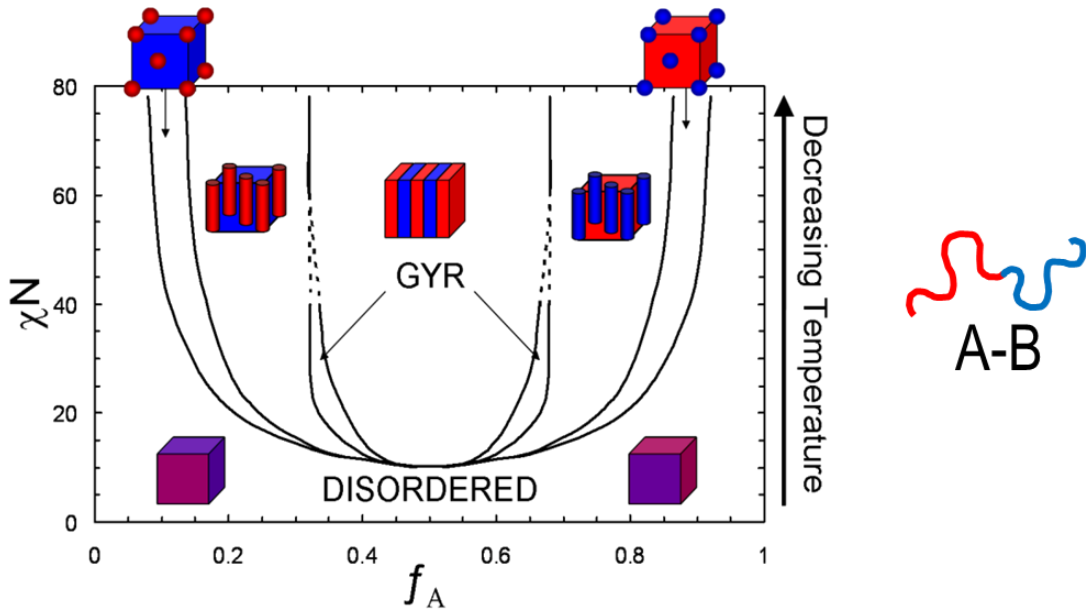


Figure 1.1 Phase diagram of a diblock copolymer predicted using self-consistent mean field theory, adapted from Ref. 3.

Self-assembly of BCP into nanostructured morphologies facilitates their use as materials for the fabrication of high density data storage media,[4-7] templates for nanowires[8] and nanopillers.[9] BCPs have been used as high resolution etch masks and low line edge roughness resist for miniaturized electronics.[10,11] Phase selective condensation of inorganic precursors in microphase separated BCPs has led to mesoporous inorganic materials[12-14]. Phase selective etching of BCPs can yield membranes with well-defined nanopores for size selective filtration and treatment[15,16] Microphase separated BCP/homopolymer blends[17,18] have been shown useful in emerging applications in the field of photonics as tunable

2

photonic band gap materials. Block copolymer domains can sequester nanoparticles with appropriate functionality and geometry to provide nanocomposites with maximum enhancement of effective physical properties. A recent review by Bockstaller et al. provides insight in the specific details and constraints for the formation of BCP/nanoparticle composites.[19]

## 1.2   Block Copolymer Order-to-Disorder Transition Study by Rheology

The temperature at which microphase separated morphology of a block copolymer transitions into a homogeneous melt is considered as order-to-disorder transition temperature ($T_{ODT}$). For a block copolymer showing UCST behavior, disordered state is achieved upon heating an ordered morphology above its $T_{ODT}$. Leibler in his famous 1980 paper[1] predicted that ODT was a weak first order transition which was later experimentally confirmed by Bates in 1990.[20] In the past,   $T_{ODT}$ in block copolymers has been primarily determined by rheology,[21-26] small-angle X-ray scattering (SAXS) [23-26] and small-angle neutron scattering techniques.[20] In scattering experiments, upon heating an ordered morphology above it $T_{ODT}$, the scattering intensity of the primary peak drops to a weak intensity levels corresponding to broad scattering peak from disordered melts. The primary peak width, and shape all show a discontinuity at the ODT. In rheological experiments, the dynamic modulus at low frequencies drops abruptly upon heating across $T_{ODT}$.  Han and co-workers determined $T_{ODT}$ of a triblock copolymer using SAXS and rheological experiments and found both in close agreement.[27] Similarly, Winter and co-workers determined $T_{ODT}$ of styrene-isoprene-styrene block copolymer (Mw=56,000 kg/mol, 24.3 wt% polystyrene and 75.7 wt% polyisoprene) using rheology and confirmed the same with

3

SAXS. Figure 1.2 presents $G'$ and $G''$ dependence on temperature at low frequency ($\omega$=0.1 rad/s) — a 2 to 3 order of magnitude abrupt drop in the $G'$ values at 140 °C signifies ODT.[23]
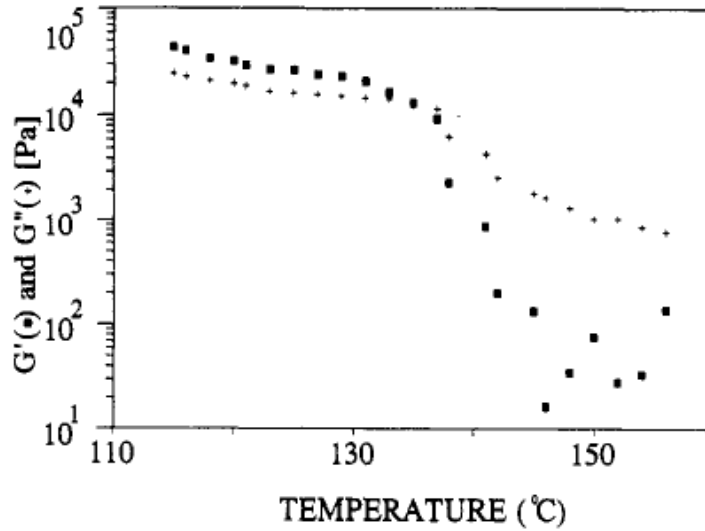


Figure 1.2 Elastic modulus (G') and loss modulus (G'') of styrene-isoprene-styrene triblock copolymer at $\omega$=0.1 rad/s and heating rate of 2 K/min, adapted from Ref. 23.

Other methods which complemented rheology or scattering technique for detection of $T_{ODT}$ used static birefringence measurement[22] and differential scanning calorimetry (DSC).[28,29] Birefringence in the ordered state arise from optical anisotropy within ordered grains whereas disordered melts are optically homogeneous and thus non-birefringent.[30] A very small enthalpy change during the ODT poses difficulty in the detection of $T_{ODT}$ using normal DSC instrument, and it often requires a high resolution DSC measurement.[31] In this research work ODTs in the novel hydrogen-bonded-additive-driven microphase separated BCPs will be explored using rheology.

## 1.3 Mesoporous Silica — Using General Synthetic Route

Porous materials are classified into 3 categories- microporous, mesoporous and macroporous with pore sizes less than 2 nm, between 2 to 50 nm and more than 50 nm, respectively. Porous materials with large specific surface area and well-ordered porosity are important for their utility in catalysis,[32-34] adsorption,[35,36] sensors,[37,38] drug delivery and biomedicine,[39-42] photovoltaics,[43-46] low-K dielectrics,[47] and chromatography.[48,49] Extensive research in the field of high specific area porous materials spur after Beck et al. at Mobil Oil Company in 1992 reported MCM-41 type of periodic mesoporous silicates.[50] The synthetic procedure used ionic surfactants with alkyl chain (for example, hexadecyltrimethylammonium bromide) forming lyotropic mesophase micelles in water as a periodic structure directing agent (template) for silicate network formation from base catalyzed condensation of silica sol-gel precursors. Silica condensation followed by calcination led to silicate structure having hexagonally arranged pores with tunable pore size between 2 to 4 nm. Use of cosolvent organic molecule (for example 1,2,3-trimethylbenzene) helped in swelling the template and increasing pore size up to 10 nm[51,52]. Development of MCM-41 opened new avenues for the use of porous materials in catalysis and filtration applications which were earlier limited by small pore sized (microporous) zeolites.

Further research in this filed lead to the invention of SBA-15 type hexagonally porous silicates with larger pores.[53] The method used long-chain nonionic Pluronic ($PEO_xPPO_yPEO_x$) triblock copolymer surfactants micelles in solutions as structure-directing agents for acid catalyzed condensation of silica precursor (tetraethyl orthosilicate). By varying PEO and PPO block lengths, pore size was tuned between 4 to

10 nm with 3 to 6.5 nm thick pore walls, as shown in Figure 1.3. When 1,2,3-trimethylbenzene was used as a swelling agent, pore size expanded up to 30 nm. Along with size-tunable larger pores, SBA-15 type materials are also more hydrothermally stable compared to MCM-41 owing to their thicker pore walls. Greater hydrothermal stability permits the use of SBA-15 type mesoporous silicates as catalysis supports in harsher environments.
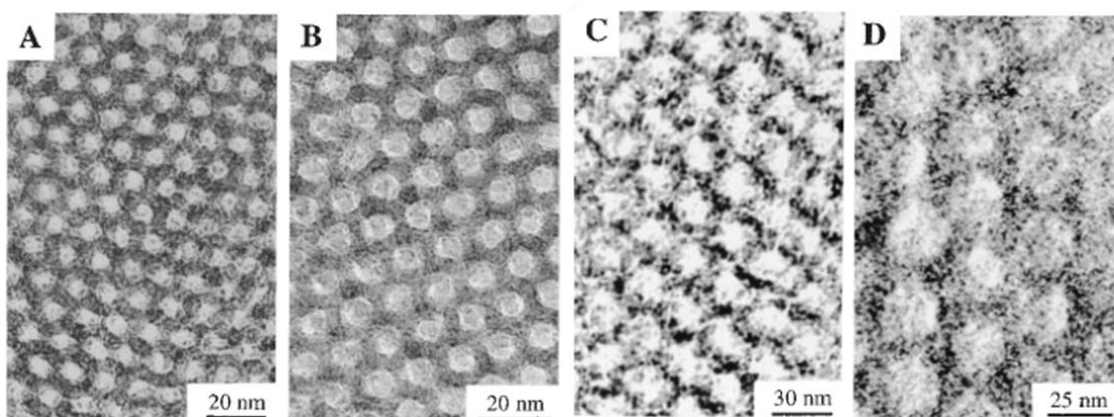


Figure 1.3 TEM images of calcined hexagonal SBA-15 with different average pore size and wall thickness of (A) 6 nm and 5.3 nm, (B) 8.9 nm and 3.1 nm, (C) 20 nm and 4 nm, (D) 26 nm and 4mn, respectively. Adapted from Ref. 53.

## 1.4   Mesoporous Silica — Using Supercritical $CO_2$ Processing

In 2004, Pai and co-workers reported a novel method to fabricate well-ordered robust mesoporous silicates.[54] The approach used block copolymer melts as templates in contrast to the previously known wet synthesis method which involved ionic and nonionic surfactant micellar solutions as structure directing agents for the fabricate MCM-41 and SBA-15 type hexagonally ordered mesoporous silicates respectively. This new strategy involved phase selectively condensed of silica precursor in microphase separated block

copolymer templates using supercritical carbon dioxide (scCO$_2$) as a process medium. The schematics of the process is shown in Figure 1.4. Templates are spin coated from a solutions containing amphiphilic block copolymer and small amount of organic acid catalyst. Upon drying the solvent and subsequent annealing, the block copolymer microphase separates with acid catalyst residing in the hydrophilic phase. The templates are then dilated with scCO$_2$ in the presence of water and organometallic silica precursor. At modest dilation pressures, scCO$_2$ carries silica precursor and water vapor into the template. The infused silica precursor hydrolyze and condense to form silica network only in the hydrophilic domain of the block copolymer where the organic acid catalyst is present. The removal of organic template in the subsequent calcination or reactive ion etching step creates silicate network in the place of hydrophilic phase and pores in the place of hydrophobic phase of the initial microphase separated template. A Transmission electron micrograph of mesoporous silicate prepared by this method is shown in Figure 1.4. Mesoporous silicate films obtained by this method were well-ordered and mechanically robust with indentation hardness of around 0.75 GPa.

The concept was demonstrated using microphase separated templates of PEO$_{106}$-b-PPO$_{70}$-b-PEO$_{106}$ (Pluronic F127), PEO127-b-PPO48-b-PEO127 (Pluronic F108) triblock copolymers and poly(ethylene)-b-PEO (brij surfactants) diblock copolymers. Para-toluene sulfonic acid was used as catalyst which partitions in hydrophilic PEO phase and tetraethyl orthosilicate (TEOS) was used as precursor for silicate.
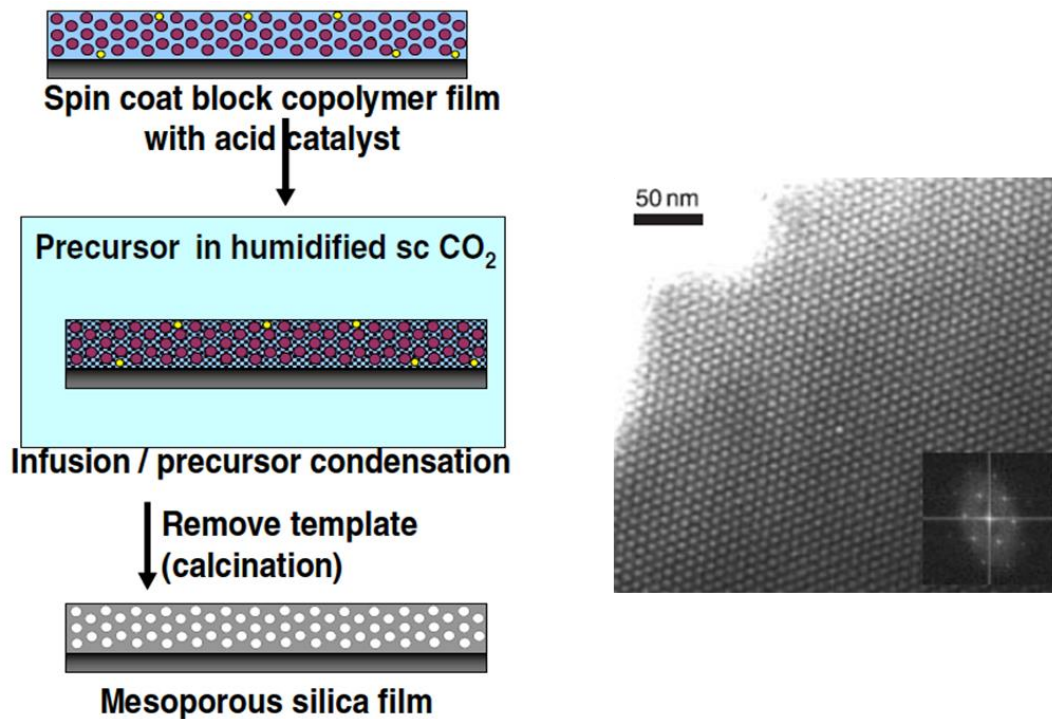
Figure 1.4 Schematic drawing of the fabrication of mesoporous metal oxides in sc $CO_2$ (left), and TEM image of mesoporous silica fabricated (right), adapted from Ref 12.

Mesoporous silica prepared by this method have several advantages over the previously known solution-synthesis methods.[12] 1) scCO$_2$ used as processing medium at modest pressure (123 bars) is a good solvent for organometallic compounds and alcohols allowing the reactant (TEOS) and byproducts (EtOH) to rapidly diffuse in and out of the template during the reaction. This provides fast reaction kinetics and near-complete condensation of the silicate during the infusion step, therefore causing less shrinkage during calcination and yield robust mesoporous silicates. 2) Since the template organization and silica network formation are mutually exclusive, well-defined spherical, cylindrical or bicontinuous pore morphologies can be easily obtained by appropriately choosing block copolymer with corresponding microphase separate morphology. While

8

cylindrical and bicontinuous pore structure provide accessible large surface area suitable for catalysis and filtration applications, closed spherical porosity rendered higher strength in silicate providing the structure suitable for low dielectric constant material, useful as a sergeant between metallic interconnects for reduced resistive capacitance delays and increase efficiency of the device. 3) Pre-organization of template also opens the possibility of its physical or chemical manipulation which can be faithfully replicated in final mesoporous silicate films. For example, chemical patterning of substrates, solvent vapor annealing or external fields can lead to horizontal or vertical oriented block copolymer morphologies which can be used to fabricate mesoporous metal oxide films with highly oriented horizontal or vertical pores, useful in microfluidics and photovoltaics, respectively. Moreover, block copolymer templates can be patterned using photolithography, yielding in patterned mesoporous films suitable for device applications.[55]

## 1.5   Soft Lithography

Soft lithography is a non-conventional lithography technique that involves fabrication of polymeric/inorganic nanostructures using a nanopatterned elastomeric mold. The process starts with fabrication of an elastomeric mold (also called stamp) by casting prepolymer against a nanopatterned hard master, as illustrated in Figure 1.5a. Nanopatterns on hard silicon master are generally made of $SiO_2$, SiN or metals, fabricated using conventional lithography techniques ― photolithography, electron beam writing, etc. From a single hard master several elastomeric molds can be replicated, rendering soft lithography an inexpensive method for fabrication of nanostructures. Figure 1.5b shows schematics of

the imprinting process. The soft elastomeric master is embossed into a low–viscosity crosslinkable resist. Upon embossing the resist rigidified by crosslinking using heat or UV light. Nanopatterning of the resist is achieved upon removing the stamp. Due to its simplicity and ability to effectively pattern sub-50-nm structures on a large area in rapid fashion[56], soft lithography is widely considered as a next-generation lithography technique for inexpensive fabrication of nanopatterns.
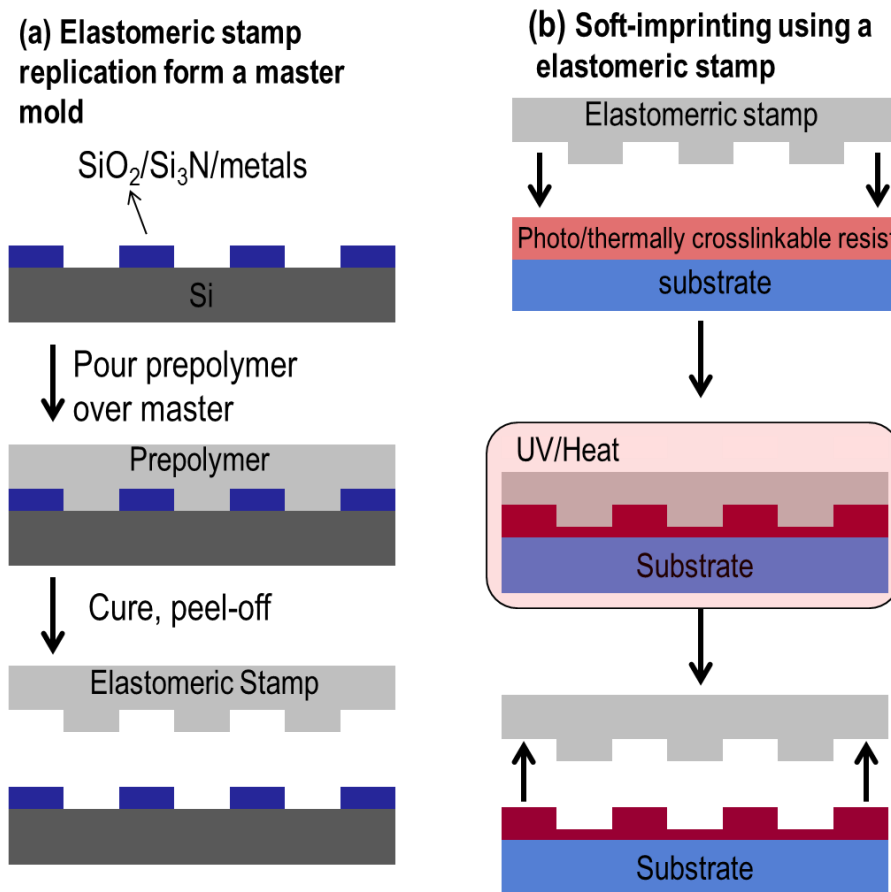


Figure 1.5 Schematic of soft lithography process. (a) Elastomeric stmap fabrications steps using a hard master. (b) Imprinting into a UV/thermally curable resist using elastomeric stamp.

Soft imprinting can also be practiced using a solvent permeable stamp. Fluidity in the resist to be imprinted can be imparted by dilution with a solvent. Upon imprinting,

10

solvent permeates through the elastomeric stamps, such as polydimethylsiloxane[57] or poly(2-methyl-2-pentyne)[58] stamps, leaving behind rigidified solids. A few acronyms used for the solvent-assisted soft imprint lithography are, micromolding in capillaries (MIMIC)[59] microfluidic molding (MM)[60,61] and solvent assisted micromolding (SAMIM).[62,63] Schematics of a solvent-assisted soft imprinting method to fabricate various nanopatterns is shown in Figure 1.6.
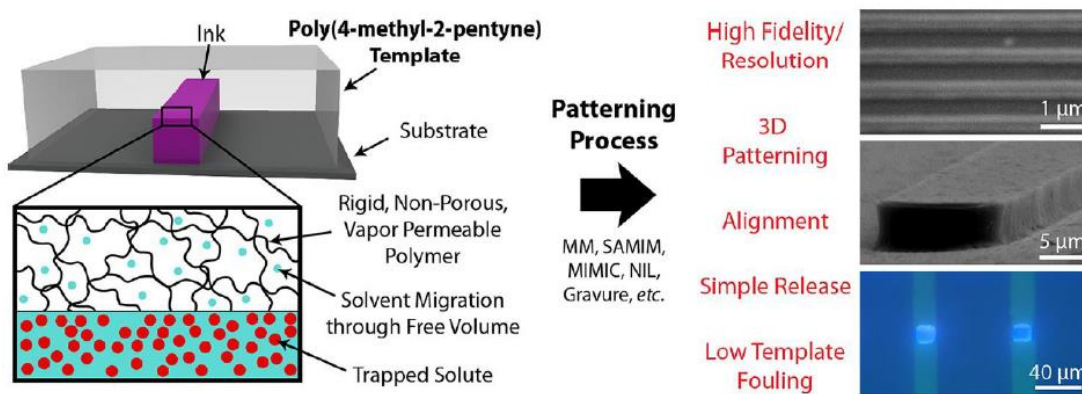


Figure 1.6 Schematics describing solvent-assisted imprinting using inks containing dissolved or suspended stamp-impermeable solids in a stamp-permeable solvent. Adapted from Ref. 58.

## 1.6 Dissertation Overview

This dissertation consists of five Chapters. Chapter 1 (present) provides an introduction to materials and techniques pertaining to this dissertation. In Chapter 2, order-to-disorder transitions in block copolymers containing hydrogen-bonded additives are investigated using rheological experiments. The amphiphilic block copolymer used is initially disordered and ordered morphologies are obtained upon blending it with various small molecule additives containing hydrogen-bond donating sites. Dependence of order-to-disorder transition temperature on additive loading, number of functional groups on the

additive molecule, and type of functional groups on the additive molecule is explored. Few unique aspects of the phase behavior of novel microphase separated block copolymer/small-molecule-additive are explored using rheology and X-ray scattering.

In chapter 3 supercritical carbon dioxide infusion method to make mesoporous silica is utilized to fabricate highly loaded mesoporous silica/metallic nanoparticle composites with uniformly distributed nanoparticles. Such nanocomposites possess tremendous utility in heterogeneous catalysis. In chapter 4, hierarchically porous silica monoliths are fabricated using supercritical carbon dioxide infusion method. The fabricated hierarchically porous silica contain well-ordered mesopores interconnected through macropores. Such dual porosity silica are advantageous in catalysis and separation because of enhance mass transport offered by the presence of macropores. Surface area and porosity of the mesoporous silica fabricated using $scCO_2$ is evaluated.

In chapter 5, a solution-based soft nanoimprint lithography technique is used to fabricate 1D, 2D and 3D dimensionally stable crystalline metal oxide nanostructures. A solvent permeable patterned PDMS stamp is used to imprint inks containing crystalline nanoparticles in an organic solvents. Composition and physical properties of imprinted metal oxides are altered by doping crystalline nanoparticle based inks with UV/thermally curable metal oxide precursors. Thermally stable highly crystalline nanostructures are imprinted. High-aspect ratio nanostructures and sub-100-nm features are demonstrated. The technique is also, optimized to imprint nanostructures in a rapid fashion. Methods to fabricate residual-layer free structures without resorting to dry-etching are demonstrated. The technique is further extended to create 3D nanostructures by deploying a completely solution processable layer-by-layer imprint strategy.

CHAPTER 2

RHEOLOGICAL STUDY OF ORDER-TO-DISORDER
TRANSITIONS AND PHASE BEHAVIOR IN HYDROGEN-
BONDED BLOCK COPOLYMER/SMALL MOLECULE ADDITIVE
COMPLEXES

## 2.1 Introduction and Objectives

Block copolymers (BCPs) have been used as phase selective etch masks to develop nanopatterns in an underlying inorganic substrate.[11] These nanopatterns are used in creation of device components, such as transistors,[64] capacitors[65] and high density data storage media.[7] To increase the efficiency of devices based on these nanostructures, higher integration densities are required, which demands smaller d-spacing of the block copolymer being used. Smaller d-spacing corresponds to smaller degree of polymerization ($N$). The increasing demand for high density microelectronic structures and the associated well-ordered morphologies with small features (3-15 nm) requires increasing $\chi$, to compensate for small $N$, in order to maintain a sufficiently large $\chi N$.

Watkins and co-workers have taken the advantage of hydrogen bonding interactions to induce order in otherwise disordered low molecular weight BCPs. Well-ordered microphase separated morphologies with d-spacing between 10-15 nm were achieved, which are useful for above mentioned applications. The strategy used is elaborated below.

**Block Copolymers Containing Hydrogen-Bonded Additives.** Hydrogen bonding is one of the key mechanisms behind the formation of various supramolecular structures from small moieties. Taking advantage of versatility, directionality, and stability of the interactions, hydrogen bonding between small molecules building blocks has enabled researchers to create supramolecular assemblies exhibiting liquid crystalline behavior.[66-71] Hydrogen bond assisted liquid crystalline supramolecular assemblies have also been achieved in blends containing polymers and mesogenic[72-76] or nonmesogenic[77] small molecules. Hierarchical assemblies at two different length scales have been demonstrated by the means of selective hydrogen bonding between a mesogenic or amphiphilic additive molecules and a specific block of the block copolymers.[78-85] Disorder-to-order[82] and order-to-order[78-83] transitions in the block copolymer are observed with the additive molecules and temperature, using X-ray scattering. Owing to the mesogenic or amphiphilic nature, these additive molecules further self-organize within the host domain of the microphase separated block copolymers to result in composition dependent hierarchical morphologies.

Recently, it has been shown that multiple-hydrogen-bond-donating small molecules can selectively associate with a particular block and induce microphase separation in otherwise disordered BCPs.[86] Molecules used are nonmesogenic and nonamphiphilic, therefore no substructures are formed within the resulting microphase separated domains and the morphologies native to the block copolymers are preserved. The resulting well-ordered morphologies exhibit feature sizes of less than 15 nm, which is important for applications requiring small domains.

Block copolymers of PEO and PPO are commercially available under the trade name Pluronic®. The hydrophobic PPO block and the hydrophilic PEO block give the

molecule an amphiphilic nature typical of a nonionic surfactant. Pluronic® block copolymers are usually disordered at room temperature and above in the melt due to their low molecular weight and weak repulsive interaction between PEO and PPO blocks. By taking advantage of the hydrogen bonding interaction, Watkins and co-workers have induced microphase separation in Pluronic® BCPs by blending it with homopolymers,[87] small molecule additives[86] and functionalized nanoparticles.[88] All of these additives bear hydrogen bond donating sites which selectively interact with the hydrophilic PEO blocks, increasing the effective $\chi$ parameter and thus leading to microphase separation. The strategy provides a method to induce order in BCPs with low molecular weight and week incompatibility between the blocks. The selective incorporation of the hydrogen bonding additive imparts additional functionality to the material along with ordered morphology.

Upon gradual addition of hydrogen bonding small molecule additives, such as benzenehexacarboxylic acid or hexahydroxybenzene, into Pluronic® F108, transition from disordered morphology to cylindrical morphology was observed through small angle X-ray scattering (SAXS),[86] as shown in Figure 2.1. Further addition of additive induced the transition from cylindrical to spherical morphologies, followed by macrophase separation of the additive at a very high loading (>40 wt % in case of benzenehexacarboxylic acid). By comparing full width at half-maximum of the primary peaks of the SAXS profiles and domain spacing for ordered cylindrical morphologies, it was shown that that additives bearing carboxyl functional groups compared to hydroxyl groups exhibit a stronger capacity to increase segregation strength and induce microphase separation. Since the microphase separation is driven by the addition of the small molecule component, segregation strength and consequently the order-to-disorder transition temperature ($T_{ODT}$)

will naturally depend upon the strength and the number of hydrogen bond interactions presented by the additive and the loadings of the small molecule additive into the BCP. Studying phase behavior (order-disorder transitions) and quantifying $T_{ODT}$ in these novel hydrogen-bonded-additive-driven microphase separated BCPs is of particular interest and is the aim of this research.
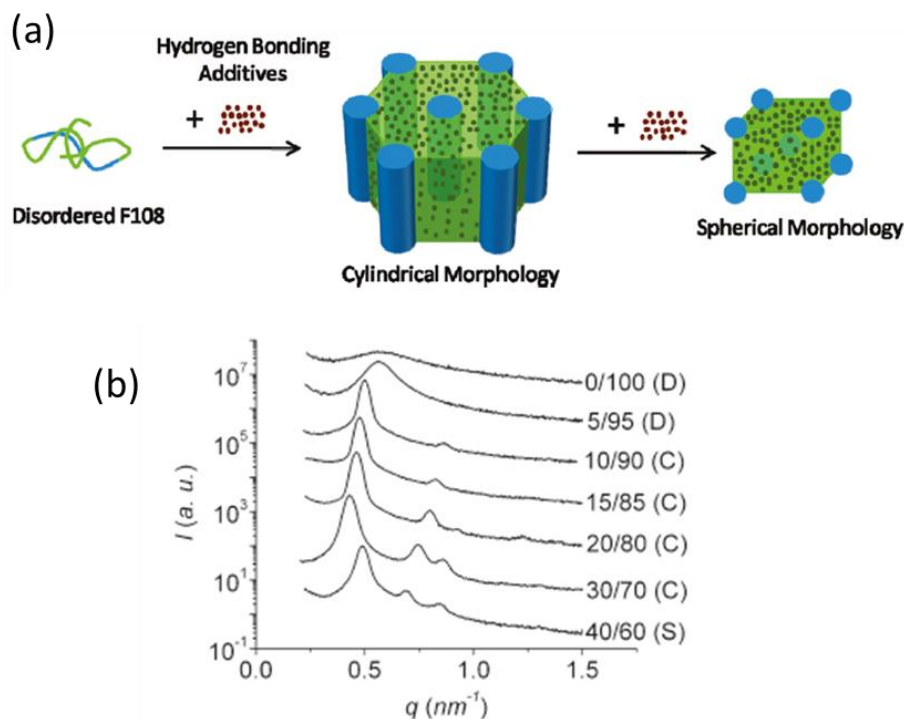


Figure 2.1 (a) Schematic representation of additive driven assembly of disordered Pluronic® F108 induced by blending with hydrogen-bond-donating small molecule additives, additive selectively interacts with poly(ethyleneoxide) (PEO; green chain) to from matrix and poly(propyleneoxide) PPO (blue chains) from cylinders or spheres (b) Small angle X-ray scattering profiles of blends of F108 and benzene-1,2,3,4,5,6-hexacarboxylic acid as a function of composition at 80 °C. The disordered state and cylindrical and spherical morphologies of the blends are denoted by D, C, and S, respectively. Adapted from Ref. 86.

**Objectives of this research.** In this study we will use rheology to explore the temperature-dependent phase behavior of Pluronic® F108 (F108) over a broad range of

small molecule additive types and loadings. The phase behavior shall be essentially different from that of neat BCP due to the additional component, small molecule, which drives microphase separation via hydrogen bonding interaction. To determine $T_{ODT}$, microphase separated morphologies of F108 containing small molecule additives will be subjected to viscoelastic measurements with increasing temperature. A set of small molecule additives with an identical core but systematic variance in the number of carboxyl functional groups will be utilized to explore the dependence of $T_{ODT}$ upon the number of hydrogen bonding sites presented by the additive. The change in $T_{ODT}$ by changing the type of functional group on the additive will be studied by blending additives with similar structure, but different functionality, carboxyl or hydroxyl. A schematics of ordered morphologies formed upon blending F108 with hydrogen bonding small molecule additive and a schematics of disordering during a rheological experiment for the determination of $T_{ODT}$ is shown in Figure 2.2.[89]
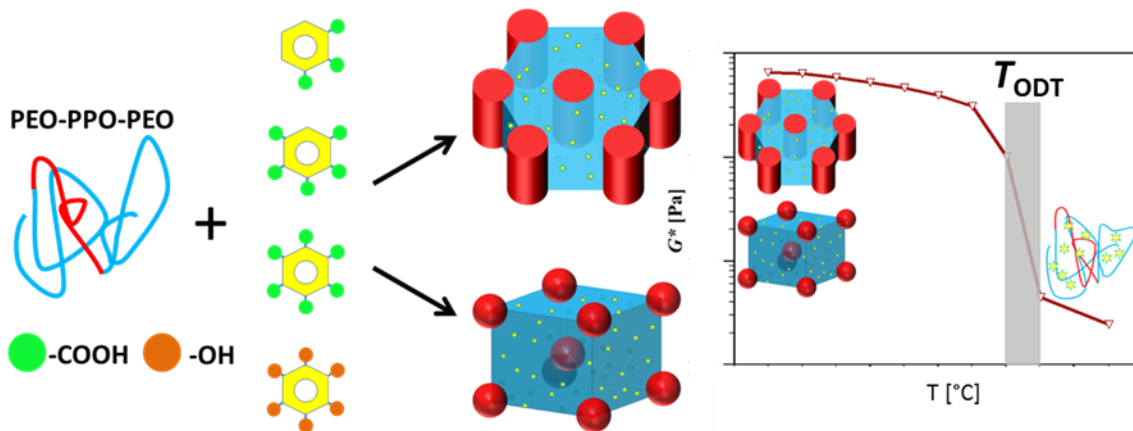


Figure 2.2 Schematics of formation of ordered cylindrical and spherical morphologies upon blending small molecule additives containing carboxyl and hydroxyl functional group, and schematics of disordering during a rheological experiment in which complex modulus ($G^*$) is plotted against temperature for the determination of $T_{ODT}$. Reprinted from Ref 89. Copyright 2014 American Chemical Society

## 2.2   Experimental Section

### 2.2.1   Materials

Figure 2.3 shows chemical structure of various small molecule additives and PEO-PPO-PEO Pluronic® F108 (F108) that are used in this study. F108 (donated by BASF) comprise of a hydrophobic PPO middle block of $M_w$ ~3 kg/mol and hydrophilic PEO side blocks that constitutes 80 wt % of the molecule. The polydispersity of F108 as determined by gel permeation chromatography was 1.2. Polyethyleneoxide (PEO) homopolymer ($M_w$ = 20 kg/mol) was obtained from Sigma-Aldrich. Small molecule additives,  benzene-1,2,3,4,5,6,-hexacarboxylic acid (BHCA), benzene-1,2,3,4,5-pentacarboxylic acid (BPCA), benzene-1,2,3-tricarboxylic acid (123BTCA) hydrate, benzene-1,3,5-tricarboxylic acid (135BTCA) and benzene-1,2,3,4,5,6-hexol (HHB) were purchased from TCI America.  Hexaketocyclohexane octahydrate, phthalic acid and benzoic acid were purchased from Sigma-Aldrich. Reagent grade water and N,N-Dimethylformamide (DMF) used as solvents were obtained from  Fisher Scientific. Hexaketocyclohexane hydrate and 123BTCA were at 100 °C under vacuum for several hours to remove water crystallization. Otherwise, the materials and solvents were used as received.

### 2.2.2   Sample Preparation

Appropriate amounts of F108 and small-molecule-additives were blended by solution casting from a 1:1 weight ratio mixtures of water and DMF. Clear solutions of 15 wt% solids were transferred to a 60 mm diameter glass Petri dish, heated to 60 °C for 48 hours, and further dried in vacuum at 60 °C for 24 hours to remove residual solvent. Batch

sizes and preparation protocols were strictly adhered to minimize deviations that might occur due to variation in solvent evaporation rate and thermal history. A blend containing 65 wt% PEO and 35 wt% BHCA was also prepared using the same protocol.

A blend represented as $x/y$ is composed of $x$ wt% F108 and $y$ wt% of small-molecule-additive ($x + y = 100$). For the purpose of comparison of $T_{ODT}$ between different F108/additive blends, additives are blended in amounts that maintain equivalent numbers of functional groups per gram of F108. For example, to incorporate 30 milliequivalents carboxyl groups per gram of F108, the amount of BHCA added will be 5 milliequivalents, the amount of BPCA added will be 6 milliequivalents and the amount of 123BTCA added will be 10 milliequivalents. As a consequence, the mass fraction and volume fraction of the additive incorporated per gram of F108 increase accordingly. This volume effect will be discussed further in connection with the experimental results.
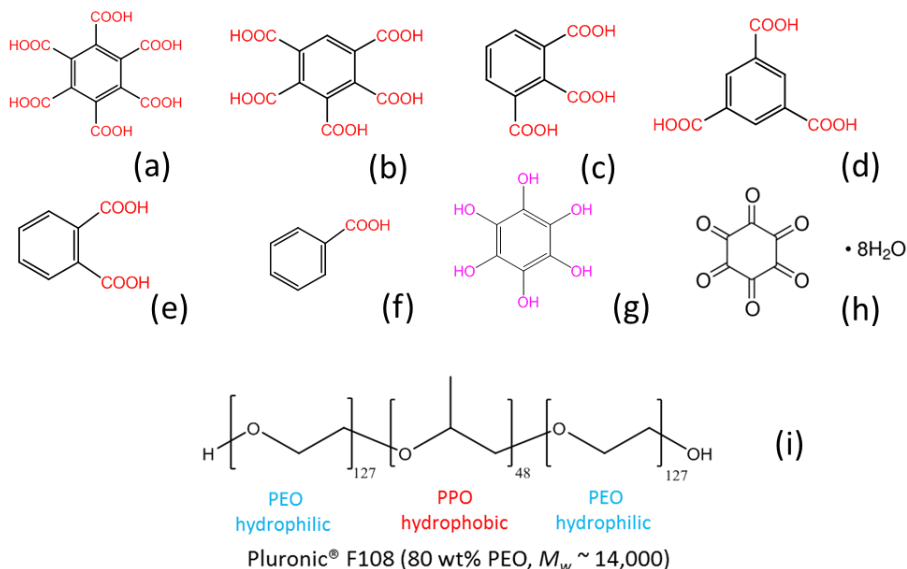


Figure 2.3 (a-g) Additives used in this study : (a) benzene-1,2,3,4,5,6,-hexacarboxylic acid (BHCA), (b) benzene-1,2,3,4,5-pentacarboxylic acid (BPCA), (c) benzene-1,2,3-tricarboxylic acid (123BTCA), (d) benzene-1,3,5-tricarboxylic acid (135BTCA), (e) phthalic acid, (f) benzoic acid, (g) benzene-1,2,3,4,5,6-hexol (HHB); (h) hexaketocyclohexane octahydrate; and (i) Pluronic® F108 (F108). Reprinted from Ref 89. Copyright 2014 American Chemical Society

**2.2.3   Characterization**

Dynamic mechanical measurements were performed on an ARES (Rheometric Scientific) strain-controlled rotational rheometer, using parallel plate fixtures of 25mm diameter. Pellets of dried samples were melted at 60 °C and squeezed between rheometer fixtures to a gap size of 0.6 mm. Small amplitude oscillatory shear (strain amplitude $\gamma$ = 0.01) was applied in the linear viscoelastic regime. To locate ODT, isothermal frequency sweeps over four decades of frequency (0.01 rad/s < $\omega$ < 100 rad/s) were performed at increasing temperature with steps of 5 K. Interactive IRIS (2006) software was used to analyze and plot the rheological data.

Small Angle X-Ray Scattering (SAXS) was performed on Rigaku-Molecular Metrology SAXS equipment using Cu K$\alpha$ radiation having wavelength $\lambda$ = 0.1542 nm. The size of incident beam at sample position was approximately 4 mm in diameter.  A two dimensional detector recorded SAXS patterns in a $q$ range 0.06-1.5 nm$^{-1}$, where the scattering vector is defined as $q$ = $(4\pi/\lambda)\sin\theta$, $2\theta$ being scattering angle. The distance between sample and detector was calibrated using the silver behenate's primary diffraction peak at $q$ = 1.076 nm$^{-1}$. Samples were placed between 2 mm thick steel washers and sealed from both sides using thin kapton film. Experiments were performed by heating samples under vacuum to a fixed temperature using a Linkam hot stage. Isothermal scattering data was circularly averaged and plotted as intensity vs $q$ where intensity was left in arbitrary units. Data are shifted vertically by constant factors to avoid overlap.

Differential Scanning Calorimetry (DSC) was carried out to obtain melting enthalpies of the PEO crystallites present in the blends. Samples weighing ~10 mg were filled into aluminum pans and sealed. Experiments were performed on TA Instruments

Q200 DSC equipped with refrigerated nitrogen cooling system and nitrogen gas purge flow rate of 50 ml/min. Temperature and heat flow were calibrated using indium as a standard. All measurements were conducted in the temperature range of -50 to 80 °C with heating and cooling rate of 10 K/min and 1 K/min respectively. The reported DSC thermograms were measured during second heating cycles.

Thermogravimetric Analysis (TGA). TGA experiments were performed on in air environment on TA instruments TGA Q500.

## 2.3   Results and Discussion

As the hydrogen-bond donating small molecule will interact with PEO segment of F108, before elaborating the phase behavior of Fl08/small-molecule-additive /F108 complexes, we first discuss morphology and rheological behavior of PEO homopolymer blended with small molecule.

### 2.3.1   Morphology and Rheological Behavior of BHCA/PEO Blends

Out of all the small molecules used in this study, BHCA is found to have strongest interaction with PEO, therefore BHCA/PEO blend at different loadings of BHCA is discussed here. Figure 2.4 shows DSC thermograms of BHCA/PEO at 0, 10, 15, 25, and 30 wt% of BHCA loading. The strong hydrogen-bonding interaction of BHCA with PEO suppresses the crystallization of PEO chains, as evident by the decrease in the enthalpy of melting of crystallizable PEO from 179.6 J/g to near zero upon increasing BHCA loading to 30 wt%. As nearly all PEO interacts with BHCA to transform into amorphous state for at 25 and 30 wt% BHCA laoding, prominent glass transition signal appears at around -20

°C (for 25 wt% loading) and -10 °C (for 30 wt% loading). The glass transition temperature of (Tg) -34.63 °C has been reported for neat PEO (20 kg/mol) using more sensitive dynamic mechanical analyzing technique. An increase in Tg is an indication of higher energy required for the mobility PEO chains due to the strong interaction with BHCA.
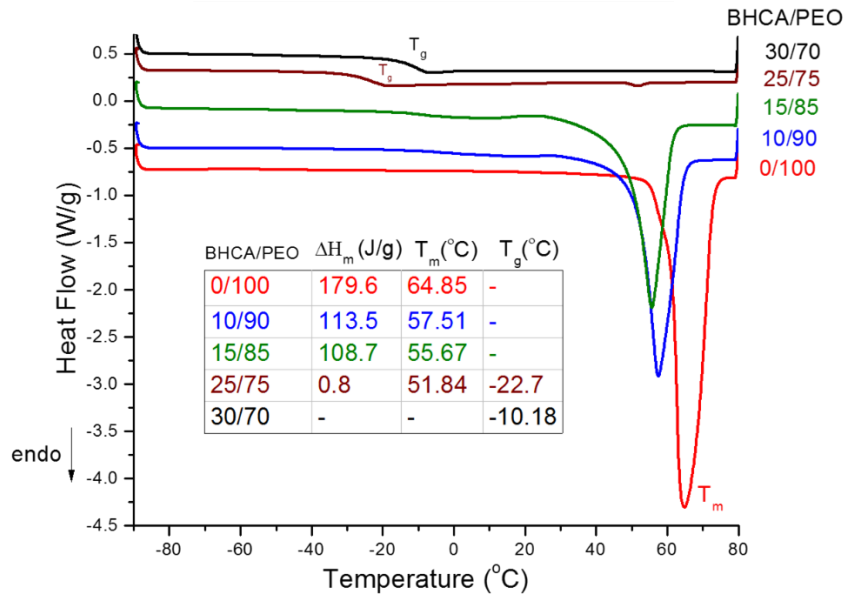


Figure 2.4 Differential scanning calorimetry (DSC) thermograms of BHCA/PEO (wt/wt) blends.
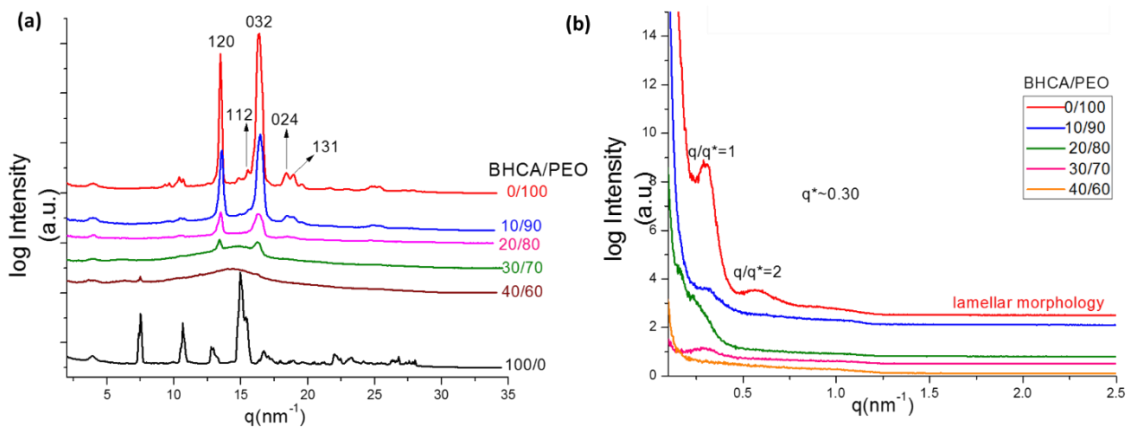


Figure 2.5 (a) Wide-angle X-ray Scattering (WAXS) and (b) Small-angle X-ray scattering (WAXS) of BHCA/PEO (wt/wt) blends. Bragg reflection of PEO are indexed as per Ref. 90.

22

Figure 2.5 shows SAXS and WAXS of BHCA/PEO blends at different loading of BHCA. WAXS data confirms the presence of crystalline PEO in the blends with low loading of BHCA. The gradual decrease in the PEO peaks intensity (for same amount of data collection time and sample thickness) with BHCA loading is another evidence of suppression in PEO crystallization at higher loadings. Crystalline PEO peaks completely disappear at 40 wt% BHCA loading and no hint of crystallization of BHCA was observed up to this concentration. As the content of crystallizable PEO decrease upon adding BHCA, the peaks corresponding to lamellar packing of crystalline sheets vanishes, as seen in SAXS.

Figure 2.6 shows isothermal frequency sweep over four decades for a 35/65 BHCA/PEO blend at 65 °C, slightly above the melting temperature of PEO. Despite of high loading of BHCA, which can form multiple hydrogen-bonded network (alike a covalently bonded crosslinking network in a thermoset), the blend shows liquid like behavior where storage modulus ($G'$) and loss modulus ($G''$) are strongly frequency dependent and $G' < G''$.
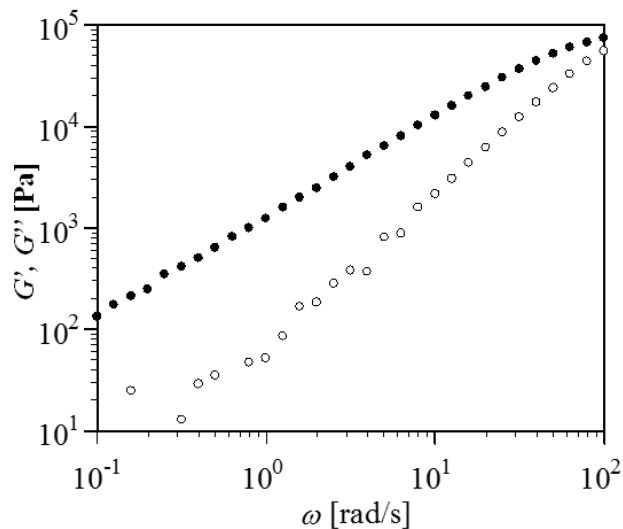
Figure 2.6 Isothermal frequency sweep at 65 °C for a 35/65 BHCA/PEO blend.

Next we discuss ODT and phase behavior of various small molecules with F108. All of the small molecule additives (Figure 2.3), are crystalline at room temperature and show no melting or degradation in the experimental temperature window for this study. We start by elaborating the phase behavior of F108/BHCA in detail to establish generality in these hydrogen-bonded F108/small-molecule-additive block copolymer complexes. Among all additives used here, BHCA induced the strongest segregation in F108. The influence of all other additives on segregation strength will be measured against BHCA by comparing $T_{ODT}$ of their respective blends with F108 to $T_{ODT}$ of F108/BHCA.

### 2.3.2   ODT and Phase Behavior in BHCA/F108 complexes

Figure 2.7 provides SAXS measurements and isothermal frequency sweep on neat F108 at 65 °C, at a temperature slightly above the melting point of the PEO segments. In SAXS, F108 shows a broad hump owing to a disordered morphology. In rheological

measurement the materials shows the characteristic of a melt with $G'$ and $G''$ being frequency dependent and $G'$ being less than $G''$.
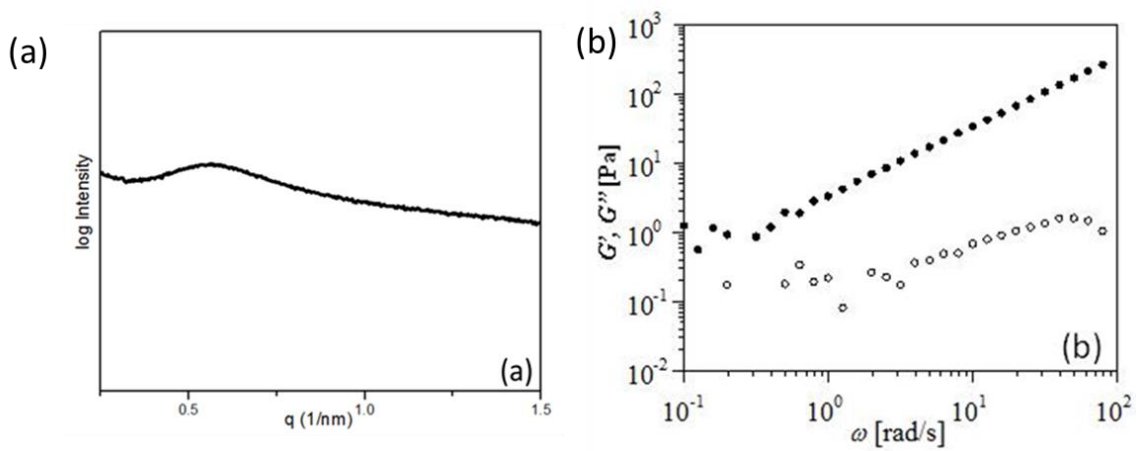


Figure 2.7 (a) SAXS profile at 65 °C for F108 showing a disordered morphology with a broad scattering hump at low q values (b) Isothermal frequency sweep at 65 °C for F108.

As in case of BHCA/PEO blends, the enthalpy of melting of PEO (integrated area under the melting endotherms) decreases upon the addition of BHCA to F108 (inset in Figure 2.8) This dicates the existence of favorable hydrogen bonding interactions, which result in molecular level mixing of the additive with PEO chains in F108, thereby suppressing PEO crystallization. The enthalpy of fusion is normalized to PEO content in the blends; for neat F108 it was found to be 165 J/g of PEO. The percentage crystallinity with respect to neat F108 is calculated and plotted in **Figure 2.8**. For example, upon adding 20 wt % of additive we see around 80% reduction in the crystallizable PEO phase. Owing to the high compatibility between BHCA and PEO, loading of the additive can be further increased to 40 wt % without macrophase separation of the additive in the as prepared sample.
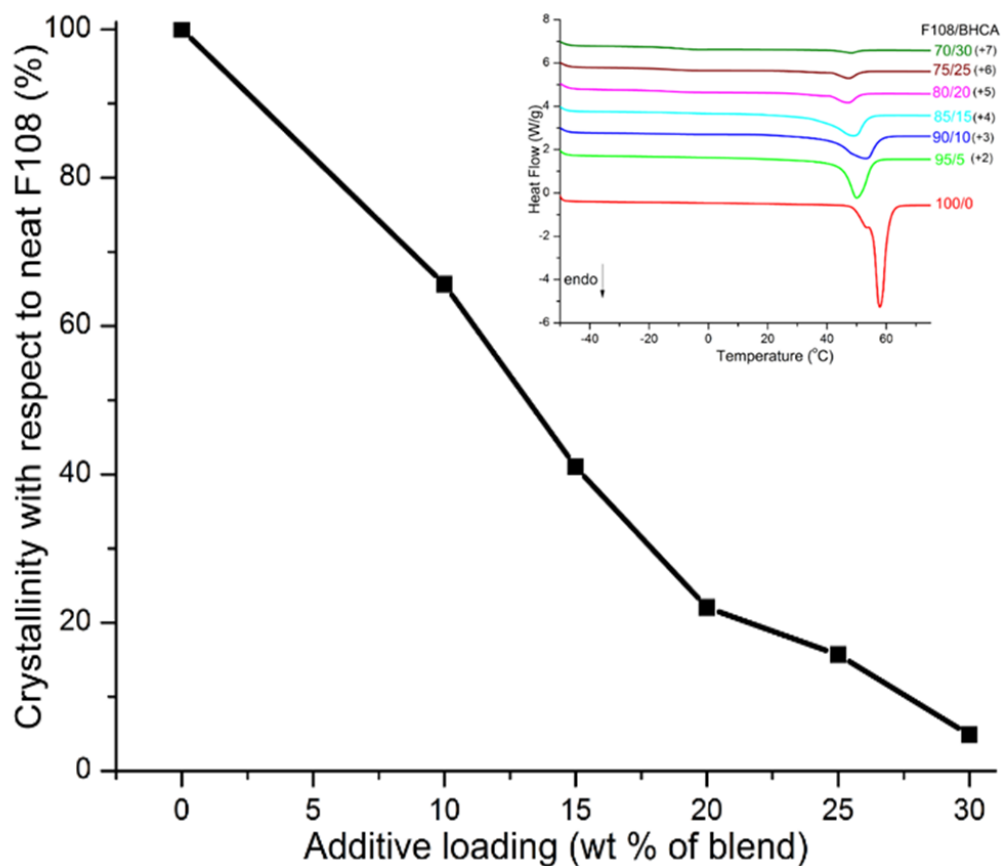
Figure 2.8 The percent crystallinity of PEO in the blends containing F108 and BHCA plotted against the loadings of BHCA in the blends. The percent crystallinity of PEO in the blends is presented with respect to percent crystallinity of PEO in neat F108, which is arbitrarily set to 100%. The inset shows DSC thermograms of the blends. Thermograms except that of neat F108 were shifted vertically by constant factors (indicated in brackets) to avoid overlap. Reprinted from Ref 89. Copyright 2014 American Chemical Society.

The strong interactions between multiple-hydrogen-bond-donating BHCA molecules and multiple-hydrogen-bond-accepting PEO chains persists well above the melting temperature of PEO. The addition of BHCA to the PEO chains increases the repulsion of PEO with the PPO segments and leads to microphase separation by creation of BHCA-PEO microdomains and PPO microdomains. In absence of BHCA, weak repulsion of PEO with PPO upon melting would cause the material be disordered $(\chi N_{BHCA/PEO-PPO} > \chi N_{PEO-PPO})$.

Isothermal frequency sweeps conducted on 90/10 F108/BHCA blends are shown in. For temperatures below 100 °C the material is microphase separated, exhibiting solid-like behavior with $G'$ and $G''$ weekly depending upon frequency.[91-96] Upon heating to 100 °C, $G'$ decreases slightly due to lattice softening. Between 100 °C and 105 °C, $G'$ and $G''$ decrease by several orders of magnitude, as expected for ODT. At 105 °C and above, $G'$ and $G''$ strongly depend on frequency with $G' < G''$ depicting liquid-like behavior.[21-26] The rheometer torque at low frequency in the disordered region is too low to yield a good signal/noise ratio, leading to scattered data. The melting of the structure is most clearly seen when plotting the complex modulus ($G^*$) against temperature at different frequencies, as shown in Figure 2.9(b). The sharp decrease of $G^*$ for the low frequencies between 100 °C and 105 °C represents ODT. The Winter-plot,[97] Figure 2.9(c) shows the transition even more dramatically. The solid like ordered morphology results in a nearly vertical $\eta^*$ when plotted over $G^*$, while the disappearance of order results in a nearly horizontal $\eta^*$ on the Winter-plot. The morphology transition was confirmed using SAXS before and after ODT (100-105 °C). For temperatures up to 100 °C, a sharp primary peak and higher order peaks indicate cylindrical morphology, with lattice parameter, $d=2\pi/q^* \approx 14$ nm as shown in Figure 2.10. A broad hump at 110 °C confirms disordered morphology as seen in rheology.
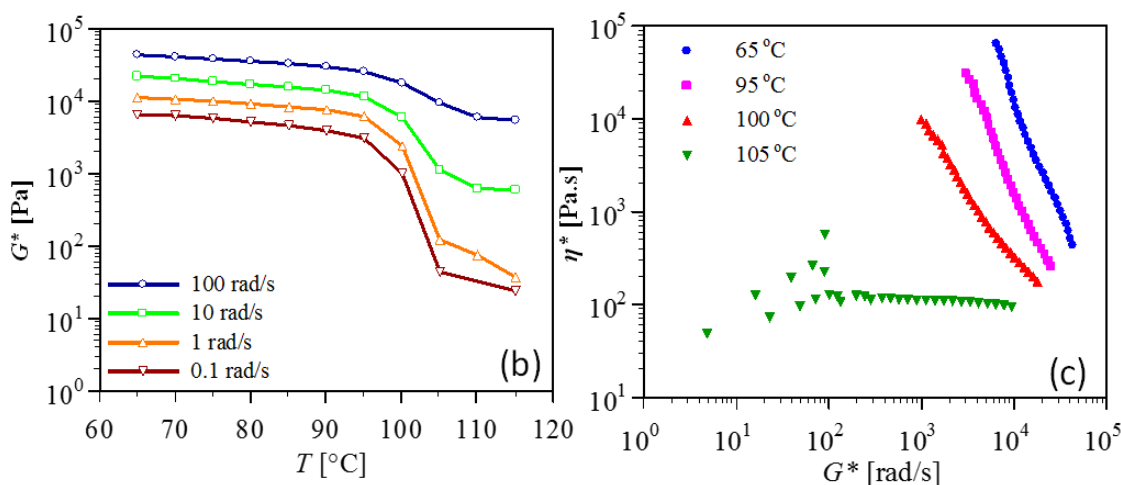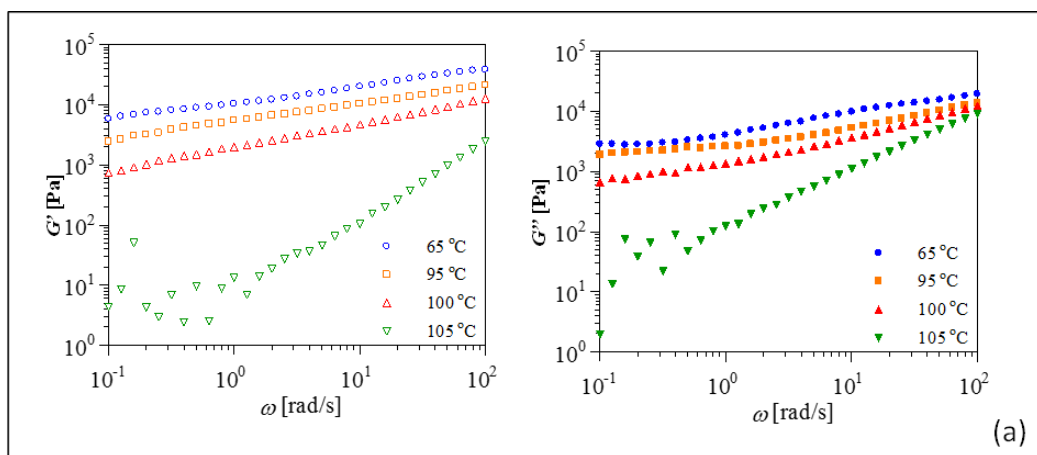
Figure 2.9 Various rheology plots for determining order-to-disorder transition temperature ($T_{ODT}$) for blends containing 90 wt% F108 and 10 wt % BHCA **(a)** Isothermal frequency sweeps of storage modulus ($G'$), on left, and loss modulus ($G''$), on right at various temperatures. $T_{ODT}$ occurs between 100 and 105 °C. Low frequency moduli at 105 °C are too small to allow good signal/noise ratios as indicated by scattered data points. **(b)** Complex modulus ($G^*$) vs temperature at different angular frequencies for the same blend. The sharp drop in $G^*$ between 100-105 °C, most pronounced at lower frequencies, represents ODT. **(c)** Complex viscosity ($\eta^*$) vs $G^*$ at different temperatures. The ODT is characterized by sharp change in the dependence of $\eta^*$ on $G^*$ between 100-105 °C. $\eta^*$ is strongly dependent on $G^*$ at temperatures of 100 °C and lower, but is weakly dependent on $G^*$ at 105 °C and higher temperature. Reprinted from Ref 89. Copyright 2014 American Chemical Society

28
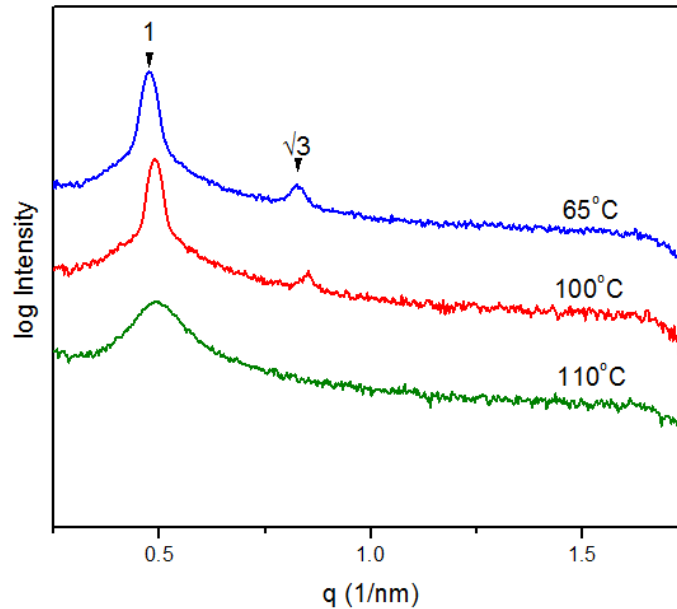
Figure 2.10 Small angle X-ray scattering (SAXS) profiles at various temperatures for blend containing 90 wt% Pluronic® F108 (F108) and 10 wt% benzene-1,2,3,4,5,6-hexacarboxylic acid (BHCA). Intensity is in arbitrary units and profiles are shifted vertically to avoid overlap. Microhpase separation results in cylindrical morphologies at 100 °C and below with $q/q^*$ √3:1. The blend disorders at 110 °C and above. Reprinted from Ref 89. Copyright 2014 American Chemical Society

It is important to note that, at low temperatures, the blend acts as physical gel (solid-like behavior) due to microphase separation and not due to formation of a network structure by multiple-hydrogen-bonding interaction between PEO chains and BHCA molecules. This is supported by dynamic mechanical measurements on a blend containing 35 wt % BHCA and 65 wt % PEO homopolymer, where hydrogen bond network formation occurs but microphase separation is not a possibility.($M_w$ = 20 kg/mol). This loading of BHCA in PEO is higher compared to the loading in PEO phase of F108 in any of the blends used in this study. Unlike gels, as discussed earlier, 35/65 BHCA/PEO blend shows strong frequency-dependent viscoelastic behavior with $G'<G''$ in the low frequency regime at 65 °C (Figure 2.6), a temperature slightly above the melting of PEO.
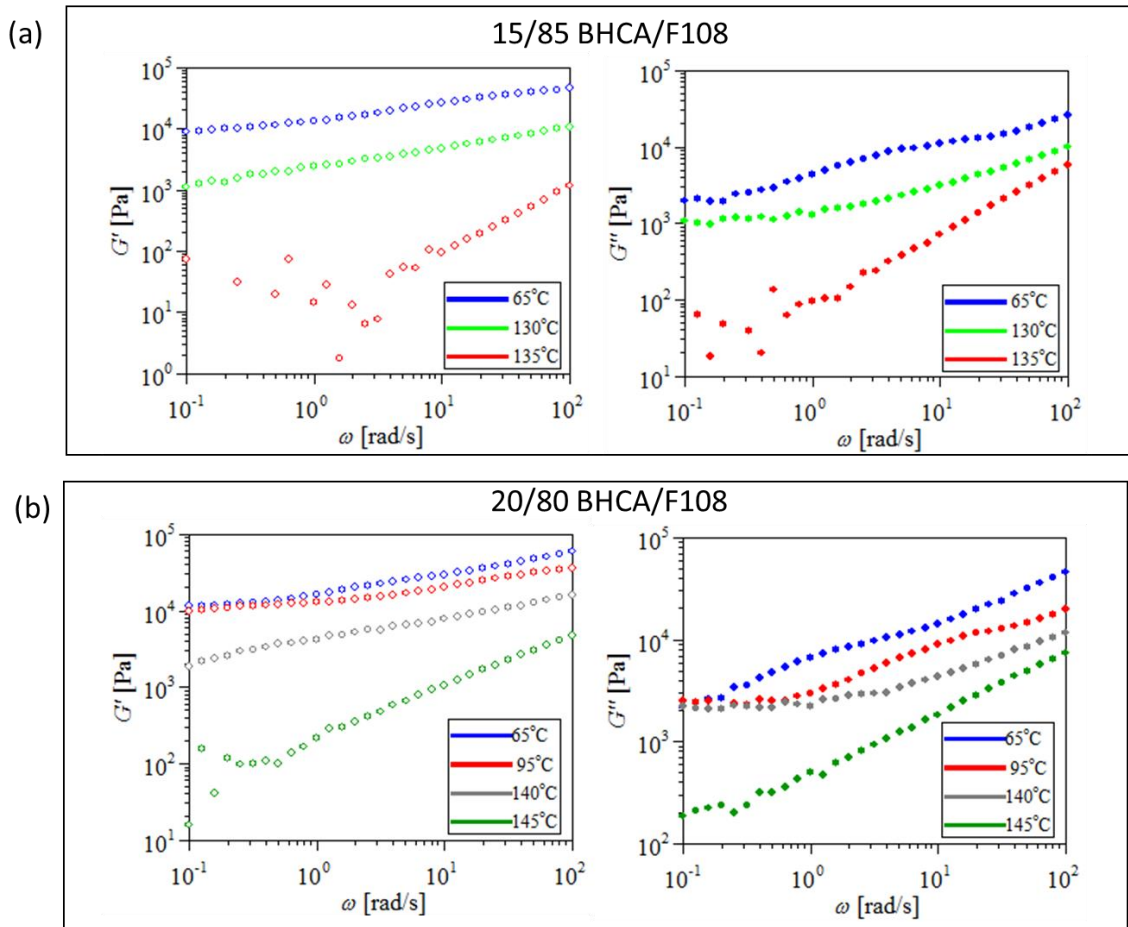
Figure 2.11 Isothermal frequency sweeps of $G'$ (on left) and $G''$ (on right) at various temperatures for (a) 15/85 BHCA/F108 and (b) 20/80 BHCA/F108. $T_{ODT}$ occurs between 130-135 °C for 15/85 BHCA/F108, and between 140-145 °C for 20/80 BHCA/F108.

Figure 2.11 and Figure 2.12 shows isothermal frequency sweep plots of $G'$ and $G''$ for up to 15, 20, 25 and 30 wt% BHCA loading in the BHCA/F108 complexes. The isothermal frequency sweep rheological experiments were performed starting from 65 °C with a step of 5 °C until ODT is detected. Isothermal frequency sweeps at 65 °C and that corresponding to ODT are shown, for pictorial clarity, plots at intermediate temperatures are omitted here. While the dependence of $T_{ODT}$ with additive loading is discussed below, from Figure 2.11 and Figure 2.12 it can be see that as the additive loading increase storage

modulus in ordered state at 65 °C (temperature well-below ODT) remains the same, ~$10^4$ Pa with increase in additive loading. This observation again reinforces the fact that the high mechanical strength of the complexes at low temperature is the result of immiscibility of the microphase separated PEO-BHCA and PPO domains and not due to the extensive hydrogen bonding network between PEO-BHCA.
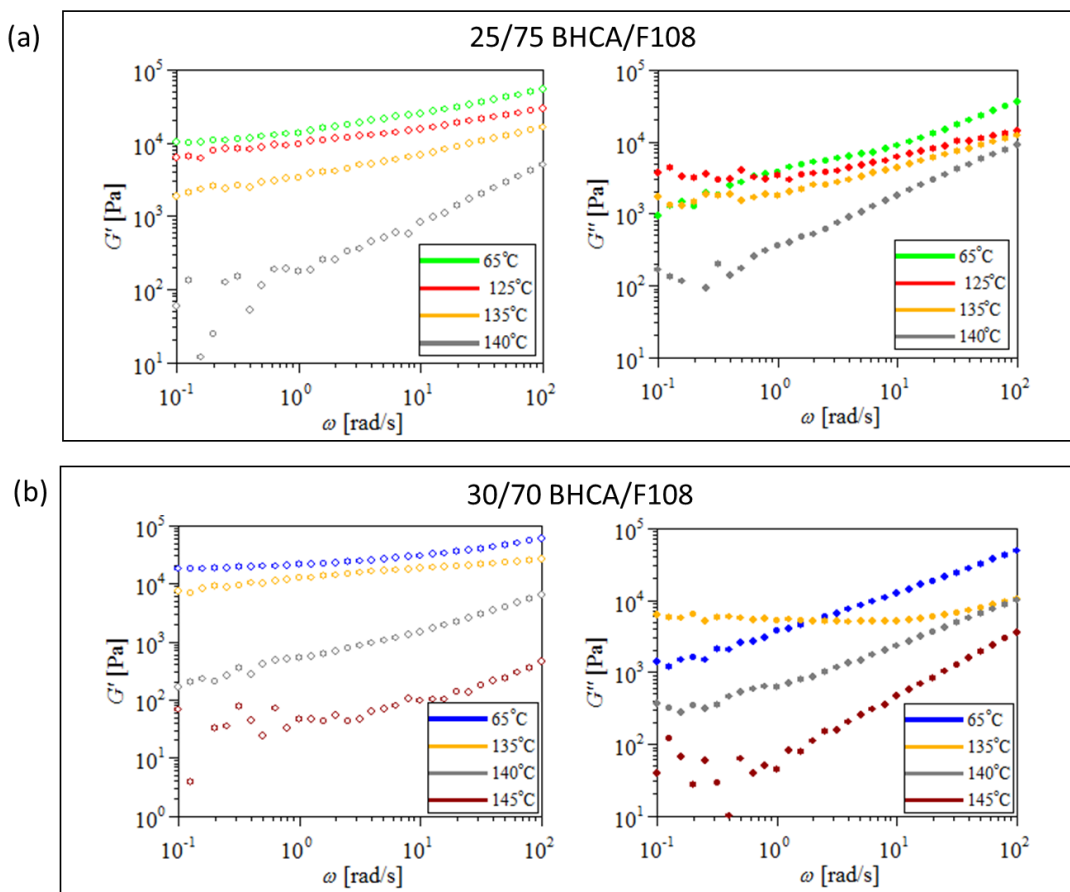


Figure 2.12 Isothermal frequency sweeps of *G'* (on left) and *G''* (on right) at various temperatures for (a) 25/75 BHCA/F108 and (b) 30/70 BHCA/F108. $T_{ODT}$ occurs between 135-140 °C for 25/75 BHCA/F108, and between 140-145 °C for 20/80 BHCA/F108.

It is important to mention that small-molecule/F108 complexes are thermally stable over the temperature range for which they are subjected to rheological experiments. Figure

2.13 shows percent weight loss (as determined by TGA in air environment) of neat F108 and 20/80 BHCA/F108 complex upon heating from 20 to 160 °C with a temperature step of 5 °C and 12 minute soaking time at each temperature, a typical heating profile during isothermal frequency sweep rheology experiments in a given temperature window. F108 showed a 1 wt% loss up to 120 C and 20/80 BHCA/F108 shows a 3 wt% loss up to 145 °C, which is in acceptable range given the tendency of PEO based materials to absorb moisture. Interestingly, BHCA/F108 complexes showed much higher thermal stability at elevated temperature (above 140 °C) compared to neat F108. F108 showed a 50 wt% loss at 160 °C where 20/80 BHCA/F108 showed only a 4 wt% loss at the same temperature. Although the exact reason for improved thermal stability of F108 upon blending with BHCA is unknown and beyond the scope of this research, it is speculated to be due to hydrogen bonding interaction between carboxyl group with ether oxygen on PEO— preventing the radical formation and chain-scission of PEO at elevated temperature. The complete recovery in modulus upon cooling the sample after heating above $T_{ODT}$ is also a sign of no degradation during the experiment to determine $T_{ODT}$. Figure 2.14 shows frequency sweeps of $G'$ for a 10/90 BHCA/F108 complex at 85 °C before and after heating at 120 °C, a temperature above $T_{ODT}$ (100-105 °C).

32
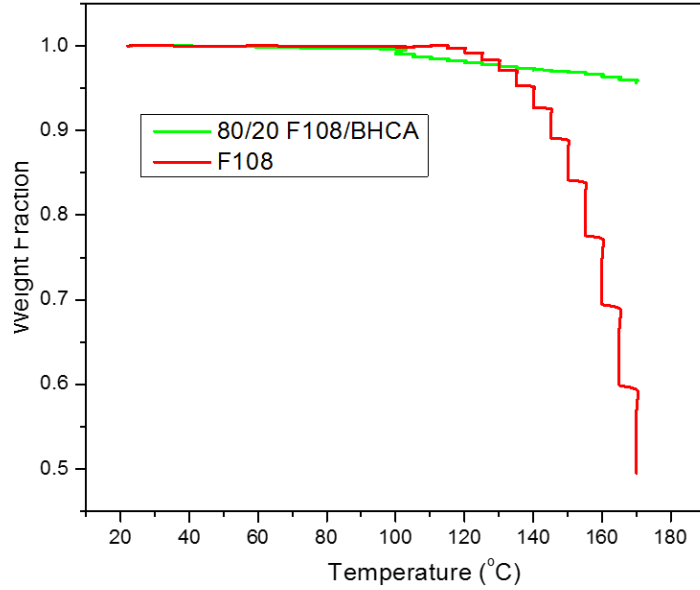
Figure 2.13 Thermogravimetric analysis (TGA) of F108 and 20/80 BHCA/F108 complex. Temperature was increased from 20 to 160 °C with a step of 5 °C and 12 minute soak time at each temperature.
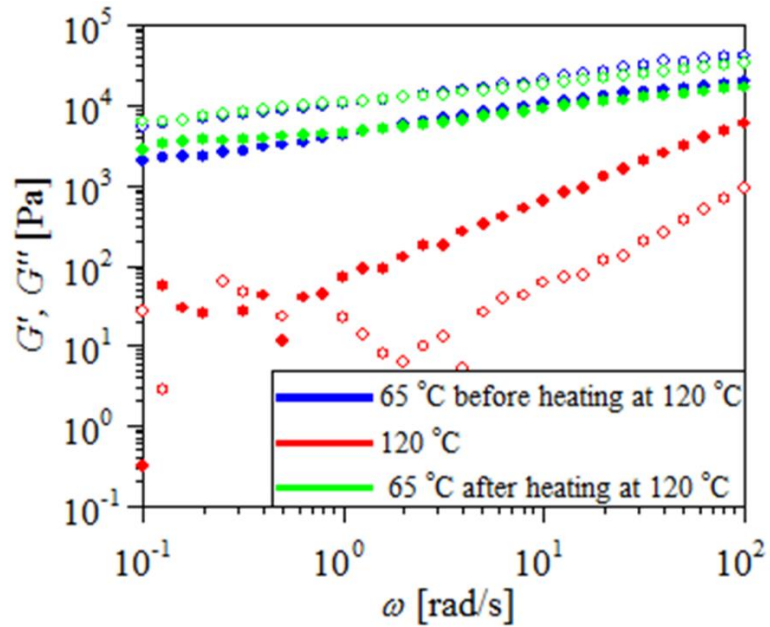


Figure 2.14 Isothermal frequency sweeps of $G'$ (open circles) and $G''$ (filled circles) of 10/90 BHCA/F108 complex at temperature above and below $T_{ODT}$ (100-105 °C) during heating and cooling cycle.
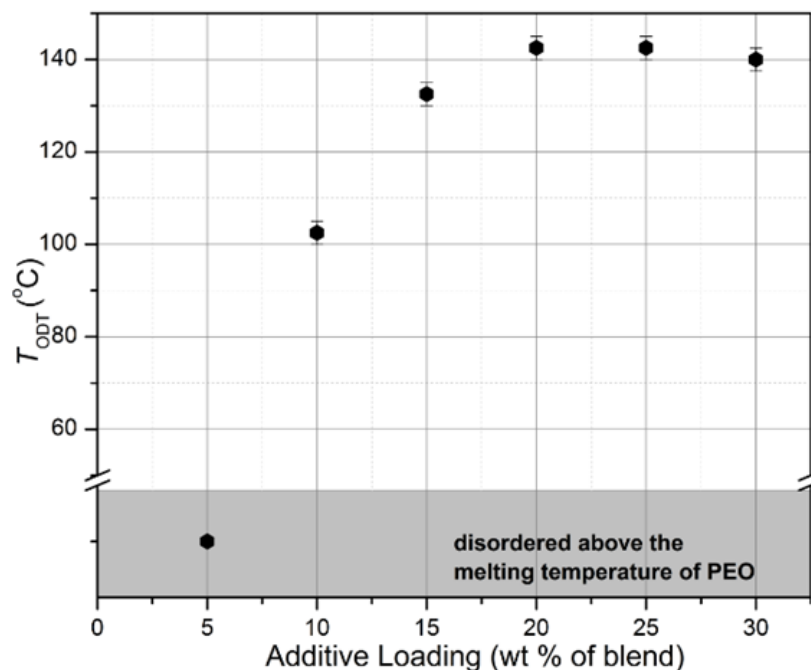
Figure 2.15 $T_{ODT}$ dependence on BHCA loading in BHCA/F108 complexes. Reprinted from Ref 89. Copyright 2014 American Chemical Society

The $T_{ODT}$ for all the complexes in Figure 2.11 and Figure 2.12, as determined by sudden drop in low frequency $G'$, are plotted against with additive loading in Figure 2.15. $T_{ODT}$ was found to rapidly increase up to 145 °C for up to 20 wt % loading, Figure 2.15. A blend with 5 wt % additive is disordered above 60 °C. Below this temperature, $T_{ODT}$ could not be determined due to the crystallization of the PEO blocks. With increased BHCA loading, number of hydrogen bonding interactions between BHCA molecules and PEO chains increases which in turn leads to an increased $\chi N_{BHCA/PEO-PPO}$ and higher $T_{ODT}$. There is no appreciable increase in $T_{ODT}$ on further increasing the additive loading. This may be a consequence of two factors, the concentration of additives is high enough such that interactions occur with all available hydrogen bond accepting sites on the polymer and a weakening of the strength of the hydrogen bonds between carboxyl group proton and ether

oxygen in PEO as temperature increases. It is likely that these weakening interactions trigger additive molecules to self-associate and form crystals at elevated temperatures.
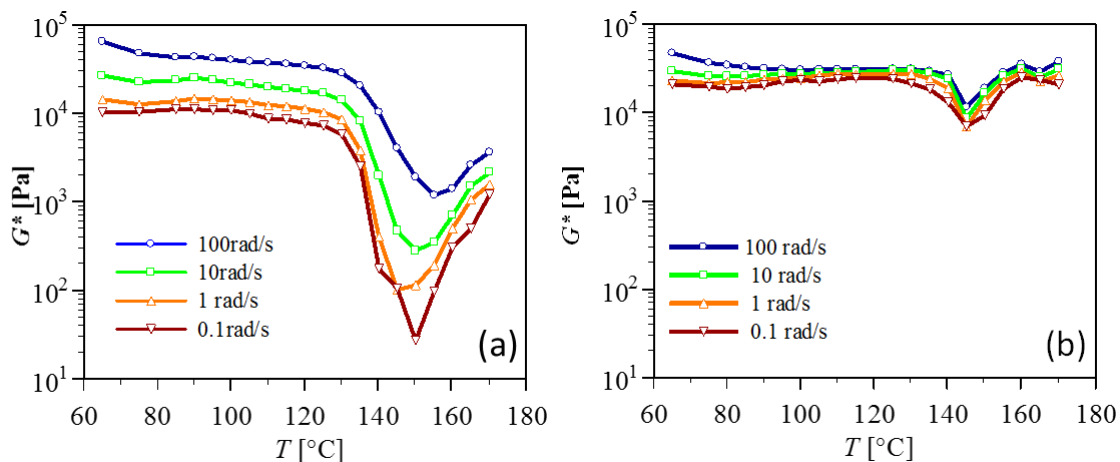


Figure 2.16 $G*$ vs temperature at different angular frequencies for a blend containing (a) 25/75 BHCA/F108 and (b) 32/68 BHCA/F108. 25/75 BHCA/F108 complex goes through an ODT at around 145 °C with the low frequency $G*$ dropping several orders of magnitude. $G*$ starts increasing again beyond ODT due to BHCA crystallization causing physical gelation. 32/68 BHCA/F108 complex slight drop in $G*$ at around 145 °C resembling an onset of ODT. A complete signature of ODT is not seen when further heating as $G*$ increases quickly due to BHCA crystallization. Reprinted from Ref 89. Copyright 2014 American Chemical Society.
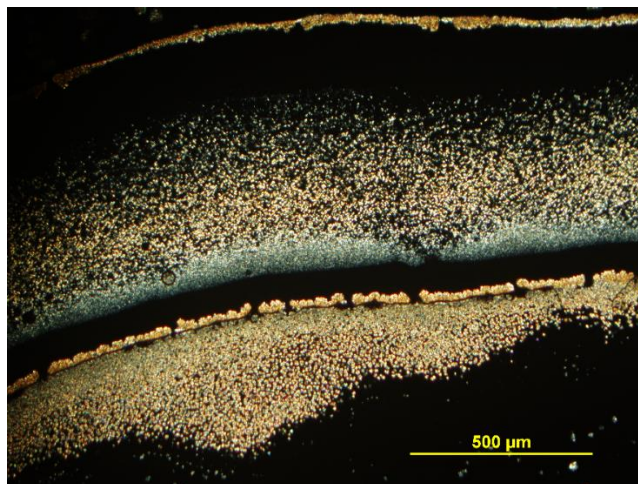


Figure 2.17 Cross polarizers optical microscope image showing crystallization of BHCA in a 25/75 BHCA/F108 heated at 160 °C. Reprinted from Ref 89. Copyright 2014 American Chemical Society.

35

There are certain conditions under which the additive crystallizes instead of forming complexes with PEO. For highly loaded systems the additive self-associates and forms crystals at sufficiently high temperature. For a blend containing 25 wt% BHCA beyond its $T_{ODT}$ (140-145 °C), the modulus increased as shown in Figure 2.16. A small change in $G*$ over a wide range of frequency at 170 °C shows that material is again acting as a gel after having passed through a solid to liquid transition at $T_{ODT}$. This increase in modulus and physical gelation is due to the formation of sufficiently large crystallites of additive creating reinforcement. The crystals act as physical crosslinking sites that hinder polymer chain segmental motion and lock the disordered morphology. Crystallization induced turbidity in the blends and was confirmed using cross polarized optical microscopy (Figure 2.17). Note that the temperatures at which macrophase separation occurs remain well below the melting point (higher than 280 °C) of the additive crystals. Moreover, the additive crystals tend to remain undissolved upon cooling back to room temperature.

Complexes with over 30 wt% BHCA are no longer homogeneous before $T_{ODT}$ is reached. For example, 68/32 F108/BHCA blends did not show any signature of an ODT. In Figure 2.16(b) there is negligible change in $G*$ upon increasing temperature from 70 °C to 140 °C. Heating from 140 °C to 145 °C causes $G*$ to decrease slightly but $G*$ increases again upon further heating beyond 150 °C and almost regains its initial values upon heating to 170 °C.

Complexes with 35 wt% and 40 wt% BHCA interestingly showed a disorder-to-order transition at low temperature. Figute 18a shows isothermal frequency sweep of 40/60 BHCA/F108 with liquid like frequency dependent viscoelastic behavior at 85 °C (blue curve; 85 °C initial), upon heating the as prepared sample from 65 to 85 °C during

rheological experiment. Upon further heating the sample to 120 °C, modulus shoots up and become frequency independent, like in case of ordered morphology. The high modulus retained upon cooling the sample back to 85 °C. Indeed, SAXS of 40/60 BHCA/F108 (Figure 2.18(b)) confirmed initial disordered morphology at 85 °C (blue curve; 85 °C initial) , and ordered spherical morphology at 120 °C which retains upon cooling back to 85 °C (red curve; 85 °C final). This disorder-to-order transition upon heating highly loaded blend is because the equilibrium ordered-morphology is unattainable at low annealing temperature (65 °C). The highly loaded BHCA/F108 complex has very high viscosity due to extensive hydrogen bonded network, which precluded the complex to achieve an ordered state due to sluggish dynamics. Upon increasing temperature, hydrogen-bonds weaken and viscosity decreases, allowing complex to attain equilibrium microphase separated morphology, which is spherical morphogoly at such high volume fraction of BHCA in PEO phase. Upon further increasing BHCA loading to 40 wt %, the blends assume spherical morphologies. ODTs in this complex cannot be detected due to crystallization of the additives at higher temperature.

Complexes with BHCA loadings of 50 wt% and more cannot be achieved as BHCA crystallizes and macrophase separate during solvent removal. Similar macrophase separation of crystals at high temperature has been observed for pentadecylphenol, which forms hydrogen bonds with methane sulphonic acid functionalized poly(4-vinyl pyridine).[78]
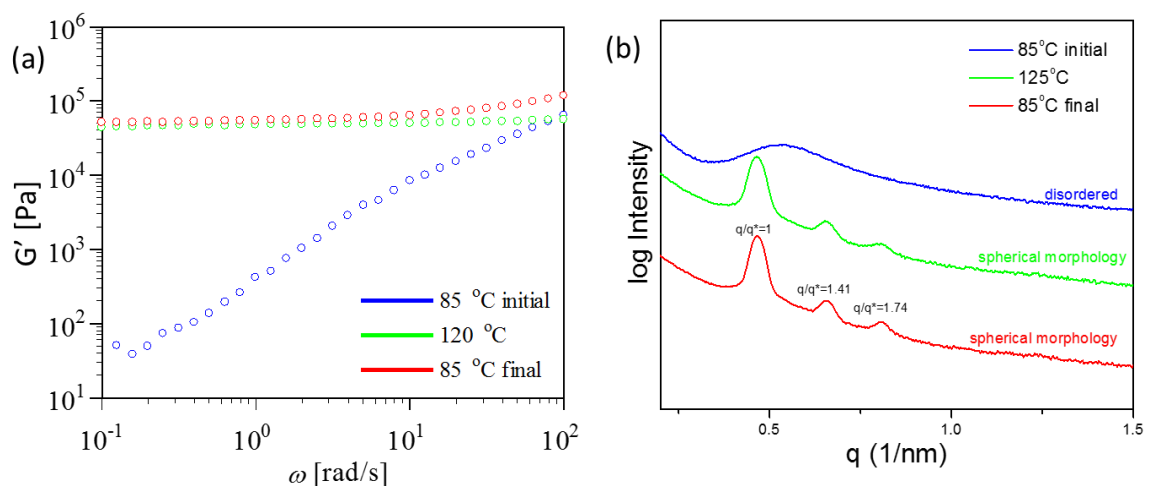
Figure 2.18 (a) Isothermal frequency sweep and (b) SAXS for 40/60 BHCA at different temperature during heating and cooling. Blue and red curve represents data collected at 85 °C during heating form 65 °C to 120 °C and duirng cooling form 120 °C to 65 °C respectivly.

### 2.3.3    Comparison of ODT in different small-molecule/F108 complexes.

The rigid small molecule-Pluronic® BCP complexes serve as model systems to study the effect of number and strength of hydrogen bonding interactions on $T_{ODT}$ as determined by rheology, as described earlier. The additives shown in Figure 2.3 were selected for their different number of hydrogen bonding functional groups (carboxyl) while maintaining the same non-interacting core (benzene ring). As $T_{ODT}$ is directly related to the segregation strength, rheology enables us to compare the effectiveness of additives for inducing microphase separation in these blends. For comparison purpose, additives are blended into F108 in amounts that maintain constant milliequivalents of functional groups so as to have nearly the same enthalpic interaction per gram of F108. Figure 2.19 and Figure 2.20 presents isothermal frequency sweeps of $G'$ and $G''$ for various F108 complexes containing small molecule additive with carboxyl functionality. The $T_{ODT}$, as determined

38

by the rheological data is then plotted against additive loading in Figure 2.21. The corresponding milliequivalents of functional group per gram of F108 and the resulting morphology type as determined by SAXS at 60 °C are indicated next to each data point in Figure 2.21. A significant reduction in $T_{ODT}$ was observed upon reducing the number of hydrogen bonding sites available on the additives, while keeping the total number of hydrogen bonding sites the same in all blends. A change of number of functional groups on the additive from 6 to 5 and from 6 to 3 respectively lowers the $T_{ODT}$ by ~20 °C and ~80 °C.

Although microphase separation in these blends is enthalpically driven, the decrease in the $T_{ODT}$ with the reduction in the number of functional groups relative to the number of cores cannot be solely attributed to the reduced number of hydrogen bonding sites. Entropic penalties resulting from the chain stretching of PEO to accommodate the additive molecules also favor the observed decrease in $T_{ODT}$. To keep the total number of hydrogen bonding sites constant, 123BTCA is added in highest volume followed by BPCA, followed by BHCA. The simulated Connolly solvent excluded volumes of these molecules can be related to volume that they will occupy in the PEO phase. These are 164 $Å^3$, 152 $Å^3$ and 135 $Å^3$ for BHCA, BPCA and BTCA respectively.[98]  For say 30 functional groups loaded into F108, number of molecules of added would be 5 for BHCA, 6 for BPCA 6, and 10 for 123BTCA. This provides that for a given number of enthalpic interactions the volume of BPCA and 123BTCA would be 1.1 times and 1.6 times that of the volume of BHCA, respectively. Although differences in BHCA and BPCA are small, 123BTCA differs significantly and therefore F108/123BTCA blends assume spherical morphologies

at low loading percentages, at which F108/BHCA and F108/BPCA blends are in the cylindrical morphology region.
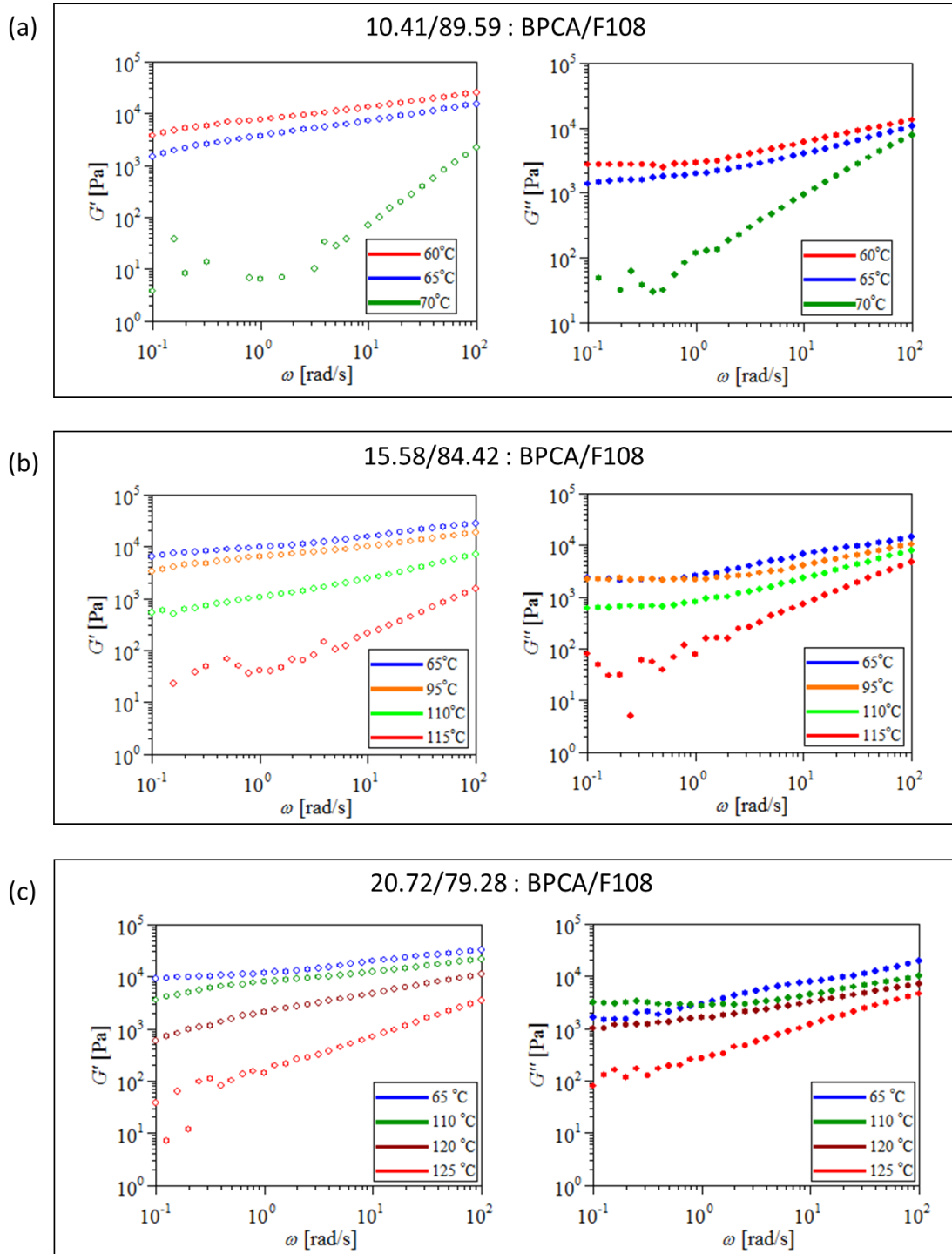


Figure 2.19  Isothermal frequency sweeps of $G'$ (on left) and $G''$ (on right) at various temperatures for different compositions of BPCA/F108 complexes.
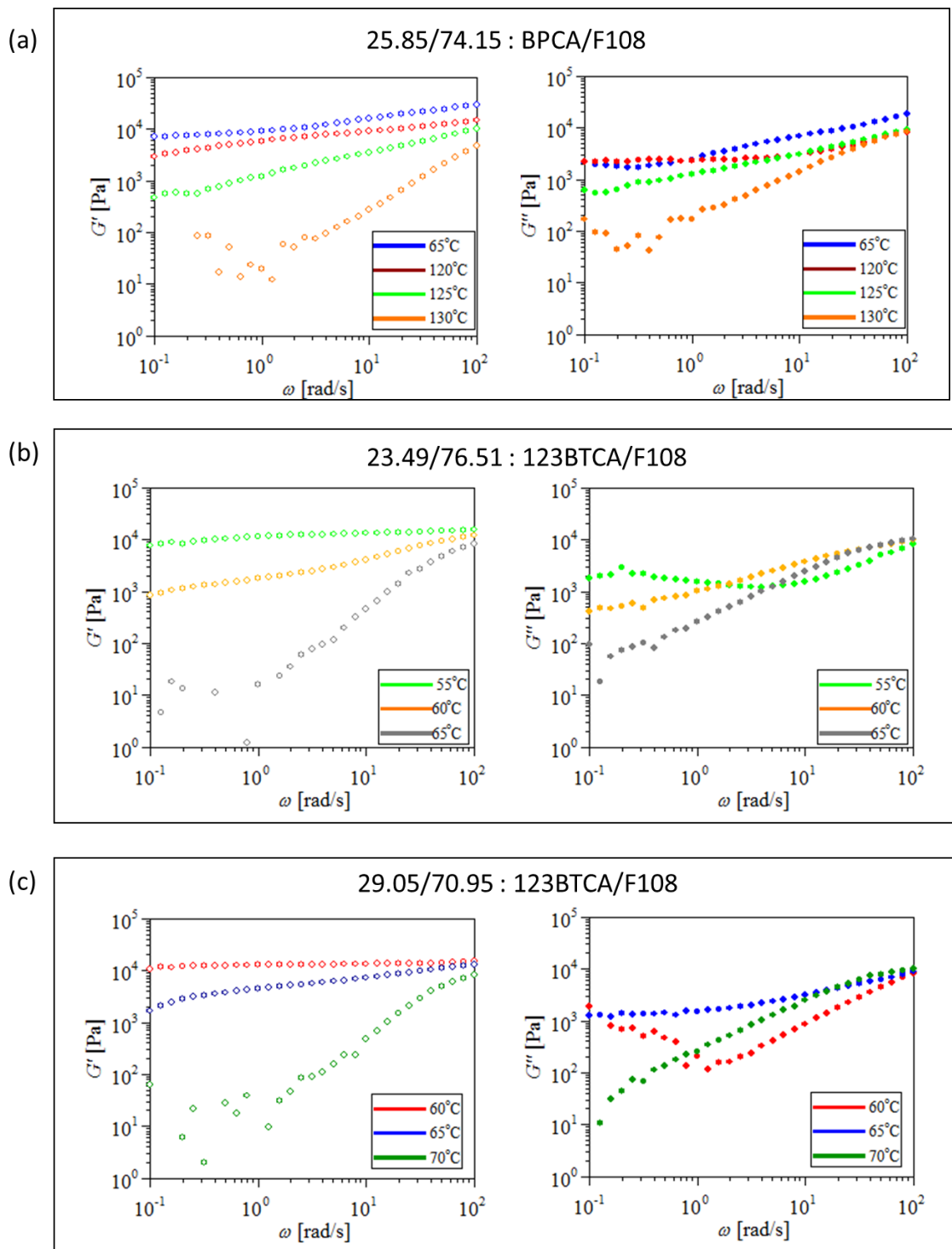
Figure 2.20 Isothermal frequency sweeps of *G'* (on left) and *G''* (on right) at various temperatures for different compositions of BPCA/F108 and 123BTCA/F108 complexes.
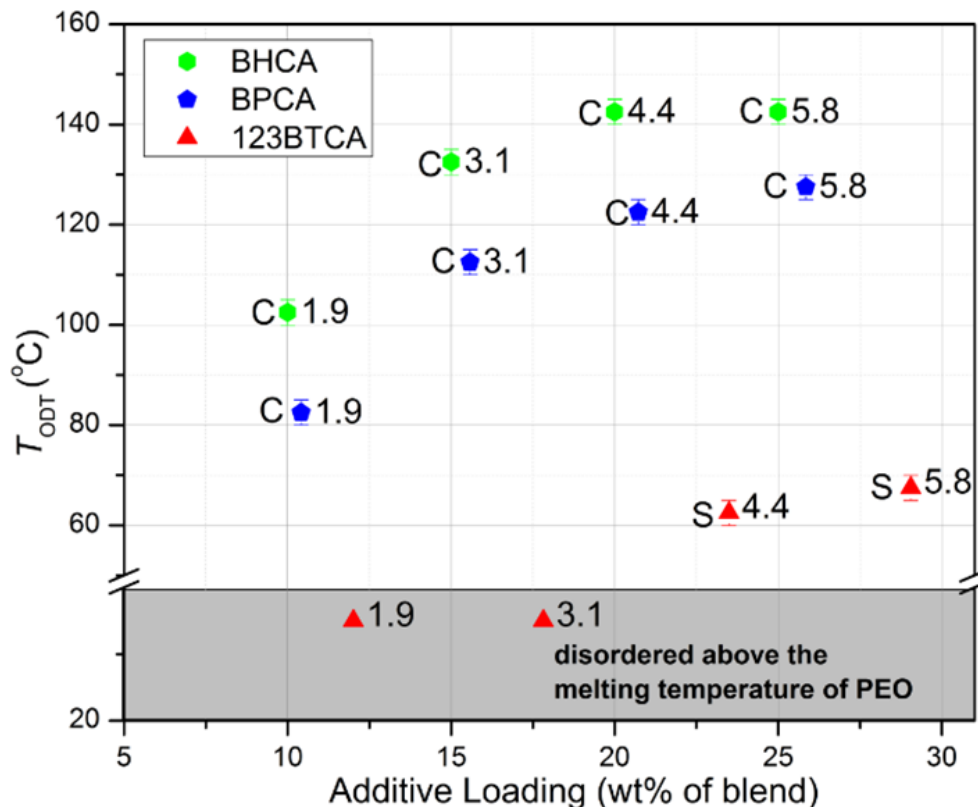
Figure 2.21 $T_{ODT}$ dependence on additive loading for blends containing F108 and three different additives bearing carboxyl functionality, BHCA, BPCA and 123BTCA. Character next to each data point represents morphology of the blend at 60 °C, 'C'-cylindrical morphology and 'S'-spherical morphology. The digit next to each data point represents milliequivalents of carboxyl functional group incorporated per gram of F108 in the complex. Reprinted from Ref 89. Copyright 2014 American Chemical Society.

It has been reported that the acidic strength of a functional group is directly proportional to hydrogen bonding strength[99]. Therefore, in these blends, it is one of the key factors affecting segregation strength. pKa values indicate 123BTCA (pKa 2.88) is a weaker acid than BHCA (pKa 1.80).[100,101] and therefore forms a weaker hydrogen bond. 123BTCA crystallization has been observed in blends at temperature as low as 80 °C. Though BHCA, BPCA and 123BTCA forms homogeneous blends for concentration explored up to 30 wt%, phthalic acid and benzoic acid precipitates out even at 5 wt%

loadings. More interestingly benzene 135BTCA also precipitates out at 5 wt % loadings in spite of having same number of functional groups as 123BTCA. There is competition between the interaction of additive molecules with PEO and with themselves. Additives with weak and insufficient numbers of hydrogen bonding sites upon blending with F108 do not have enough overall hydrogen bonding interaction energy to overcome its crystallization. Moreover, the additive molecules have different crystallization energies owing to difference in molecular structure and packing. Therefore 135BTCA, being planar, precipitates out whereas 123BTCA (nonplanar) does not. Benzene-1,2,3,4,-tetracarboxylic acid was not used in this study due to its sparse commercial availability and complex synthesis. Benzene-1,2,4,5,-tetracarboxylic has poor solubility in PEO, similar to 135BTCA and phthalic acid.

The effectiveness of microphase separation, as measured in terms of $T_{ODT}$, also obviously depends upon the hydrogen bond forming capacity of the functional group on additive molecule. BHCA and HHB, both contain a benzene ring and 6 carboxyl and hydroxyl functional groups respectively and are suitable molecules for comparing the effect of these functional group on $T_{ODT}$. For the purpose of comparison of $T_{ODT}$, BHCA and HHB were blended into F108 in an amount to provide the same number of hydrogen-bonding functional groups per gram of F108. Figure 2.22 presents isothermal frequency sweeps of $G'$ and $G''$ for different compositions of HHB/F108 complexes.
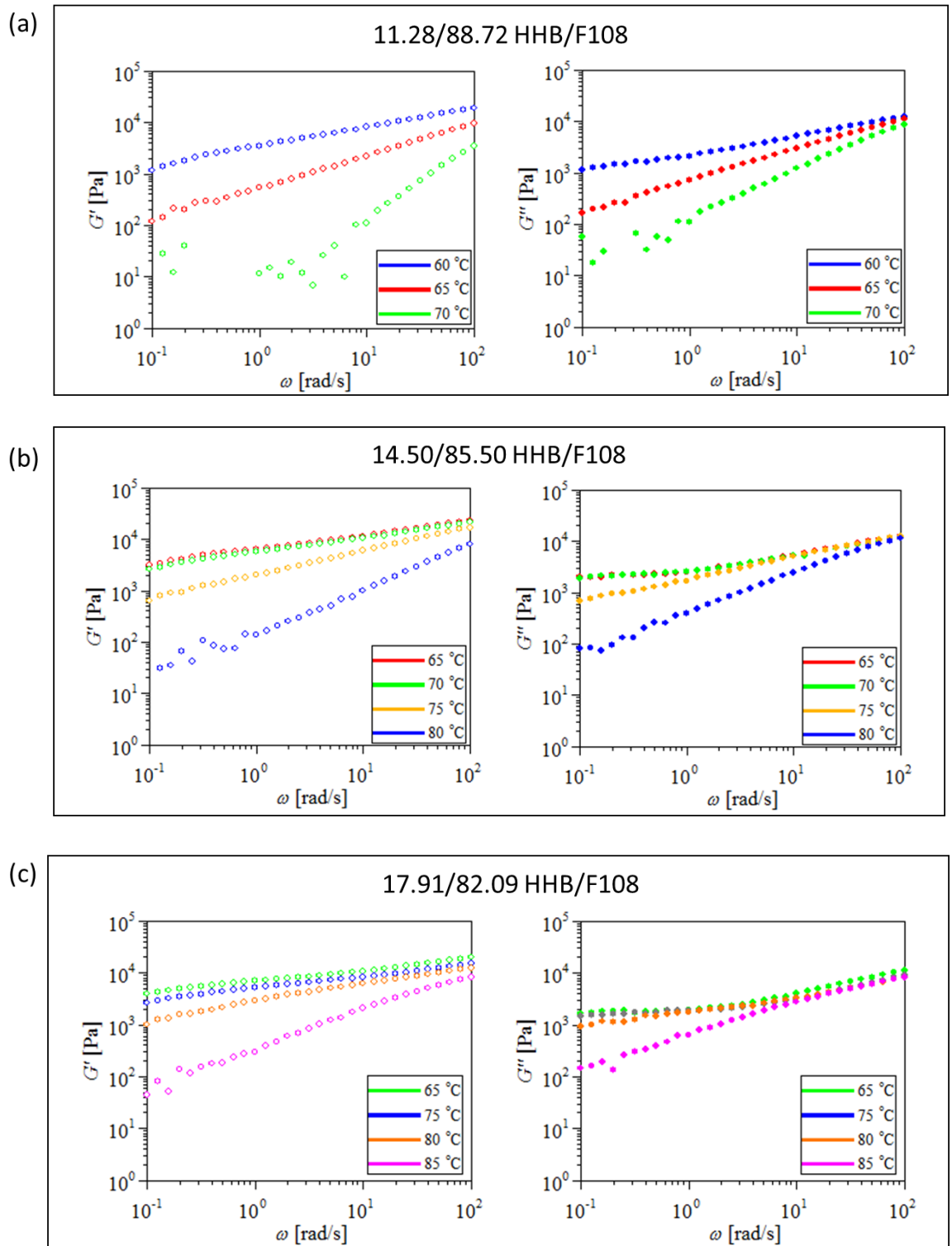
Figure 2.22 Isothermal frequency sweeps of *G'* (on left) and *G''* (on right) at various temperatures for different compositions of HHB/F108 complexes.

The $T_{ODT}$, as determined by the rheological data is then plotted against additive loading in Figure 2.23 along with $T_{ODT}$ in BHCA/F108 complexes. The corresponding milliequivalents of functional group per gram of F108 and the resulting morphology type as determined by SAXS at 60 °C are indicated next to each data point in Figure 2.23. For 1.9 and 3.1 milliequivalents of functional groups per gram of F108, blends with HHB are still in a disordered state above melting point of PEO. At 4.4 milliequivalents functional group loading per gram of F108, $T_{ODT}$ for HHB blends is lower by 80 °C than of BHCA blends, indicating much higher segregation strength in BHCA blends. Simulated Connolly solvent excluded volumes of these molecules are 88 $Å^3$ and 164 $Å^3$ for HHB and BHCA respectively.[98] Since the size of the core benzene ring is unchanged, differences between filler volumes originate from the larger size of the carboxyl group compared to the hydroxyl group. For the same number of enthalpic interactions, the volumetric penalty is significantly larger in case of BHCA blends as compared to HHB. Still, the capacity of BHCA to induce phase segregation in F108 is significantly higher than of HHB. This is due to stronger hydrogen bonding of ether-oxygen of PEO segments with more electron deficient proton of the carboxyl group, compared to hydrogen bonding with the less electron deficient proton of the hydroxyl group, as sketched in Figureppp (a) and (b). Since the BHCA/F108 complexes are no longer homogeneous for loadings above 30 wt % of BHCA for the determination of $T_{ODT}$, and comparison with HHB is no longer valid after this point.
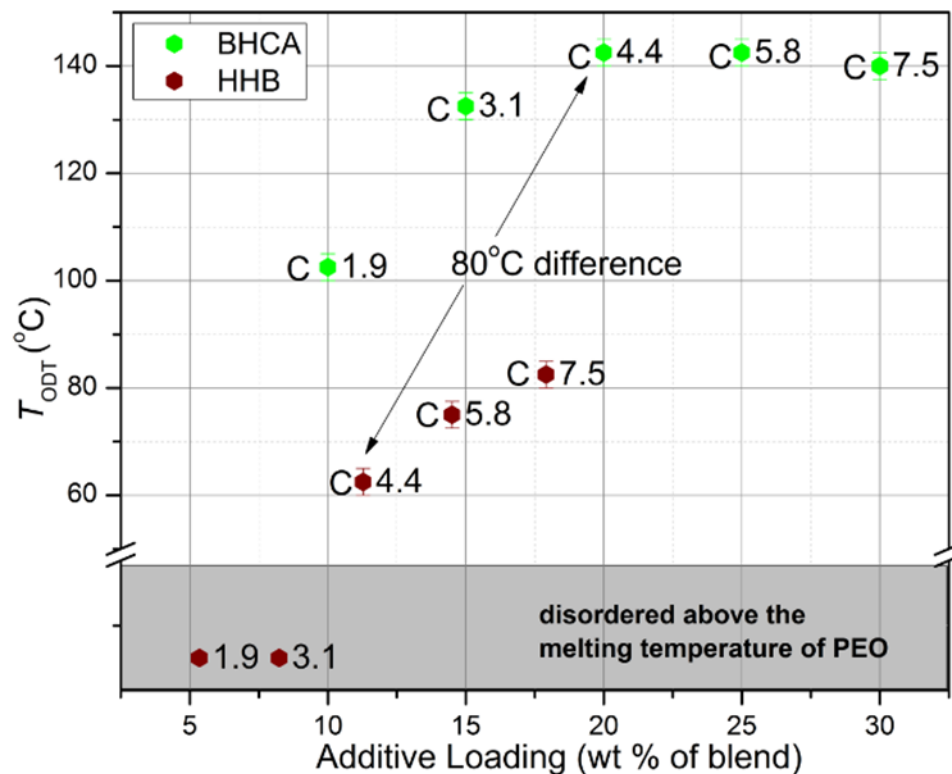
Figure 2.23 $T_{ODT}$ dependence on additive loading for blends containing F108 and two different additives, BHCA and HHB. Character 'C' next to data point represents cylindrical morphology of the blend at 60 °C. The digit next to each data point represents milliequivalents of functional group (carboxyl in case of BHCA and hydroxyl in case of HHB) incorporate per gram of F108 in the complex. Reprinted from Ref 89. Copyright 2014 American Chemical Society.

### 2.3.4 Microphase separation in hexaketocyclohexane/F108 blends

It is well established that the microphase separation in Pluronic® blends with carboxyl and hydroxyl containing additives is driven by the hydrogen bonding interaction between the electron deficient hydrogen atom in these functional group with the electron rich ether oxygen in PEO[86-88], as shown in Figure ppp in case of BHCA and HHB. The interaction of H atom with ether unit in PPO is restricted because of the methyl group attached to the α-C (i.e. carbon atom attached to oxygen atom in PPO), providing steric hindrance. Since the ether oxygen in PEO unit is electronegative, it will polarize the C-O

46

bond in ethylene oxide unit and make the protons attached to the C atom (protons in –(CH$_2$-

O)- unit) electron deficient. It is hypothesized that if an electronegative species is added to

F108, it may induce microphase separation by the interaction of the species with electron

deficient protons in –(CH$_2$-O)- unit of PEO. To check this hypothesis, we blended

hexaketocyclohexane (HKC; C$_6$O$_6$) with F108. HKC does not contain any proton to

interact with ether oxygen in PEO, therefore the only possible way it could interact with

PEO is via hydrogen-bonding between electronegative carbonyl group (C=O)  in HKC and

proton in –(CH$_2$-O)- unit of PEO.
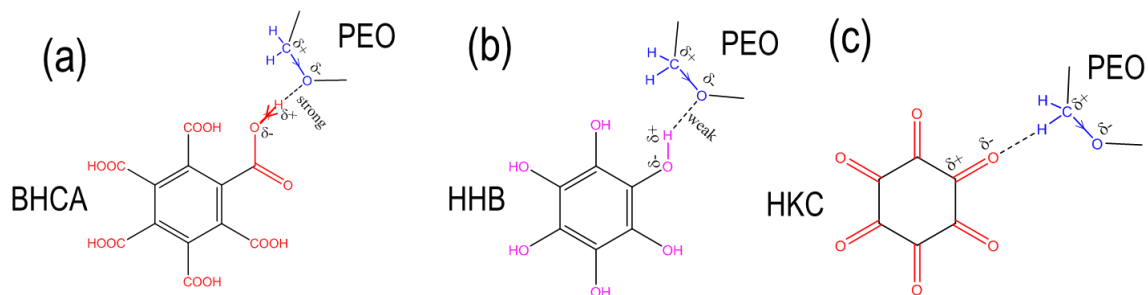


Figure 2.24 Hydrogen bonding interaction between PEO and additives containing (a) carboxyl group ((b) hydroxyl group and (c) carbonyl group.

A 20/80 HKC/F108 blend indeed showed an ordered cylindrical morphology in

SAXS experiment (Figure 2.25), supporting the fact that hydrogen bonding interaction

between HKC/PEO lead to increased χ parameter (χ$_{HKC/PEO-PPO}$ > χ$_{PEO-PPO}$) parameter and

caused microphase separation. It is well known that carbonyl unit of the carboxyl acid

group interacts with acid-proton to form hydrogen-bonded acid dimer. Therefore, a similar

hydrogen bonding interaction between carbonyl in carboxyl group with proton in –(CH$_2$-

O)- is also a possibility upon blending carboxyl containing additive with PEO containing

F108, leading to strongly segregated complexes in contrast to the additives with hydroxyl groups.
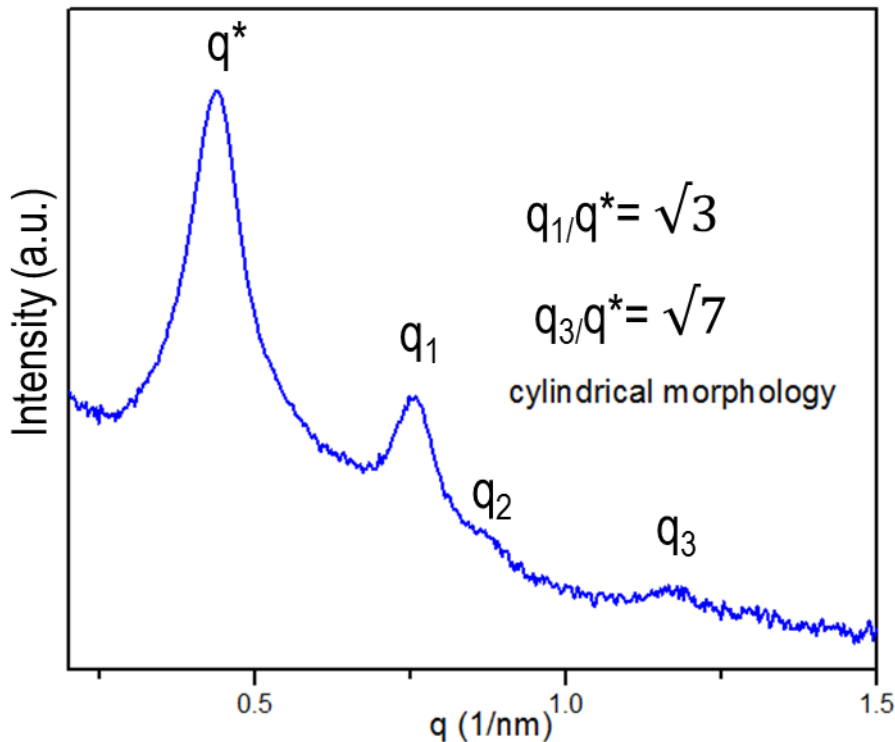


Figure 2.25 SAXS at 65 °C of 20/80 hexaketocyclohexane/F108 complex with peaks corresponding to a cylindrical morphology.

## 2.4 Conclusion

Small-molecule-additives bearing multiple hydrogen bonding sites can induce microphase separation in otherwise disordered F108. The additive molecules consist of carboxyl or hydroxyl functional groups attached to a benzene ring. The hydrogen bonding between these functional groups on additive and the PEO chains of F108 increase effective $\chi$ parameter between PEO and PPO chains thereby leading to microphase separation. The rich phase behavior of these F108/small-molecule-additive complexes depends upon

loading of additive, temperature, and number of functional groups on the additive molecule.

Additives with 6 carboxyl groups surrounding an aromatic core (BHCA) show strongest tendency to strengthen microphase separation. $T_{ODT}$ increases steadily with BHCA loading in the blend and levels of at about 20 wt% loading. Unlike common behavior of increasing solubility of small molecules crystallites with temperature, here we find for high loadings the additives tends to self-interact and crystallize out upon increasing temperature due to a weakening of hydrogen bonds between additive molecules and PEO chains. These crystallites formed at high temperature cause an increase in modulus due to reinforcement effects. A disorder-to-order transition was observed during heating complexes with high loading (35-40 wt%) of BHCA. $T_{ODT}$ notably drops in upon decreasing the number of hydrogen bonding functionalities on the additive core while keeping the total number of hydrogen bond donating functional groups approximately constant. Upon reducing the number of carboxylic groups from 6 to 5 and from 6 to 3 there is ~20 °C and ~80 °C decrease respectively in $T_{ODT}$. Using these small molecules as models, we find that $T_{ODT}$ of these microphase separated blends created by hydroxyl functionalized additive is significantly lower by 60-80 °C compared to carboxyl functionalized additive. Additive bearing carbonyl group was also found to be capable of inducing microphase separation in F108 via hydrogen bonding interaction between proton in ethyleneoxide unit of PEO and oxygen of the carbonyl group.

## 2.5   Acknowledgements

CHAPTER 3

MESOPOROUS SILICA/NANOPARTICLE COMPOSITES

FABRICATED BY 3D REPLCATION OF HIGHLY FILLED BLOCK

COPOLYMER TEMPLATES IN SUPERCRITICAL CARBON

DIOXIDE MEDIUM

## 3.1  Introduction and Objectives

**Mesoporous Silica as Catalyst Support for Metal Nanoparticles.** Catalysis is an important and expanding field of chemistry that facilitates development of useful chemicals from raw materials, which otherwise seemed elusive. Catalysis enabled reactions to be fast, energetically efficient and selective.  Heterogeneous catalysis is especially attractive as catalyst is in different phase than reactants making it possible to be recovered and recycled after completion of the reaction. Metal surfaces display excellent heterogeneous catalyst for a plethora of chemical reactions involving liquid and gaseous reactant materials. The use of metal nanoparticles in catalysis is of especial importance as they increase the reaction efficiency by providing several orders of magnitude larger surface area compared to their bulk counterparts for the same amount of material. Metal nanoparticles can be anywhere between one to several 100 nanometers, but crystals with few nanometer in size, along with providing large surface area, are found to be most active for catalysis.[102, 103] Famous Heck reaction involves usage of catalytically active Pd nanoparticles for C-C coupling reactions between alkenes and aryl halide for arylation of alkenes.[104,105] Au nanoparticles shows catalytic property for conversion of carbon monoxide to carbon

dioxide with potential utility in car engines to reduce release of obnoxious carbon monoxide. Au nanoparticles are also shown catalyzing reactions involving hydrogenation of olefin.[106] Catalytic activity of Rh nanoparticles are used in conversion of syngas (carbon monoxide and hydrogen) to ethanol.[107] Catalytic splitting of hydrogen into proton and electron on the surface of Pt nanoparticles is well known and commercially used in anodes of proton exchange membrane fuel cells. The field is actively research from several decades and aforementioned are a few out of enormous reported examples of catalytic activity of metal nanoparticles.

Metal nanoparticles, due to high surface to volume ratio, tend to form aggregates in order to reduce surface energy. Aggregation reduces catalytically active surface area and therefore lowers reaction throughput. As mentioned previously, some reactions are only specific to nanoparticles with few nanometer in size, agglomeration will also lead to loss of catalytic properties. Therefore, in order to prevent agglomeration and take full advantage of catalytic activity of metal nanoparticles, they are often required to be immobilized on substrates. Metal oxides, for example on silica,[108,109] alumina,[110,111] titania,[112, 113] and zirconia[114, 115] have been widely used to support metal nanoparticles for catalysis. Inorganic oxides supported nanoparticles have advantages such as stability at high temperature and easy separation of large sized heterogeneous supports from reaction medium. In some cases, supporting nanoparticles on oxides is also crucial for their catalytic activity. For example, Au nanoparticles when supported on titania can catalyze oxidation of carbon monoxide to carbon dioxide at temperature as low as 200 K.[102,116] Mechanism of the reaction is not well understood but it is believed to be related with low energy barrier for the adsorption of nascent oxygen on the oxide surface adjacent to the nanoparticle surface

on which carbon monoxide is adsorbed. Similarly, Pt and bimetallic Pd-Au nanoparticles when supported on silica showed high activity for carbon monoxide to carbon dioxide and were also useful in hydrogenation of toluene.[117, 118]

MCM-41 and SBA-15 type mesoporous silicate are ideal candidates for supporting metal nanoparticles due to their high surface area, allowing active area of nanoparticles well exposed for catalysis. Apart from high surface area, the aforementioned reasons, i.e. oxide stability at high temperature and easy recovery/recyclability of catalyst are key to the use of mesoporous silicates as catalytic supports. For these purposes, extensive research has been carried out in the recent past for incorporating metal nanoparticles into mesoporous silicates.

There are 4 primary method exploited by researchers to incorporate metal nanoparticles into mesoporous silica. Discussed below are the methods and their drawbacks.

1) Inception wetness method. A metal salt (precursor) solution is added to mesoporous silica in an amount to just completely 'wet' the pores. After drying of solvent, nanoparticles are generated from the salts by reduction methods, for example sonochemical[119] (Figure 3.1a), reduction using $H_2$ gas[120] (Figure 3.1b) or silanol groups present on the surface of amorphous silica[121] (Figure 3.1c) or organo-functionalized MCM-41.[122] There are several drawback of this method to fabricate mesoporous silica containing metal nanoparticles, as discussed in the following paragraphs.
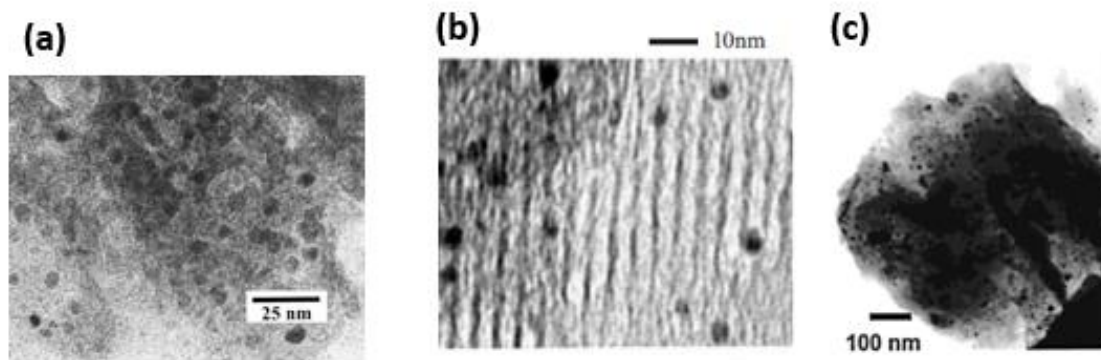
Figure 3.1 (a) Au/SiO$_2$ composite prepared by sonochemical reduction of HAuCl$_4$ filled inside the pores, adapted from Ref. 119 (b)Mesoporous silica/Pt nanoparticle composite prepared by loading Pt(acac)$_2$ precursor dissolved in supercritical CO$_2$ with acetone into mesoporous silica followed by reduction in flowing H$_2$ , adapted from Ref. 120 (c) (A) amorphous silica/Au nanoparticle composite after spontaneous reduction of the AuCl$_4^-$ ions by surface silanol groups of amorphous fumed silica, adapted from Ref. 121.

Diffusion of salt solutions through mesopores may be sluggish. It took 3 weeks for aqueous gold precursor slat (HAuCl$_4$) solution to completely fill mesopores in silica.[119] Diffusion resistance due to entrapped air in variable curvature may be the reason for slow infiltration. There is also a poor control on the size and dispersion of nanoparticles growing inside mesoscale pores. The absence capping agents like alkylamines and alkylthiols[122] and inferior dispersion of the salt throughout the pore after removal of solvent often lead to the undesirable growth of nanoparticles during the reduction step. This causes nanoparticle to encroach everywhere on the pore wall thereby blocking the pore, resulting in reduced mass transport during catalysis. Reduction of HAuCl$_4$ by sonochemical[119] method created nanoparticles of size 5.2 nm inside pores less than 6 nm size, Figure 3.1a. Nanoparticles were also found to be aggregating inside mesopores. In another study by Wakayama et al., Pt precursors were infused inside the mesoporous silica with different pore sizes and reduced using H$_2$ gas.[120] Nanoparticles were found to grow to a sizes 1.5, 1.7, 2.3 and 2.9

nm inside 1.6, 2.1, 2.4 and 3.5 nm diameter pores, respectively. The size of nanoparticles is again only a slightly less than the pore size of silica being used. If a liquid solvent was used to infiltrate Pt precursor, the inefficient transport inside the small pores lead to the formation of 10-30 nm sized large nanoparticles on the external area of 2-3 nm mesoporous silica. In a preemptive measure to restrict agglomeration and coalescence of the nanoparticles, precursor is usually added in low concentrations, just enough to wet the pores. Small loadings and low metal content of the precursor salt ($HAuCl_4$ contain only about 60 wt% Au) leads to small loading of metal nanoparticles in mesoporous silica, and hence low catalytic activity of the final nanocomposite. Ghosh et al., used dilute solutions of $HAuCl_4$ to fill pores of to MCM-41 for an extended period of 3 days.[123] The mesopore walls were also functionalized using propylamine and propylthiol so as to anchor the nanoparticles after reduction and therefore stabilizing them from growing. Resulting loading of Au nanoparticle in MCM-41 was limited to maximum 3.5 wt%. In another study, Pt loading was limited to less than 3 wt% of silica in the final mesoporous silica/metal nanoparticle composite prepared by Wakayama et al.[120]

2) Impregnation of pre-synthesized nanoparticles into mesoporous silica. There are relatively fewer studies of this method compared to inception wetness method. In this method nanoparticles coated with ligands are synthesized separately and then infused inside the pores of mesoporous silica with the help of a carrier solvent. The challenge lies in transporting nanoparticle dispersion into the pores by capillary wetting. To improve wetting, pore walls are often functionalized[124] to flood the dispersion inside the pores and/or the coated stabilizing ligand on the nanoparticle possess functionality to bind with the surface of silica.[125] Additional driving force, for example vacuum and electrophoresis

may be required to improve wetting of pores.[126] The advantage in this technique being control over the size of pre-synthesized nanoparticles, which is difficult in inception wetness method where synthesis of nanoparticles is coupled with dispersion. The size of nanoparticle which can access the pore is comparatively smaller than the size of the pore and therefore do not block the pore wall for later usage. The major challenge in this method is to have solvent which allow nanoparticle to adsorb on substrate while preventing them from agglomeration by self-interaction. This leads to the use of dilute solution and hence low loading of the nanoparticles is achieved.
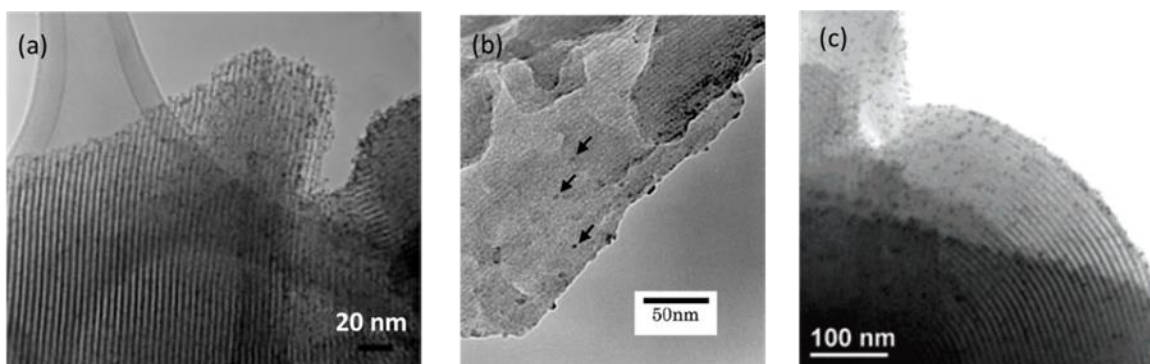


Figure 3.2 (a) Pt/SBA-15 composite where 2.9 nm Pt nanoparticles coated with poly(vinylpyrrolidone) were infused inside SBA-15 of pore size 9 nm using water as a carrier solvent, adapted from Ref. 125 (b) Mesoporous silica infused with CdSe nanoparticles where arrow indicated position of CdSe nanoparticles, adapted from Ref. 124 (c) Mesoporous silica infused with tetraoctylammonium bromide capped Iridium nanoparticles, adapted from Ref. 128.

Somorjai et al. loaded Pt nanoparticles in SBA-15 by both, inception wetness method and by impregnation of pre-synthesized nanoparticles in SBA-15.[125] Although Pt content reach up to 14 wt% in inception wetness method, agglomeration and uncontrolled growth resulted in complete blockage of pores. When Pt nanoparticles in the size range of 1.7 − 7.1 nm were coated with poly (vinylpyrrolidone) and infused in SBA-15 of pore size 9 nm using water as a carrier medium, nanoparticles did not block the pores but loading

was limited to 1 wt%. Figure 3.2(a) shows 2.9 nm Pt nanoparticles infused inside SBA-15, by their method. Hirai et al. infused CdS nanoparticles capped in reverse micelles into thiol functionalized MCM-41, as shown in Figure 3.2 (b).[124] They observed that the loading of nanoparticles decrease as the size of nanoparticle increase or pore size decrease. Although the actual wt% of nanoparticles incorporated was not calculated, but the TEM images hints to a very low loading of nanoparticles (Figure 3.2b). Similarly, gold nanoparticles capped with dodecanethiol[127] and iridium nanoparticles capped with tetraoctylammonium bromide[128] , Figure 3.2(c), were infused into mesoporous silica using toluene and evenly precipitated using supercritical carbon dioxide as an anti-solvent. The loading of the nanoparticles was limited to only 2.5 wt% after infusing and extracting solvent for an extended period of 24 h.

3) One-pot synthesis of nanoparticle-doped mesoporous silica. This method involves simultaneous synthesis of mesoporous silica and metal nanoparticles from a mixture of their precursor solutions templated in a liquid crystalline phase of a surfactant. Metal containing salts, for example $K[AuCl_4]$, $K_2[PdCl_4]$, $K_2[PtCl_4]$ and $Na[M(EDTA)]$ (M = Fe, Co and Cr) are added to a hexagonal mesophase of $C_{12}EO_8$ surfactant along with tetramethyl orthosilicate as a silica precursor.[129] Ageing of the solution followed by drying and calcination leads to the formation of mesoporous silica with embedded metal nanoparticles. Mesoporous silica doped with transition and noble metal nanoparticles[129] and bimetallic[130] nanoparticles have been synthesized by this simple one-step approach which avoids the complexity of wetting and/or agglomeration of nanoparticles in mesoporous silica as seen in previous method. Also, the maximum loading of the nanoparticles that can be obtained while maintaining control of the ordered silica structure

is slightly higher (up to 5 wt%) than the previous methods. The major drawback of this method is the poor control over the size of nanoparticles due to the constraints in simultaneous synthesis of metal particulate and silica framework. The resulting nanoparticles block the pore walls as they are 1-2 pore widths in diameter, hence leading to poor catalytic efficiency by blockage of the pores. The synthesis of silica can also interfere with the synthesis of metal nanoparticles thereby affecting the composition and surface morphology of the nanoparticles. Figure 3.3 shows mesoporous silica doped with Pd, Ir and bimetallic PtCo nanoparticles prepared by this approach. The nanoparticles in all these cases block the pore walls thereby reducing mass transport of reactants toward the inner nanoparticles during catalysis.
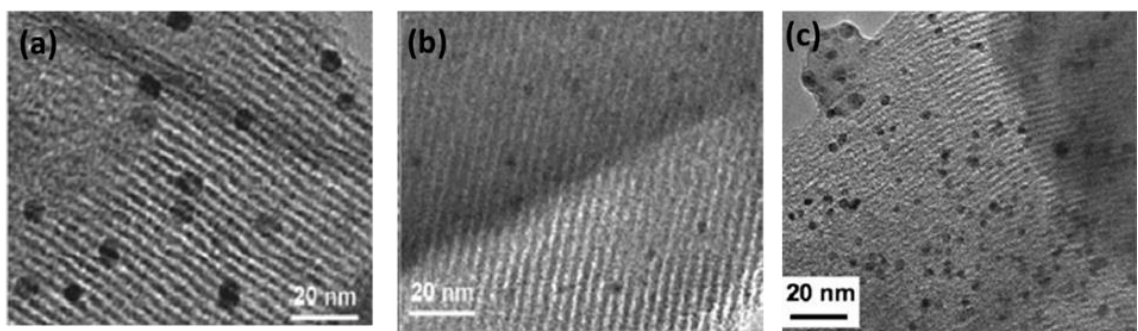


Figure 3.3 TEM images of mesoporous silicates containing (a) Pd, (b) Ir (c) PtCo nanoparticles prepared by one pot synthesis method, (a) and (b) adapted from Ref 129 and (c) adapted from Ref. 130.

4) Synthesis of mesoporous silica in the presence of pre-synthesized nanoparticles. In this method mesoporous silica is synthesized from the surfactant template precursor solution in which surface stabilized nanoparticles are also dispersed. Nanoparticles are synthesized separately and therefore high quality dispersion with uniform and narrow size distribution can be achieved. Somorjai et al. prepared Pt doped SBA-15 by this method

where nanoparticle loading was limited to 3.2 wt%.[131] Pt nanoparticles were synthesized by alcohol reduction method and stabilized by poly(vinylpyrrolidone). The dispersion of stabilized nanoparticles with narrow sized distribution was mixed with surfactant template solution containing TEOS precursor and acid catalyst. Upon aging the solution silicate structure is directed by surfactant micelles which also contains nanoparticles. Drying and calcination leads to Pt nanoparticles doped mesoporous silica, as shown in Figure 3.4(a). The drawback this method is the low loading of nanoparticle incorporated. The presence of high concentration of nanoparticles can significantly disrupt the miceller structure of surfactant leading to the formation of disordered silicate network. In other examples, due to instability of nanoparticle dispersion at low pH required for mesoporous silica synthesis and due to disruption of surfactant structure directing agent, only $10^{12}$-$10^{16}$ gold[132] nanoparticles or platinum[132,133] nanoparticles, Figure 3.4(b) and (c), could be loaded per gram of silica material. Such low concentrations provides only a maximum of 0.0003 wt% of metallic nanoparticles in the mesoporous silica, which therefore will have significantly low catalytic activity.
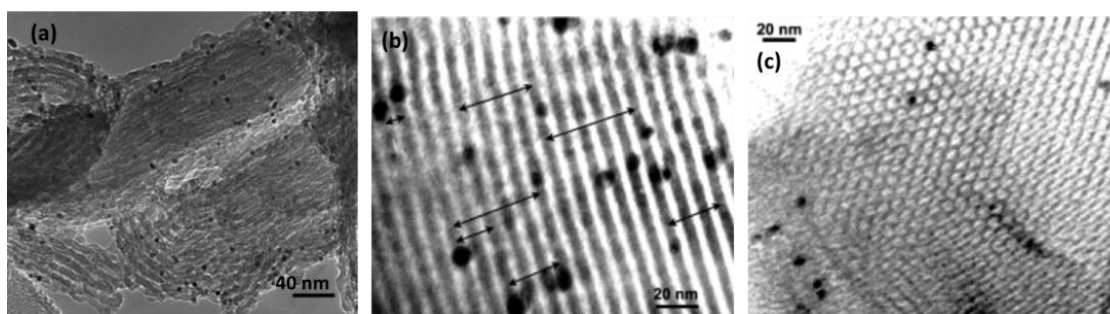


Figure 3.4 (a) SBA-15 mesoporous silica containing 0.77 wt% of 2.9 nm Pt nanoparticles, adapted from Ref. 131 , (b) and (c) mesoporous silica loaded with metallic (Pt or Au) nanoparticles where nanoparticle loading is less than 0.0003 wt%, adapted from Ref 132.

All the four methods described in the previous section to prepare mesoporous silica/metal nanoparticle catalyst have serious drawbacks in achieving high loading on metallic nanoparticles in mesoporous silica matrix while maintaining uniform particle distribution and long range mesopore order. The inception wetness and one-pot synthesis of nanoparticle doped mesoporous silica results in uncontrolled growth of nanoparticles leading to pore blockage and nonhomogeneous distribution of nanoparticles inside the silica matrix. Impregnation of pre-synthesized nanoparticles in mesoporous silica provides catalyst with very low loading or agglomeration of nanoparticles due to difficulty in tuning competing interaction of nanoparticles with solvent and mesoporous silica matrix. To overcome these drawbacks, mesoporous silica was synthesized in the presence of pre-synthesized nanoparticles. High loading of nanoparticles could not be achieved even in this method because self-assembly of the structure directing agent is disrupted in the presence of high concentration of nanoparticles. In all the reports discussed earlier, maximum loading of nanoparticles that could be achieved while maintaining uniform particle distribution, long range order and no pore-blockage was well below 5 wt%.[131]

To date, high metallic nanoparticle loadings (>10 wt%) have received less attention but would be of significant importance in enhancing catalytic efficiency. To the author's knowledge, there is only one example in which metal loading is claimed as high as 14 wt%, but no robust analytical method was used to determine the actual loading[134]. Gupta et al. prepared mesoporous silica/FePt nanoparticle composited by impregnation of pre-synthesized nanoparticles silica. FePt nanoparticles were functionalized with oleic acid and oleyolamine, which are weaker ligands compared to poly(vinylpyrrolidone) and dodecanethiol used in previous studies, and therefore result in exposed nanoparticle surface

which can strongly interacts with silica. To determine metal loading, known amount of mesoporous silica (10 mg) was stirred with known concentration (0.25-2 mg/mL) of ligand stabilized FePt nanoparticles suspension in toluene. After stirring for 10 minutes and filtering with a 0.2 µ PTFE filter, extend of incorporation of FePt crystals was determined by subtracting final mass of nanoparticles recovered in supernatant from initial mass of nanoparticles dispersed in toluene. Although TEM image in Figure 3.5 show high loading of nanoparticles, the method used to determine loading is unreliable as it ignores the mass of nanoparticles that will be stuck in filter membrane, which can be significantly high in case of a weakly bonding ligand. Also, due to weakly stabilizing ligand, thick stacks of nanoparticle layers are adsorbed on the external surface of mesoporous silica particles. These nanoparticles, which obviously will be inactive during catalysis, inadvertently get counted in determination of nanoparticle loading. Moreover, TEM images were provide only for composites with maximum 7.3 wt% loading and not for 14 wt% loading.
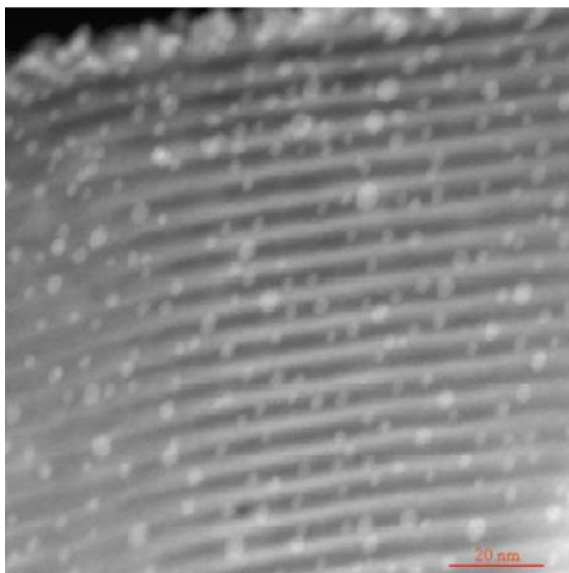


Figure 3.5 High annular dark field TEM image of mesoporous silica containing 7.3 wt% FePt nanoparticles, adapted from Ref. 134

**Objectives of this research.** The goal of this research is to incorporate high loadings of metallic nanoparticles (>10 wt%) into mesoporous silica while maintaining good particle dispersion, long range mesopore order without pore-blockage. Since the methods discussed above possess significant drawbacks in achieving high loadings while maintaining good particle dispersion and long range mesopore order without pore blockage, a novel approach will be utilized that involves preparing mesoporous silica by scCO$_2$ assisted infusion of TEOS into block copolymer templates pre-filled with high loading of metallic nanoparticles. Nanoparticles' surface will be engineered to have favorable hydrogen bonding interaction with the block copolymer, in order to achieve highly filled block copolymer/nanoparticle composites without nanoparticle aggregation. These ordered hybrid composites will then serve as templates for the fabrication of mesoporous silica using method developed by Watkins and co-workers,[12] which involves phase selective condensation of TEOS in the block copolymer template using supercritical carbon dioxide as reaction medium, followed by calcination.

The fabricated mesoporous silica/nanoparticle composites will be characterized using X-ray scattering, electron microscopy and X-ray photoelectron spectroscopy in order to assess the quality of long-range order and weight fraction of nanoparticles incorporated in silica.

## 3.2 Experimental

### 3.2.1 Materials

4-hydroxybenzoic acid (99%, Acros Organics), oleylamine (approximate C18-content 80-90%, Acros Organics), oleic acid (97%, Acros Organics), dioctyl ether (99%,

Sigma Aldrich), iron(0) pentacarbonyl (>99.99%, trace metals basis, Sigma Aldrich), platinum (II) acetylacetonate (97%, Sigma Aldrich), trioctylphosphine (97%, Sigma Aldrich), 1,2-hexadecanediol (>98%, TCI America), hydrogen tetrachloroaurate trihydrate (MP Biomedical, ACS Grade), para-mercaptophenol (Acros Organic, 99%), acetic acid (Fisher Scientific, Glacial), sodium borohydride (Aldrich, Venpure SF), Pluronic® F127 ($EO_{106}$-$PO_{70}$-$EO_{106}$) block copolymer (BASF), para-toluene sulfonic acid (99%, Acros Organics), tetraethyl orthosilicate (99.999%, Sigma-Aldrich), and carbon dioxide ($CO_2$, Merriam Graves, bone-dry grade) were used as received without further purification. Common solvents were purchased from Fisher Scientific and were used as received without further purification. Silicon wafers of (100) orientation (p-type, boron dopant) were obtained from University Wafer.

### 3.2.2   Iron Platinum (FePt) Nanoparticle Synthesis

The synthesis of monodisperse hydrophobic FePt NPs was based on the method previously reported by Sun et al.[26] The resulting alkyl-functionalized NPs could be stably dispersed in solvents with low polarity such as alkanes, alkenes and chlorinated solvents. These NPs were employed as the starting material for the preparation of hydrophilic NPs through a simple one-step ligand exchange reaction with small-molecule ligands such as 4-hydroxybenzoic acid.  Typically, as-synthesized FePt NP solid was mixed with 10x hydrophilic ligand (by weight) in a 20 mL scintillation vial with the targeting solvent (i.e. ethanol).  The reaction was facilitated by 10 minutes of sonication and 1 hour of magnetic stirring to ensure a satisfactory yield.  The vial appeared to be dark yet transparent in just a few minutes, indicating a fast reaction rate.  The exchanged FePt NPs were than

precipitated out with the addition of successive anti-solvent (i.e. hexanes) and collected with centrifugation operating at 5k RPM for 5 minutes. The resulting NP powders could be readily dispersed in polar solvent (such as alcohols, THF, and DMF) and remain stable during long period of observation (over a year). The same purification procedures were applied as necessary until all the excessive ligands were removed. Detailed information of this ligand exchange method and properties of the hydrophilic magnetic nanoparticle are reported, elsewhere.[135] NPs obtained after ligand exchange were dispersed in DMF to obtain a concentration of ~9 mg/ml (attached ligands weight included).

### 3.2.3   Block Copolymer/Nanoparticle Composite Template Fabrication

Silicon substrates (1" x 1") were cleaned by ultrasonication in concentrated sulfuric acid ($H_2SO_4$, Fisher Scientific, ACS Grade) for 15 minutes followed by rinsing with acetone (Fisher Scientific, ACS Grade) and isopropyl alcohol (Fisher Scientific, ACS Grade) and dried under a stream of nitrogen ($N_2$). Solution containing Pluronic® F127 (BCP template), para-toluene sulfonic acid (acid catalyst for hydrolysis and condensation od silica precursor), and pre-synthesized FePt nanoparticles in DMF were spin coated on cleaned silicon substrate. Solution composition and spin coating parameters are detaild along with the discussion  section.

### 3.2.4   Supercritical Carbon Dioxide Processing

Mesoporous silica films doped with NPs were prepared by exposing the amphiphilic block copolymer templates doped with FePt NPs to a solution of tetraethyl orthosilicate (TEOS) in supercritical carbon dioxide ($scCO_2$) within a high pressure reactor

at 60 °C and 125 bar.  The high pressure reactor, ~ 160 mL in volume, is constructed from two stainless steel opposed ended hubs sealed with a graphite ring (55 ft-lb torque) purchased from Grayloc® Products.  Heating bands (Watlow®) are connected to the outside of the reactor walls to control the gas temperature.  The top reactor hub is drilled to have 4 ports; one to measure internal pressure, one to measure internal temperature, one for gas inlet and one for gas outlet.  For the Pluronic® F127 solution containing pre-synthesized NPs, 20 µL of TEOS was directly placed within the high pressure reactor along with 300 µL of de-ionized water, each in separate Vespel® containers, prior to sealing. Once the reactor was sealed and heated to a gas temperature of 60 °C, an equilibrium time of 2 hours was observed to allow the polymer templates sufficient annealing and water uptake.  $CO_2$ was injected with a high pressure syringe pump (ISCO, Model 500 HP) at a rate of 2 – 3 mL/minute.  Once the correct pressure was reached (1800 psi), a soak time of 2 hours at 60 °C.  The reactor was then de-pressurized within 20 minutes to ambient pressure.  Samples were thermally degraded at 400 °C for 6 hours with a ramp rate of 1.56 °C/minute.

### 3.2.5   Characterization

Film thicknesses were measured with a Filmetrics F20 Thin Film Measurement System and reported values were an average of 5 measurements over the entire surface with a deviation of ± 5 nm. Transmission electron microscopy (TEM) samples were prepared by scraping mesoporous silica from the substrate, grinding via mortar and pestle, suspended with ethanol and transferred to a holey-carbon-coated copper grid to be analyzed with a JEOL 2000FX II operating at 200kV. Small Angle X-Ray Scattering (SAXS) was

performed on Rigaku-Molecular Metrology SAXS equipment using copper (Cu) Kα X-rays (0.1542 nm) operating at 45kV and 40mA. X-ray diffraction (XRD) and low-angle XRD (LAXRD) were performed on a PANalytical X'Pert diffractometer, using copper (Cu) Kα X-rays (0.1542 nm) operating at 45kV and 40mA. X-ray photoelectron spectroscopy (XPS) measurements were conducted on a Quantum 2000 scanning ESCA microprobe (Physical Electronics Inc.) using Al Kα radiation (1486.6eV). Survey spectrum was acquired in the binding energy range of 0-1100eV using 187eV pass energy and 1.6eV step size. For depth composition analysis samples were sputtered with Ar+ ion-sputtering gun operating at 1keV and 20nA. After each sputtering event, narrow scans were acquired using pass energy and step size of 46.9eV and 0.2eV respectively. Raw XPS data was analyzed using MultiPak V6.1A (Physical Electronics Inc.) software.

## 3.3   Results and Discussion

The Pluronic® family of block copolymers are amphiphilic tri-block copolymers that consist of hydrophilic poly(ethylene oxide) (PEO) and hydrophobic poly(propylene oxide) (PPO) segments.  To incorporate significant weight fractions of pre-synthesized FePt NPs into the Pluronic® block copolymer, a favorable interaction between the pre-synthesized NP and Pluronic® PEO segment must be established. The Watkins group recently demonstrated that high loadings of pre-synthesized metal and semiconducting NPs located within the PEO segments of Pluronic® copolymers could be achieved to yield well-ordered composites by exploiting strong interactions between the NP ligands and the PEO segment. For example, Lin et al., showed that gold (Au) NPs decorated with para-mercaptophenol as the hydrogen bond donating ligand increased the segregation strength and enabled Au

NP loadings as high as 30 wt% in the well-ordered composite.[5] This strategy has been further extended to incorporate similar loadings of FePt NPs decorated with the hydrogen bond donating 4-hydroxybenzoic acid within the PEO segment of Pluronic® F127, $PEO_{106}$-b-$PPO_{70}$-b-$PEO_{106}$, copolymer template which is known to phase separate into a cylindrical morphology, both in bulk[27,28] and thin film samples.[29]

Figure 3.6 cartoon of FePt NP decorated with mercaptophenol ligand and TEM image of synthesized FePt NPs with a particle size of ~2nm. Figure 3.7 shows SAXS of bulk Pluronic® F127/FePt NP composites at various wt% loadings of NPs (with respect to composite weight). From the SAXS data it is seen that FePt NPs bearing hydroxyl terminated ligands are capable of inducing order in otherwise disordered Pluronic® F127. Because of the favorable interactions, loading of the NPs could be increased up to 40 wt% without aggregation of the NPs — no aggregation peak was observed in SAXS at higher $q$ values.
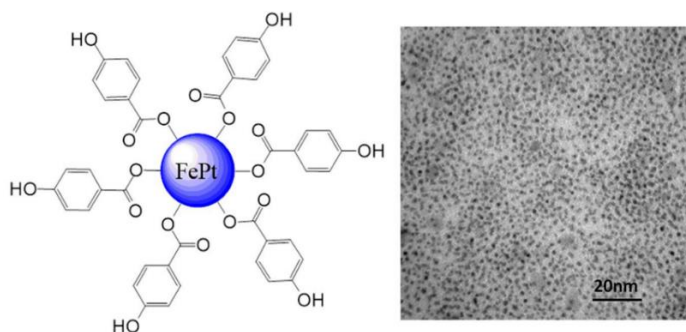


Figure 3.6 Cartoon depicting the FePt nanoparticle decoraated with 4-hydroxybenzoic acid ligands (left). TEM image of the as synthesized FePt nanoparticles functionalized with 4hydroxybenzoic acid ligands (right) with particle size ~2nm. Reproduced from Ref. 136 with permission from The Royal Society of Chemistry.
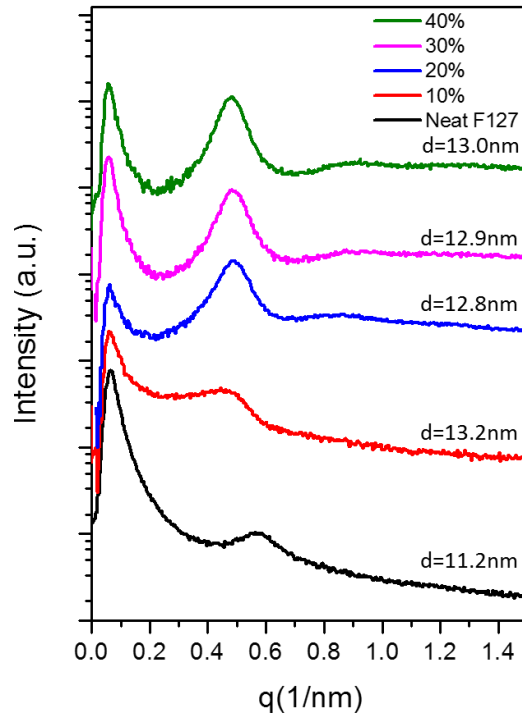
Figure 3.7 SAXS of Pluronic F127/FePt nanoparticle composites with various loading of FePt nanoparticles. Samples were annealed at 60 °C for 24 h and SAXS was performed at 80 °C.

Figure 3.8 illustrates how the desired mesoporous silica with high loadings of pre-synthesized NPs was produced. The process begins by spin-coating a solution of NPs with Pluronic® F127 and para-toluene sulfonic acid (PTSA), which is a strong organic acid used to promote the hydrolysis and condensation of the silica network, to create a 400 – 500 nm thin films. The solutions consisted of 10 wt% solids (Pluronic® F127, pre-synthesized NPs and PTSA) and 90 wt% DMF solvent for the case of FePt NPs. Concentration of the pre-synthesized NPs ranged from 5 wt% to 25 wt% with respect to Pluronic® F127 while the concentration of the PTSA was held constant at 15 wt% with respect to all solid materials. The solutions were stirred at room temperature for 15 minutes to ensure the components were sufficiently mixed. The solutions were then directly spin-coated in an

68

air environment, through a 0.2 μm poly(tetrafluoroethylene) (PTFE) filter, on a cleaned silicon wafer for 90 seconds at 3000 rpm. The thin films showed no signs of crystallization, de-wetting or macro-phase separation.
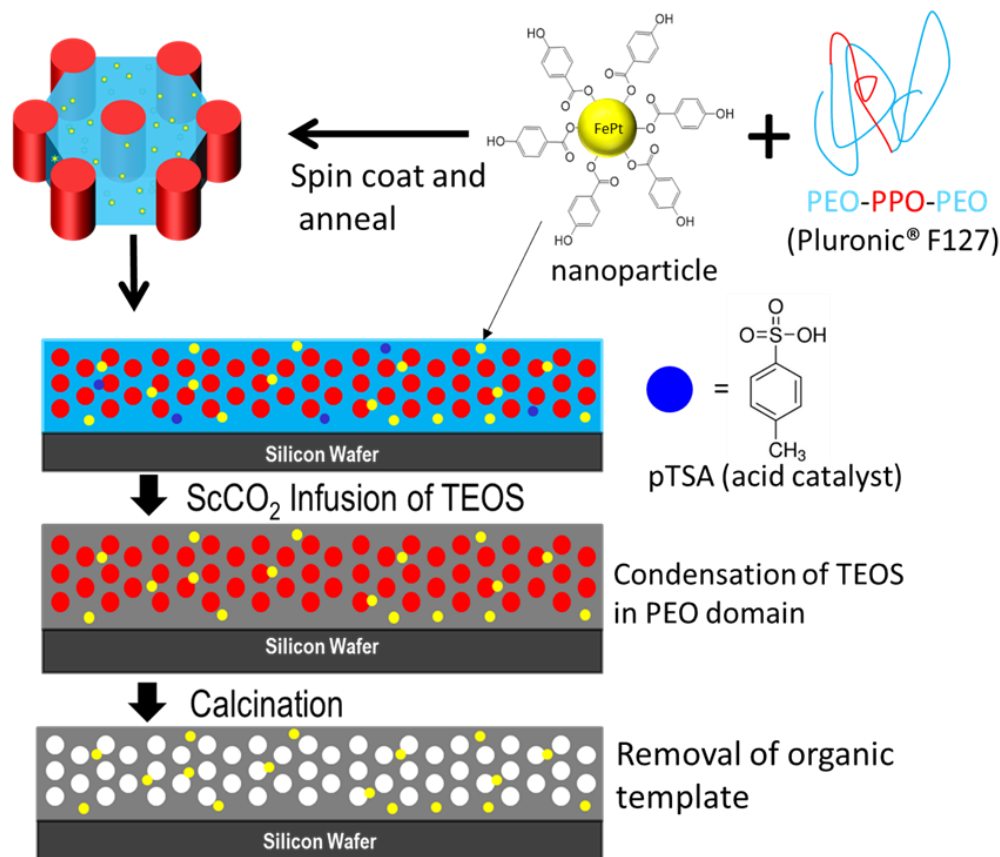


Figure 3.8 Illustration showing the fabrication of mesoporous silica loaded with FePt nanoparticles.

To template the mesoporous silica around the pre-synthesized NPs, the thin film samples were exposed to a humidified solution of scCO$_2$ containing the silicon alkoxide precursor of tetraethyl orthosilicate (TEOS) at 60 °C and 125 bar for 2 hours. The unique aspect of templating mesoporous silica through the use of scCO$_2$ processing is that the thin film block copolymer template formation is separated from the condensation of the silica

69

precursor. This allows the block copolymer template to retain the morphology created during the spin-coating and annealing steps and remain unperturbed during the formation of the silica network. The generation of the mesopores and removal of organic material is simultaneously achieved by thermal degradation. Calcination was performed with a 1.56 °C/minute ramp rate from room temperature to 400 °C, held at 400 °C for 6 hours and brought back to room temperature with a ramp rate of 1.56 °C/minute. Fabrication of mesoporous silica through the $scCO_2$ processing has also been characterized to show that an interpenetrating network (IPN) structure is formed from the micropores created during the thermal degradation of the PEO blocks[30]. Such characteristics of the mesoporous silica, i.e. high degree of wall porosity, created through $scCO_2$ processing, once doped with pre-synthesized NPs, make for unique substrates that are ideal for use in catalysis and sensing applications.
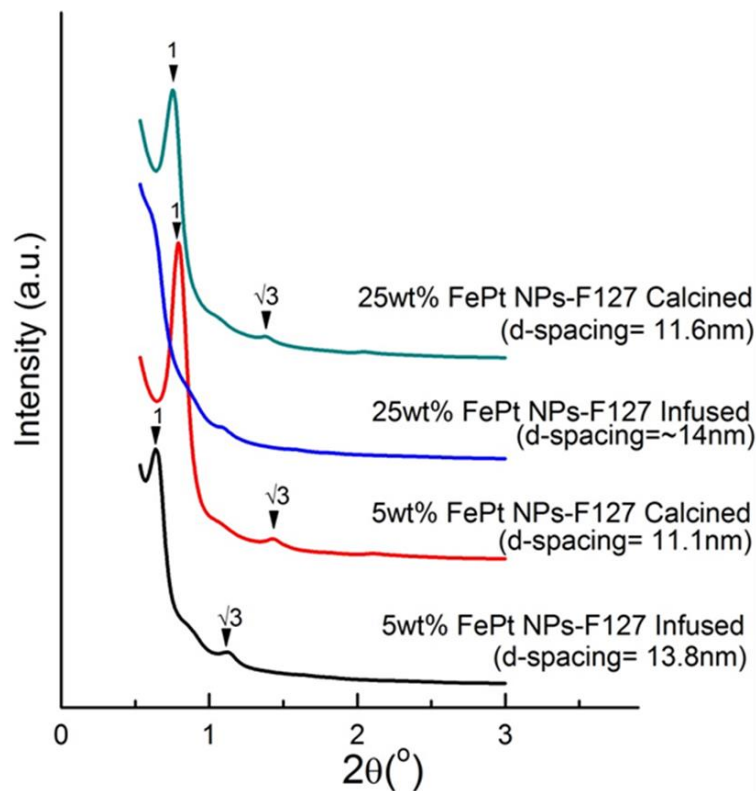
Figure 3.9 Low-angle X-ray diffraction (LAXRD) for mesoporous silica containing pre-synthesized FePt nanoparticles. Weight percents of FePt nanoparticles is with respect to Pluronic® F127. The terms of infused and calcined refer to the presence of organic materials (infused) and to the presence of no organic material (calcined). Reproduced from Ref. 136 with permission from The Royal Society of Chemistry

Mesoporous silica samples containing pre-synthesized FePt NPs of 5 wt% and 25 wt%, with respect to the Pluronic® F127 template, were created. X-ray diffraction (XRD) was used to evaluate the structure of the mesoporous silica/NP composites and the data is provided in Figure 3.9.[136] For composites containing silica/NPs/polymer, a well-ordered hexagonal structure was observed with domain spacing between 13.2 nm and 14.0 nm. When the polymer material was removed from the composite, yielding only mesoporous silica and NPs in the composite, a well-ordered hexagonal structure was observed but the domain-spacing was reduced to between 10.9 nm and 11.6 nm. The difference between

71

the domain-spacings between the calcined and uncalcined samples corresponds to the shrinkage in the lattice parameters, by ~ 20 %, due to removal of the polymer template and organic material (e.g. NP ligands) as well as further condensation of the silica matrix. Also, the increase in scattering intensity in the composite without the polymer template, when compared to the composite with the polymer template, is as expected due to the increase in electron density differences between the two composites, i.e. upon removal of the minor block copolymer domains to yield the mesopores.
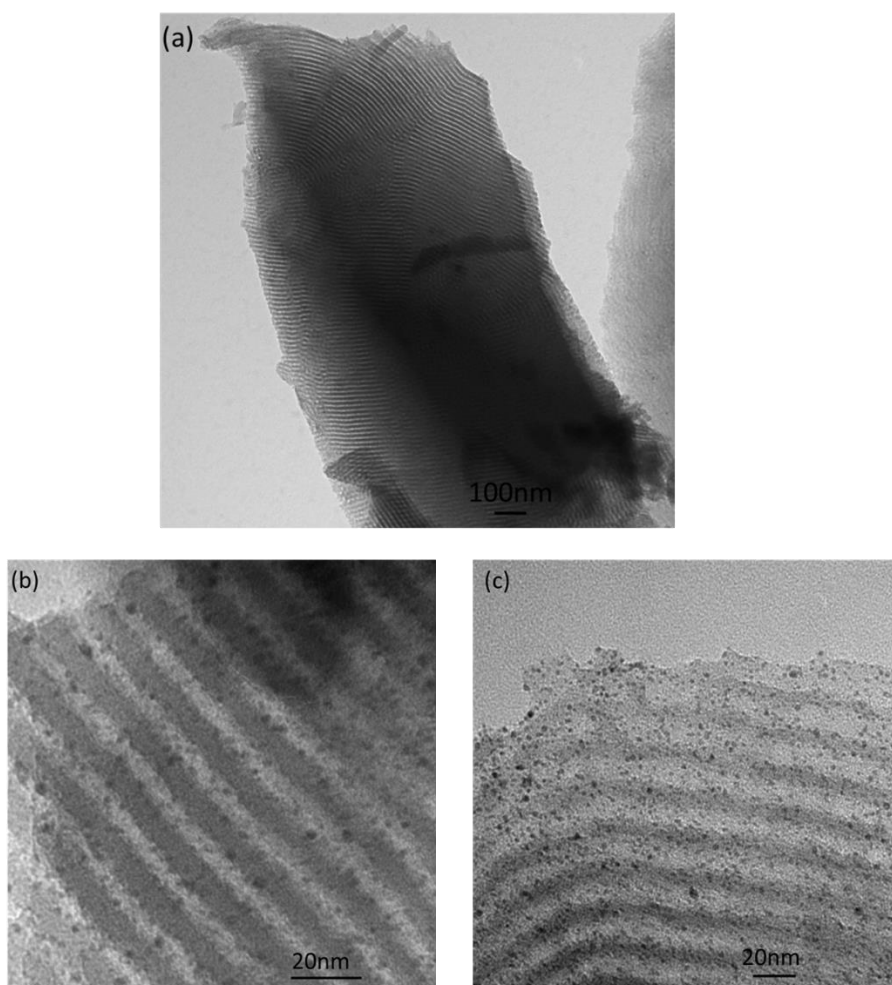


Figure 3.10 TEM images of mesoporous silica created from Pluronic® F127 containing 25 wt% pre-synthesized FePt NPs (a) low magnification image showing presence of cylindrical mesopores (b and c) high magnification images displaying FePt NPs within mesoporous silica. Reproduced from Ref. 136 with permission from The Royal Society of Chemistry.

72

Electron microscopy was used to confirm the presence of the NPs within the mesoporous silica. The transmission electron microscopy (TEM) images Figure 3.10 show the successful incorporation of pre-synthesized NPs into mesoporous silica while maintaining the presence of mesopores with diameters of 5 – 6 nm for mesoporous silica samples containing 25 wt% of pre-synthesized NPs. The darkest areas of the electron micrographs correspond to the NPs, while the lighter gray areas correspond to the silica and the white areas correspond to the mesopores. High magnification TEM images, provided in Figure 3.10(b) and (c), confirms the presence of NPs and suggests that the NPs are predominately located within the mesopore walls rather than in the mesopores themselves. This partitioning of NPs within the mesoporous silica walls is consistent with the initial partitioning of NPs within the hydrophilic (PEO) segment of the Pluronic® block copolymer template, only now the hydrophilic segment of the Pluronic® block copolymer template is infused with silica from the hydrolysis and condensation of TEOS during scCO$_2$ processing. There is no evidence of coarsening or aggregation of the FePt NPs during calcination, indicating that the particles are stable and remain well distributed during template removal and further silica network condensation. XPS survey spectrum (Figure 3.11) of mesoporous silica created from Pluronic® F127 template containing 25 wt% pre-synthesized FePt NPs shows Auger and photoelectron features of silicon (Si), oxygen (O), iron (Fe) and platinum (Pt) along with carbon (C) as impurity on the surface. Figure 3.12 shows narrow scans of these elements after sputtering for the time indicated in the legend. Composition analysis after each sputtering event confirms presence of nanoparticles in the bulk of the film. No carbon impurity was observed after the first 30seconds of sputtering. Composition profiles with sputtering time are plotted in Figure 3.13, the average FePt NPs

73

concentration in the bulk of the film with respect to silica is 15 wt%. This is consistent with the presence of the ligands on FePt NPs, replacement of low density Pluronic® F127 template with higher density silica matrix.
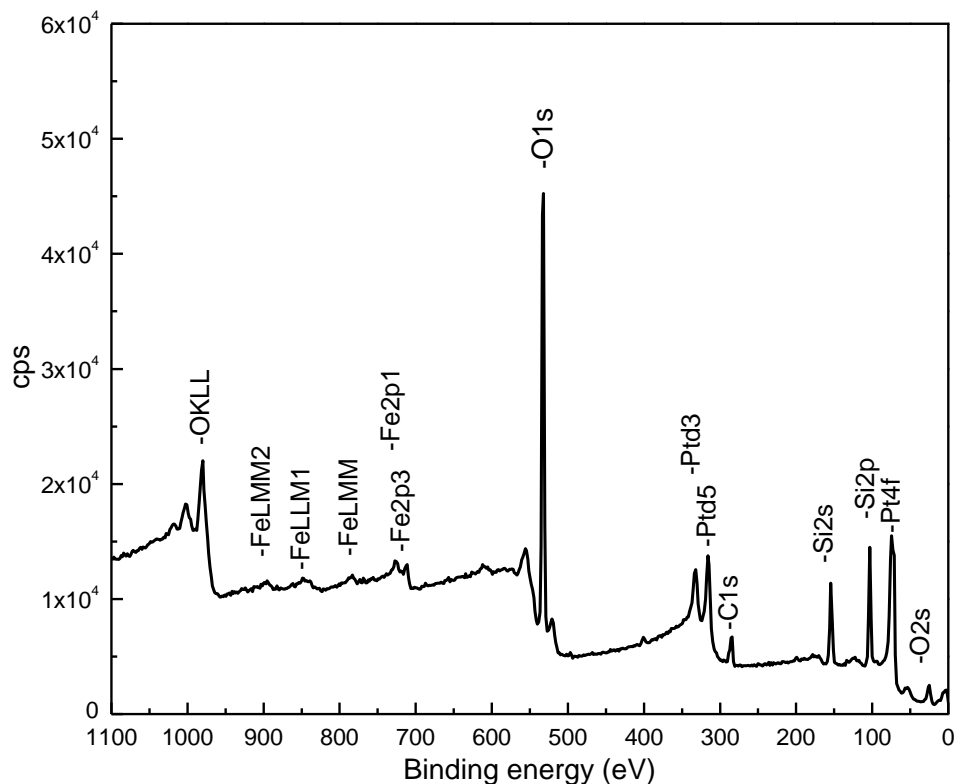


Figure 3.11 . XPS survey spectrum of mesoporous silica created from Pluronic® F127 template containing 25 wt. % pre-synthesized FePt NPs. Reproduced from Ref. 136 with permission from The Royal Society of Chemistry
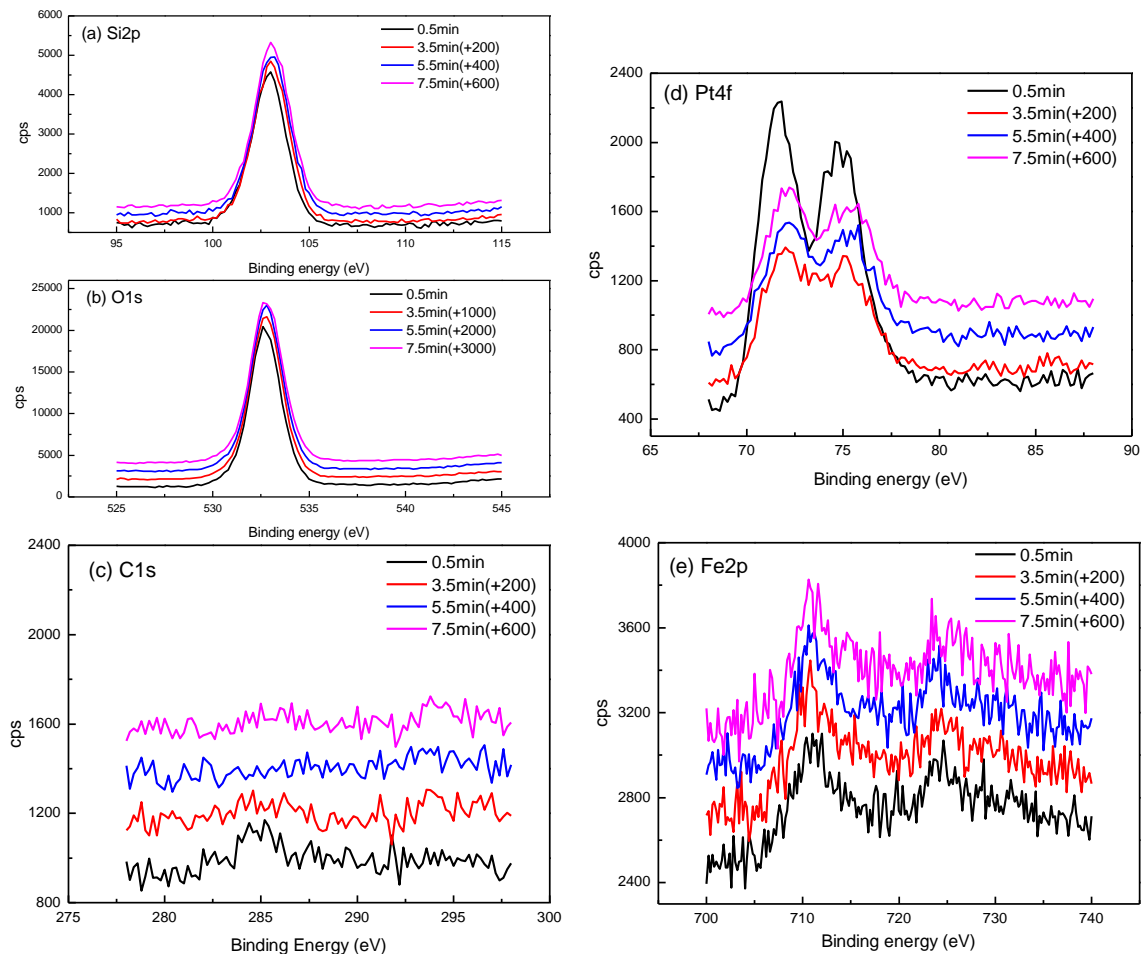
Figure 3.12 Narrow scans of mesoporous silica created from Pluronic® F127 template containing 25 wt. % pre-synthesized FePt NPs after different sputtering time: (a) Si2p; (b) O1s; (c) C1s; (d) Pt4f; (e)Fe2p. Legend represents time for which sputtering was done before data acquisition. Number in bracket next to legend is shift in y axis for clear representation. Reproduced from Ref. 136 with permission from The Royal Society of Chemistry.
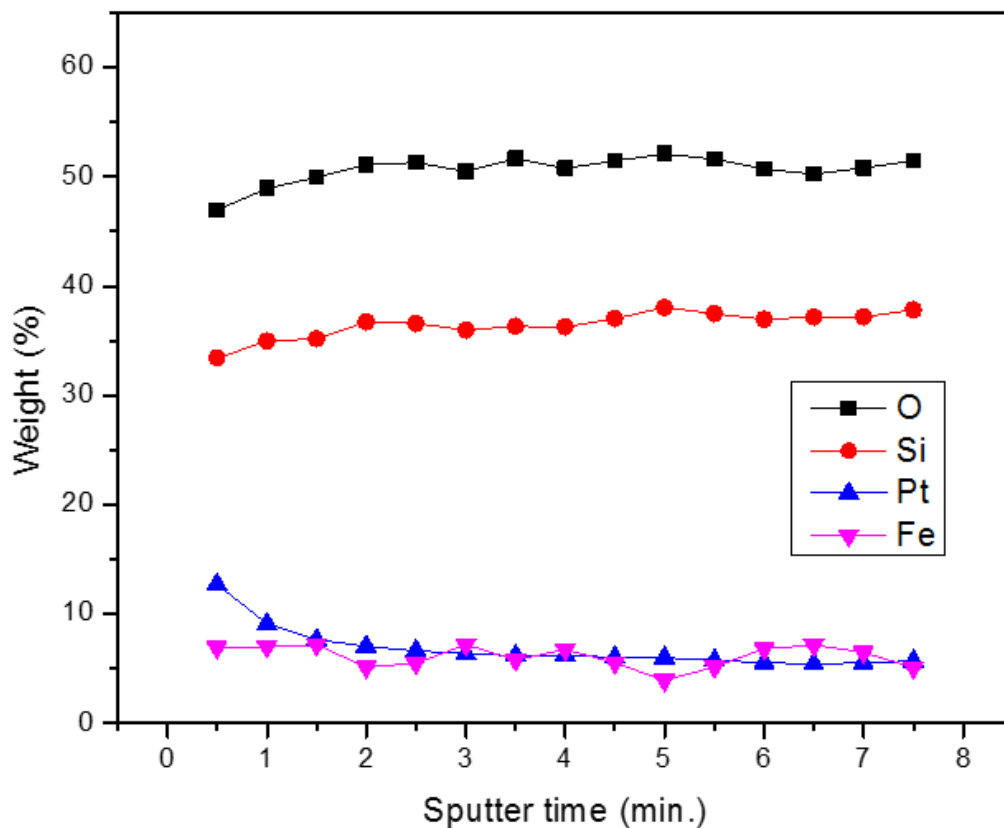
Figure 3.13 XPS composition profiles vs sputtering time for mesoporous silica created from Pluronic® F127 template containing 25 wt. % pre-synthesized FePt NPs. Reproduced from Ref. 136 with permission from The Royal Society of Chemistry

## 3.4  Conclusion

A method for the preparation of mesoporous silica/nanoparticle composites containing high concentrations of NPs within the silica walls is presented.  2-3 nm FePt NPs decorated with 4-hydroxybenzoic acid ligands selectively hydrogen bond to the hydrophilic segment of Pluronic® F127 enabling the generation of templates with high concentrations of NPs located selectively within the PEO domain. The NPs were then encapsulated by the generation of silica by the phase selective condensation of silica from TEOS within the PEO/NP domain of the $CO_2$ swollen composite template. Calcination

removed both the template and the NP ligands yielding mesoporous silica loaded with NPs. X-ray scattering confirmed the presence of hexagonally ordered mesopores in the silica/NP composites. Electron microscopy confirmed that the NPs reside primarily within the walls of the mesoporous silica allowing the mesopores to be free of obstructions to the transport of materials. At a FePt NPs loading of 25 wt%, with respect to the Pluronic® template, the FePt NPs were stable during preparation of the mesoporous silica and remained well dispersed and less than 3 nm in diameter. This procedure described here could be applied to any number of NPs, although ripening may be observed during calcination for NPs with low melting points. In the latter case other means of template removal such as plasma processing may be required.

The novel scheme elaborated here to fabricate mesoporous silica/metallic nanoparticle composites useful in catalysis and other applications deliver mesoporous silica with high loading of nanoparticles (>10 wt%) while maintaining long range order, well ordered porosity and good nanoparticle dispersion ― attributes otherwise difficult to achieve using the methods explored in the literature.

## 3.5   Acknowledgements

CHAPTER 4

# HIERARCHICALLY POROUS SILICA MONOLITHS WITH WELL-

# ORDERED MESOPORES INTERCONNECTED BY MACROPORES

## 4.1  Introduction and Objectives

Microporous (pore diameter less than 2 nm) and mesoporous materials (pore diameter between 2 to 50 nm) owing to their high surface area and well-ordered porosity are useful for applications in catalysis, separation and filtration, as discussed in detail in Chapter 3, Section 3.1 of this dissertation. While invention of mesoporous and microporous materials has significantly advanced the field of catalysis and separation, it is further desirable to complement mesopores and micropores with macropores (pores with size greater than 50 nm) to enhance properties such and mass transport and diffusion during catalysis and separation.  Such dual porosity structure is also often referred as hierarchically porous structure due to the presence pores at two discrete length scales.

Early research to create bimodal porosity focused on generating two and more different pore sizes in mesopore range.  Approaches used to obtain bimodal mesoporosity are biomimetic synthesis in weakly ionic solutions,[137] post-synthesis hydrothermal treatments in presence of ammonia,[138] crosslinking reactions[139] and incorporation of synthetic additives.[140-142] Zhang et al. synthesized mesoporous silica with controllable bimodal pore size distribution with cetyltrimethylammonium bromide as chemical template for small mesopore and silica gel as a template for large mesopore.[143] While small mesopores provide selectivity and large surface area, the purpose for large mesopores is to

provide better transport. Hierarchically porous structures, involving the combination of micropores and mesopores[144,145] as well as micropores and macropores[146-148] have been investigated. The focus of this research is on hierarchically porous silica involving the combination of mesopores and macropores.

Hierarchically porous silica with mesopores and macropores have been synthesized earlier by coating structure directing surfactant solutions containing silica precursors over macro-templates comprising connected macropores, followed by condensation and calcination steps. Sacrificial macro-templates exploited in combination with usual mesoporous structure directing templates are self-assembled polystyrene beads and latex spheres,[149-154] emulsions,[155-158] polymeric membranes,[159-162] inorganic slats[163] and biological skeletons.[164] The well-ordered mesoporosity provides selectivity and high surface areas whereas connected macropores dictated by sacrificial macro-templates provides pathways for enhanced mass transport and diffusion during catalysis and separation. Figure 4.1 shows electron microscopy images of hierarchically porous silica with macropores (left image) and with mesopores (right image) prepared during the natural creaming process of an oil-in-water emulsion.[155]
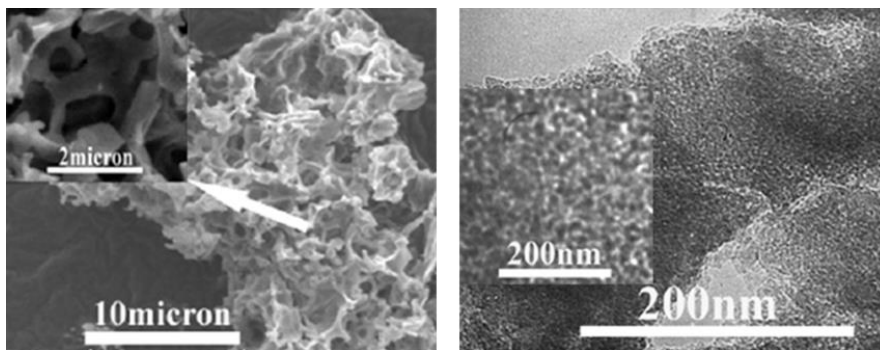


Figure 4.1 Electron microgrpahs at two different order of scale of a hierarchically porous silica sample synthesized during the natural creaming process of an oil-in-water emulsion. Left image shows macropores and right image shows mesopores. Adapted from Ref. 155

Supercritical fluids have been earlier used in fabricating porous metals and metal oxides structures by a technique termed "nanoscale casting" which involves conformal and easy deposition of metal/metal oxide precursors around carbon fibers by the means of supercritical carbon dioxide followed by calcination.[165-168] Supercritical carbon dioxide is specifically advantageous owing to its easily achievable critical point, zero surface tension and gas like transport properties, which helps in conformal deposition of precursor throughout the template. Supercritical carbon dioxide is also a good solvent for silica precursor. In this research we develop a technique to fabricate 3D hierarchically porous silica monoliths in prescribed shapes using a supercritical carbon dioxide processing method. The method that is used to fabricate hierarchically porous silica is analogous to "nanoscale casting" technique as silica precursor is selectively condensed to form a porous structure.

**Objectives of this research.** The objective of this research is to fabricate hierarchically porous silica with well-ordered mesopores connected with/by macropores. The supercritical carbon dioxide infusion method developed by Watkins et al. to make thin film mesoporous silica (as detailed in Chapter 3, section 3.1) will be utilized in combination with inexpensive macroporous templates, for example cellulose filter paper and polystyrene foam, to fabricate 3D hierarchically porous silica with interconnected mesopores and macropores. Hierarchically porous silica will be characterized using electron microscopy, X-ray scattering and nitrogen physisorption in order to access the quality of porous structure, long range order in mesopores, porosity and surface area of the mesopores.

Till now, the novel supercritical carbon dioxide infusion method developed by Watkins et al. has as only been used to fabricate high quality (long-rage ordered) mesoporous thin films. Bulk mesoporous silica, that also has well-ordered porosity, has not yet been shown by this method. This is the first attempt to fabricate bulk mesoporous using this method that has also has long-range mesopore order. Surface area of the bulk mesoporous silica made using this method will also be reported for the first time.

## 4.2   Experimental

### 4.2.1   Materials

Pluronic® F127 (EO$_{106}$-PO$_{70}$-EO$_{106}$) block copolymer (BASF), benzene-1,2,3,4,5,6,-hexacarboxylic acid (>98.0%, TCI America) para-toluene sulfonic acid (99%, Acros Organics), tetraethyl orthosilicate (99.999%, Sigma-Aldrich), de-ionized water (Fisher Scientific, Optima) and carbon dioxide (CO$_2$, Merriam Graves, bone-dry grade) were used as received without further purification. Cellulose filter paper (Whatman Qualitative Filter Paper, Grade No. 1) was purchased from Sigma-Aldrich. The polymeric macroporus sponge is typical of that found in packaging cardboard boxes.

### 4.2.2   Template Preparation

Benzene-1,2,3,4,5,6-hexacarboxylic acid (BHCA) and Pluronic® F127 (F127) or Pluronic® F108 (F108) were dissolved in water in 10/90, 20/80 and 0/100 weight ratios of BHCA/Pluronic®. The concentration of solution ranged between 1 to 10 wt% (BHCA+Pluronic®) in water. To this solutions 1 to 15 wt% (with respect to the total weight of BHCA and Pluronic® weight) of para-toluene sulphonic acid (PTSA; acid catalyst) was

dissolved. Filter paper and packaging sponge (macroporous templates) were soaked in these solutions for 10 minutes. During soaking, packaging foam was squeezed in solution to remove trapped air bubbles and fill its pores with the solution. Cellulose filter paper is very hydrophilic and easily gets wet with the solution. Soaked filter paper and packaging foams were then dried at room temperature. Thermal annealing in vacuum at 80-85 °C (12 h or 24 h) was performed to achieve microphase separated ordered morphology in BHCA/Pluronic® templates. At this point templates were ready to be used for $scCO_2$ infusion process.

### 4.2.3  Supercritical Carbon Dioxide Processing

Templates were exposed to a solution of tetraethyl orthosilicate (TEOS) in supercritical carbon dioxide ($scCO_2$) within a high pressure reactor at 60 °C and 1800 psi (12.4 MPa). The high pressure reactor, ~ 160 mL in volume, is constructed from two stainless steel opposed ended hubs sealed with a graphite ring (55 ft-lb torque) purchased from Grayloc® Products. Heating bands (Watlow®) are connected to the outside of the reactor walls to control the gas temperature. The top reactor hub is drilled to have 4 ports; one to measure internal pressure, one to measure internal temperature, one for gas inlet and one for gas outlet. Templates were places in reactor on a curved glass dish (to avoide direct contact with hot reactor surface) along with excess (~500 µL) of de-ionized water and TEOS (20-500 µl) each in separate Vespel® containers, prior to sealing. Once the reactor was sealed and heated to a gas temperature of 60 °C, an equilibrium time of zero to 2 hours was observed. $CO_2$ was injected with a high pressure syringe pump (ISCO, Model 500 HP). Once the correct pressure (1800 psi) was reached, a soak time of 2 hours at 60 °C

was observed. The reactor was then de-pressurized within 20 minutes to ambient pressure. Samples were thermally degraded at 650 °C for 6 hours with a ramp rate of 1.56 °C/minute.

### 4.2.4   Characterization

Scanning electron microscopy was performed on a field emission scanning electron microscope (FEI Magellan 400), operating at 2kV. Samples were gold sputtered for 1 minute before FESEM Small Angle X-Ray Scattering (SAXS) was performed on Rigaku Molecular Metrology SAXS equipment using copper (Cu) Kα X-rays (0.1542 nm) operating at 45kV and 40mA. Transmission electron microscopy (TEM) samples were prepared by grinding a small amount of sample using mortar and pestle, suspending the grinded material in ethanol and drop casting the suspension on a holey-carbon-coated copper grid to be analyzed with a JEOL 2000FX II operating at 200kV. Nitrogen adsorption/desorption experiments were (for surface area and porosity measurement) performed on Quantachrome autosorb IQ gas sorption instrument. Prior to obtaining adsorption/desorption isotherms at room temperature, samples were degassed at 200 °C for 2 hours in vacuum (on the instrument). Isotherms were analyzed using Quantachrome® ASiQwin$^{TM}$ version 1.02 software for determination of BET surface area and BJH pore-size distribution.

## 4.3   Results and Discussion

The Pluronic® family of block copolymers are amphiphilic triblock copolymers that consist of hydrophilic poly(ethylene oxide) (PEO) and hydrophobic poly(propylene oxide) (PPO) segments. Pluronic® F127 ($PEO_{106}$-b-$PPO_{70}$-b-$PEO_{106}$) triblock copolymers

blended with BHCA and PTSA are be used as a template to obtain mesoporous silica structure. BHCA is used to enhance long-range order of the template and PTSA acts as a catalyst for hydrolysis and condensation of TEOS. Schematics for the formation of hierarchically porous silica is laid out in Figure 4.2. Solution of Pluronic® F127/BHCA/PTSA in water is casted on macroporous supports, dried and annealed at 85 °C for 24 hours in oven to obtain an ordered microphase separated morphology in Pluronic® F127/BHCA/PTSA coating. Annealing was not performed in some cases. Coated macroporous templates are placed in the reactor and TEOS silica-precursor is infused into them in the presence of humidified $scCO_2$. TEOS selectively condense in the PEO phase where acid catalyst (PTSA) is present. After infusion, templates are then thermally degraded in a calcination oven at 650 °C to obtain a porous structure.
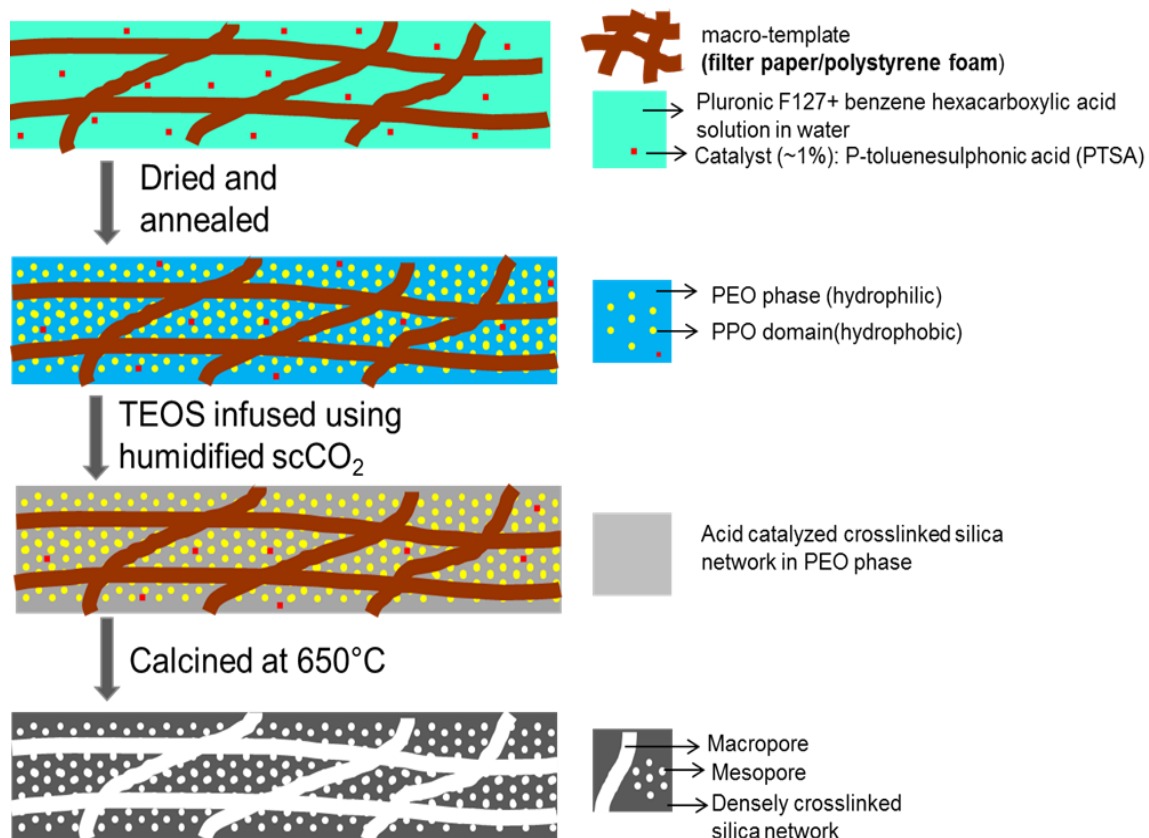
Figure 4.2 Illustration showing the fabrication of hierarchically porous silica by supercritical carbon dioxide (scCO$_2$) assisted infusion of tetraethyl orthosilicate (TEOS) into an ordered small-molecule-additive/block copolymer template casted on a macroporous organic template, followed by calcination.

Figure 4.3 provides SEM images and digital photographs (insets) of filter paper and packaging sponge with pores at two different length scales, that are used as macroporous supports for templating mesoporous silica. Initial experiments were carried out using only Pluronic® F127 as a template for mesoporous structure (without BHCA), as used earlier in case of mesoporous silica thin films fabricated on silicon wafer by Pai et al.[12] Pluronic® F127 template containing 15 wt% of PTSA were casted on cellulose filter paper from a 10 wt% solution. Templates were placed in the reactor along with excess of TEOS and water (350 µl each in separate Vespel® containers), before sealing the reactor. The reactor was

then heated to 60 °C and $CO_2$ was injected with a rate of 2-3 ml/min for 2 h to 1800 psi pressure. After observing a 2 h soak time at this pressure, the reactor was depressurized and the samples were calcined. Figure 4.4 shows the TEM images of sample with regions of ordered and disordered porosity. SEM characterization of the template after TEOS infusion step showed a thick skin layer of silica deposited on the surface (Figure 4.5). This pore-less silica deposition is a result of rapid hydrolysis and condensation of TEOS on the surface having high concentration of PTSA, which may have occur in two stages of the process: first, after sealing the reactor, TEOS molecules dissolve in air rapidly hydrolyze and condense on PTSA rich surface. Second, when $CO_2$ is injected, TEOS dissolves in the gas and precipitate at the same time when it is infused in the polymer matrix.
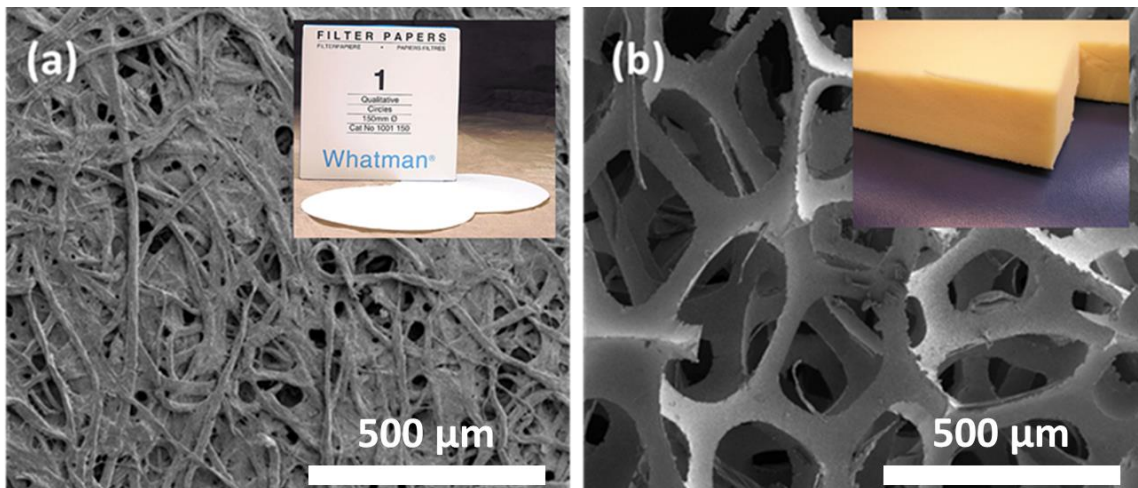


Figure 4.3 Scanning electron microscopy (SEM) images of (a) cellulose filter paper (b) packaging sponge that serves as macroporous templates. Inset in (a) shows digital photograph of the circular filter paper pieces (1500 mm in diameter) and inset in (b) shows digital photograph of ~5 cm thick packaging sponge.
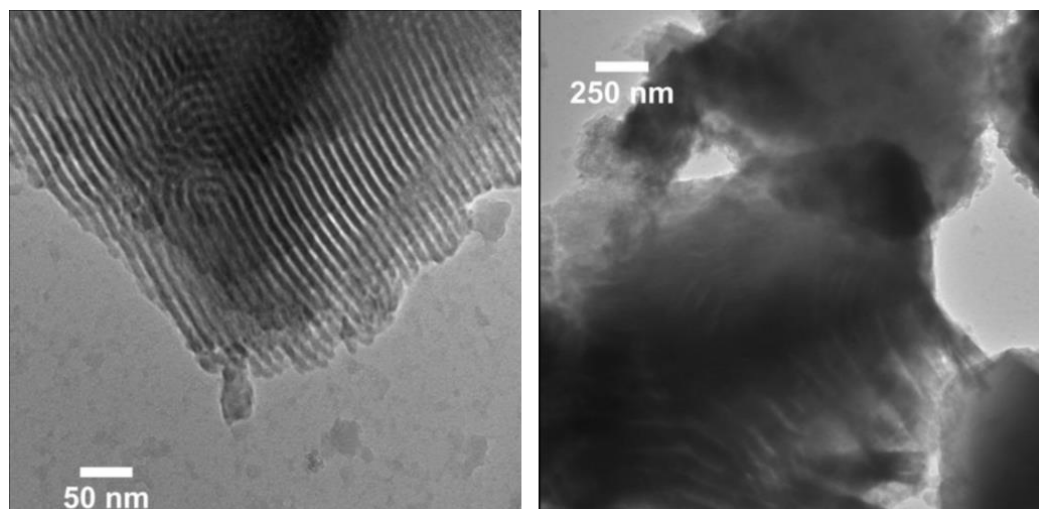
Figure 4.4 TEM images porous silica created using 85/15 (wt/wt) Pluronic® F127/p-toluene sulphonic acid (PTSA) template coated on cellulose filter paper.
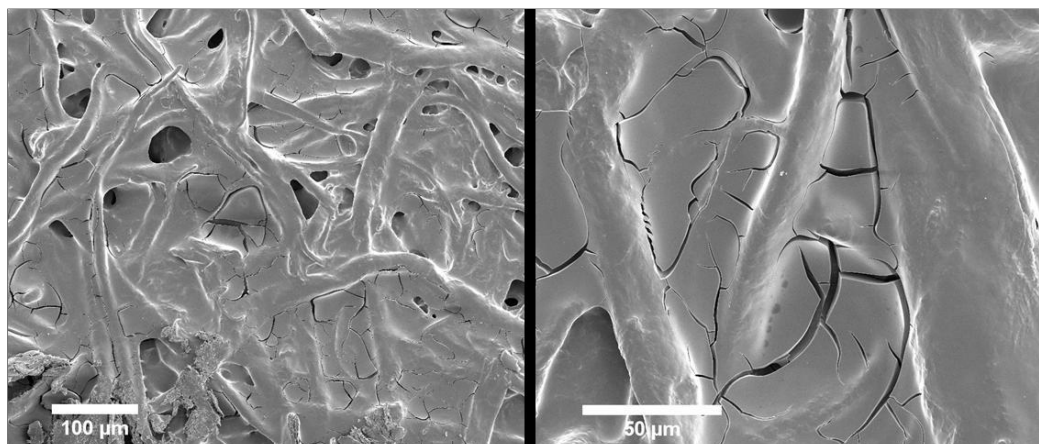


Figure 4.5 SEM images of 85/15 Pluronic® F127/PTSA template coated on cellulose filter paper after tetraethyl orthosilicate infusion.

To decouple these two factors, TEOS was injected externally along with $CO_2$. This time, PTSA concentration was varied between 1, 10 and 20 wt% of the template. The weight of the casted piece of cellulose filter paper was less than 20 mg, with ~50 wt% from Pluronic® F127/PTSA template. Reactor was sealed with sample inside and TEOS was injected externally, along with $CO_2$. SEM characterization of the surface after infusion of

TEOS (before calcination) showed thick skin layer in samples with 20 wt% PTSA (Figure 4.6a) and 10 wt% of PTSA (Figure 4.6b) in initial Pluronic® F127 template, suggesting that skin layer forms during the infusion process and not during pre-heating of the reactor to 60 °C when TEOS is placed inside. Samples with 10 wt% PTSA showed regions with well-ordered cylindrical pores (Figure 4.7c), worm-like pores (Figure 4.7b) and disordered pores. Sample with low PTSA loading did not possess thick skin layer and had a texture similar to that of the template before any TEOS infusion (Figure 4.6c); but samples made with low concentration PTSA lack ordered mesoporoisty (Figure 4.7a).
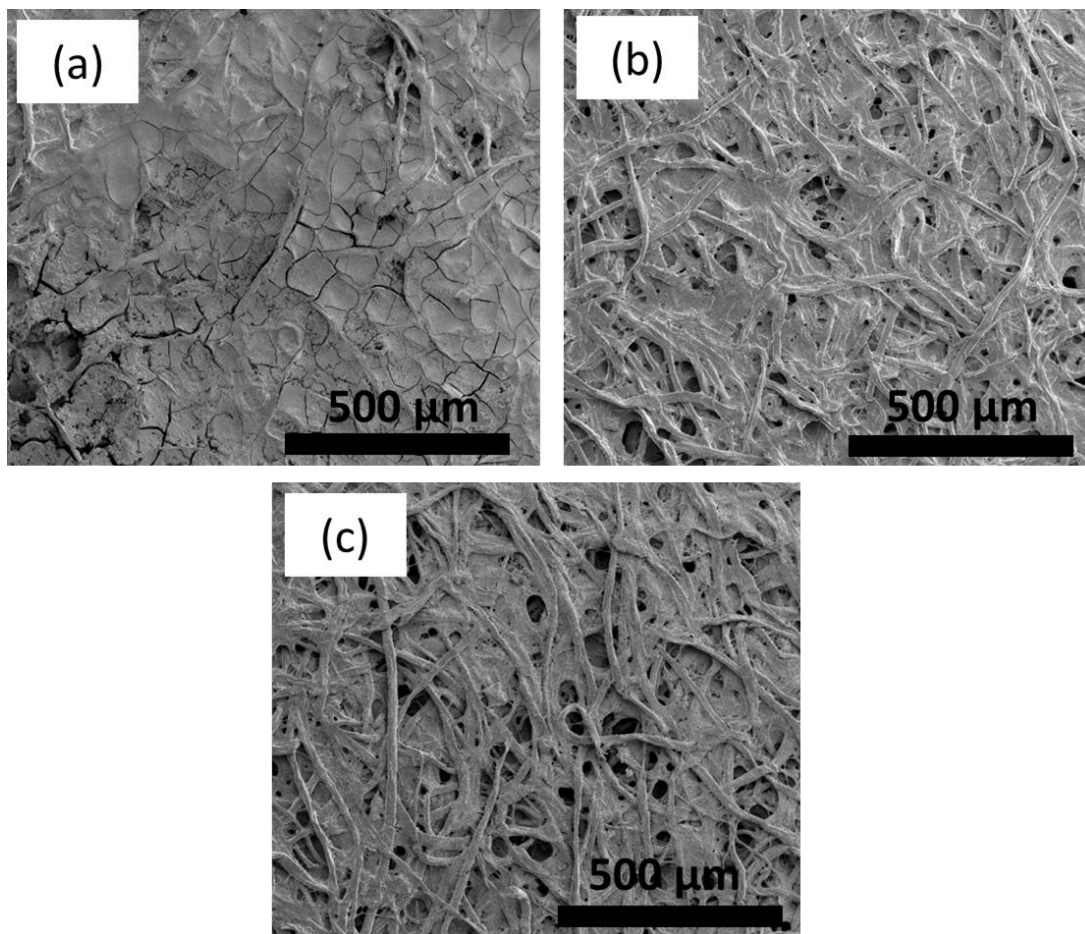


Figure 4.6 (a-b) Pluronic® F127 templates containing 20 wt% PTSA and (b) 10 wt% PTSA after infusion of TEOS injected in the reactor, (c) Template containing 10 wt% PTSA before infusion.
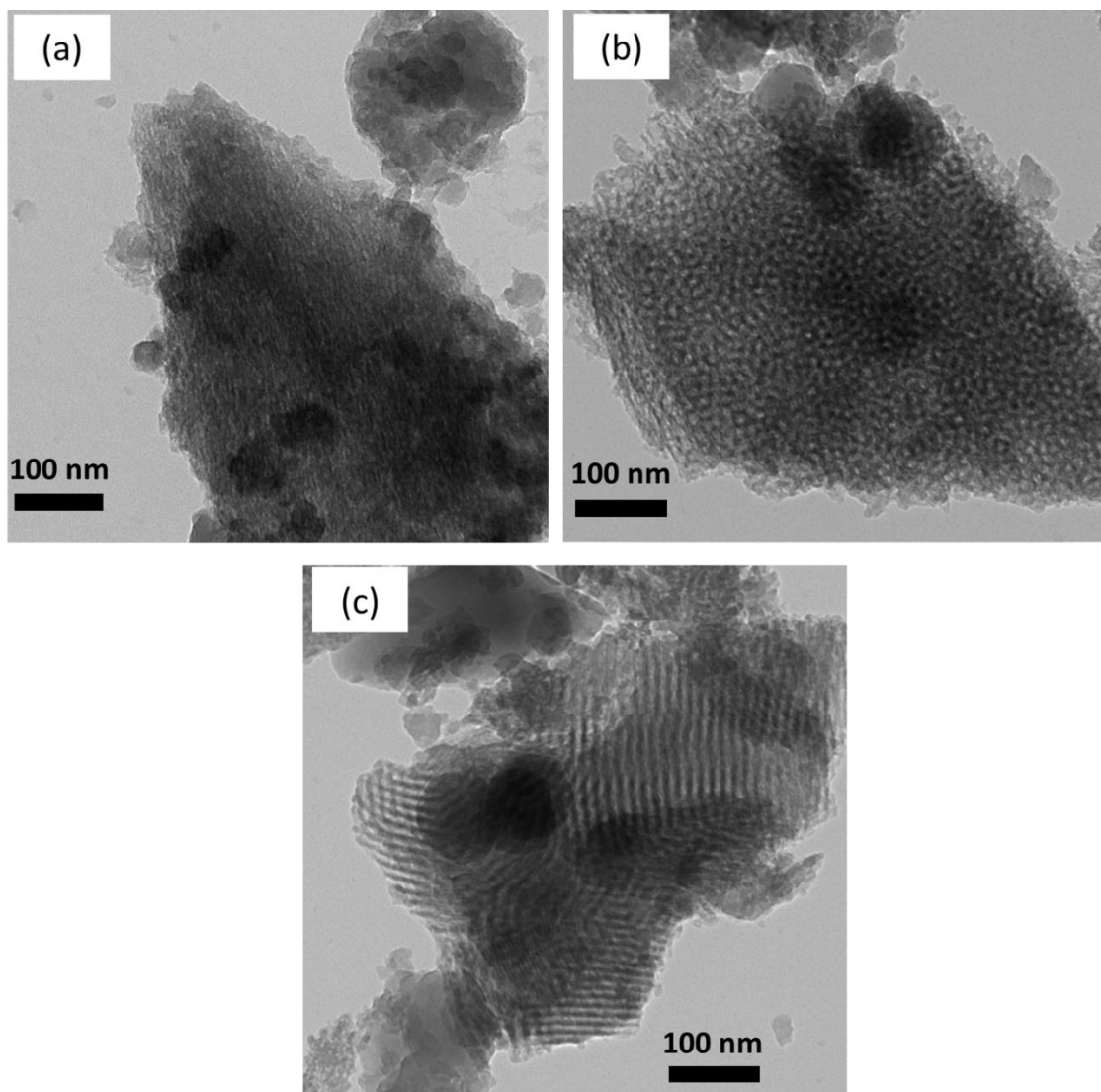
Figure 4.7 Mesoporous silica prepared using (a) 1 wt% PTSA, (b) and (c) 10 wt% PTSA in Pluronic® F127 template. TEOS was injected with $CO_2$ after equilibrating reactor at 60 °C.

It is noted that Pluronic® F127 with 10 wt% of PTSA blend itself did not possess an ordered morphology as observed in SAXS (even after thermal annealing at 85 °C for 24 hours). Ordered morphology appeared only after infusion of TEOS. Infused TEOS rapidly hydrolyze to form silicic acid, which can order the Pluronic® F127 by hydrogen bonding

interaction, before condensing to form a silica network.[169] Since the hydrolysis rate of TEOS to silicic acid is slower in 1 wt% PTSA templates, condensation to silica network may occur much before the ordering in Pluronic® F127 template is achieved.

At this point, it was concluded that in order to make well-ordered mesoporous silica without dense skin layer of silica on the surface, PTSA concentration was needed to be low and template was required to be ordered before the infusion process in carried out.

To enhance long range order of the template, BHCA was blended into Pluronic® F127. The small molecule additive can hydrogen–bond with PEO chains to increase effective $\chi$ of the blend and induce microphase separation, as elaborated in Chapter 2 of this dissertation. This pre-organization of the template will help in reducing the concentration of PTSA and avoid pre-mature condensation of TEOS to form pore-less skin layer on the surface, which otherwise will adversely affect the specific surface area of the fabricated mesoporous silica. Also at this point, 3D pieces of packaging sponge were used as macroporous supports. Figure 4.8a shows a cubical object (~1 cm in height) of mesoporous silica with macroporous architecture, replicated form macroporous sponge.
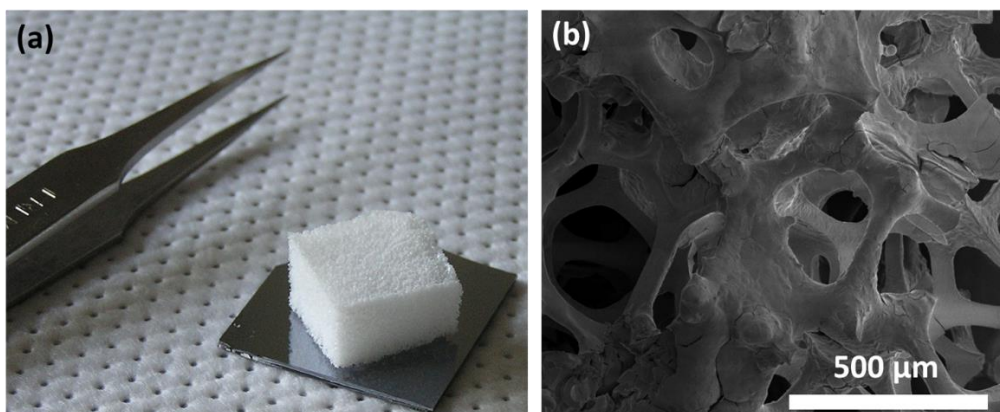


Figure 4.8 (a) digital photograph of a cubical shaped hierarchically porous silica created using Pluronic® F127/BHCA template supported on a macroporous packaging sponge template. (b) SEM image of hierarchically porous silica showing macroporous structure template form packaging sponge.

A 10/90 BHCA/F127 (wt/wt) blend with 1 wt% PTSA catalyst was casted on a 3D piece of packaging sponge, dried at room temperature for 4 h and annealed at 80 °C for 12 h to obtain an ordered morphology. The template was then placed in reactor with excess of TEOS and water in Vespel® containers. The reactor was sealed and heated to 60 °C. There after $CO_2$ was slowly injected (2-3 ml/min) to 1800 psi. A soak time of 2 h was observed and then reactor was depressurized. Samples were calcined to degrade organic template. Initially, order in mesoporous silica obtained by this templating method, as assessed by TEM images, was better than that of the previous method. But, the mesoporous structure failed to showcase long range order in SAXS experiments (no higher order peaks were observed). Later on it was found that a prolonged period of annealing in sealed reactor in the presence of water (before $CO_2$ injection) was necessary to obtain long-range order in mesoporous silica. Figure 4.9(a) shows SAXS and Figure 4.9(b) shows TEM of long-range ordered mesoporous silica created by 10/90 BHCA/F127 with 1% PTSA template casted on sponge and annealed at 80 °C for 12 h. This template was left for a prolonged period in the reactor at 60 °C before injection of $CO_2$ (in the presences of water and TEOS). Figure 4.9(c) shows the nitrogen adsorption/desorption isotherms of the mesoporous silica created by this template. The sudden step in the adsorption and broad hysteresis are characteristic of well-ordered porosity with monodispersed pore-sizes. BET specific surface area was found to be 254 m$^2$/g.

Keeping the template in humid environment allows it to uptake water and soften. As the template softens, TEOS is effectively infused inside it, uniformly condensing in the PEO phase. Moisture absorbed in the Pluronic® matrix also enhances uniform hydrolysis

in the bulk of the matrix. If the template is rigid (as in case of microphase separated block copolymer) and do not absorb moisture effectively in its bulk, silica will quickly condense on exterior surface, thereby hampering TEOS infusion inside the bulk and leading to non-uniform condensation and poorly ordered mesoporous structure.

In contrast to well-ordered silica created by allowing template with low PTSA content to absorb moisture, pre-organized template with the same composition (10/90 BHCA/Pluronic® F127) having higher loading of PTSA (5 %) to enhance order in silica, when not left in the reactor to absorb moisture for elongated period, resulted in mesoporous silica with adsorption isotherm showing no distinct step (indicating poor order), as seen in Figure 4.10. Template with 5 wt% PTSA also showed low BET surface area (141 m$^2$/g) due to pore-less skin layer on top. This clearly suggest that high-quality mesoporous silica can be created by allowing pre-organized templates to absorb water and choosing a low acid catalyst concentration.
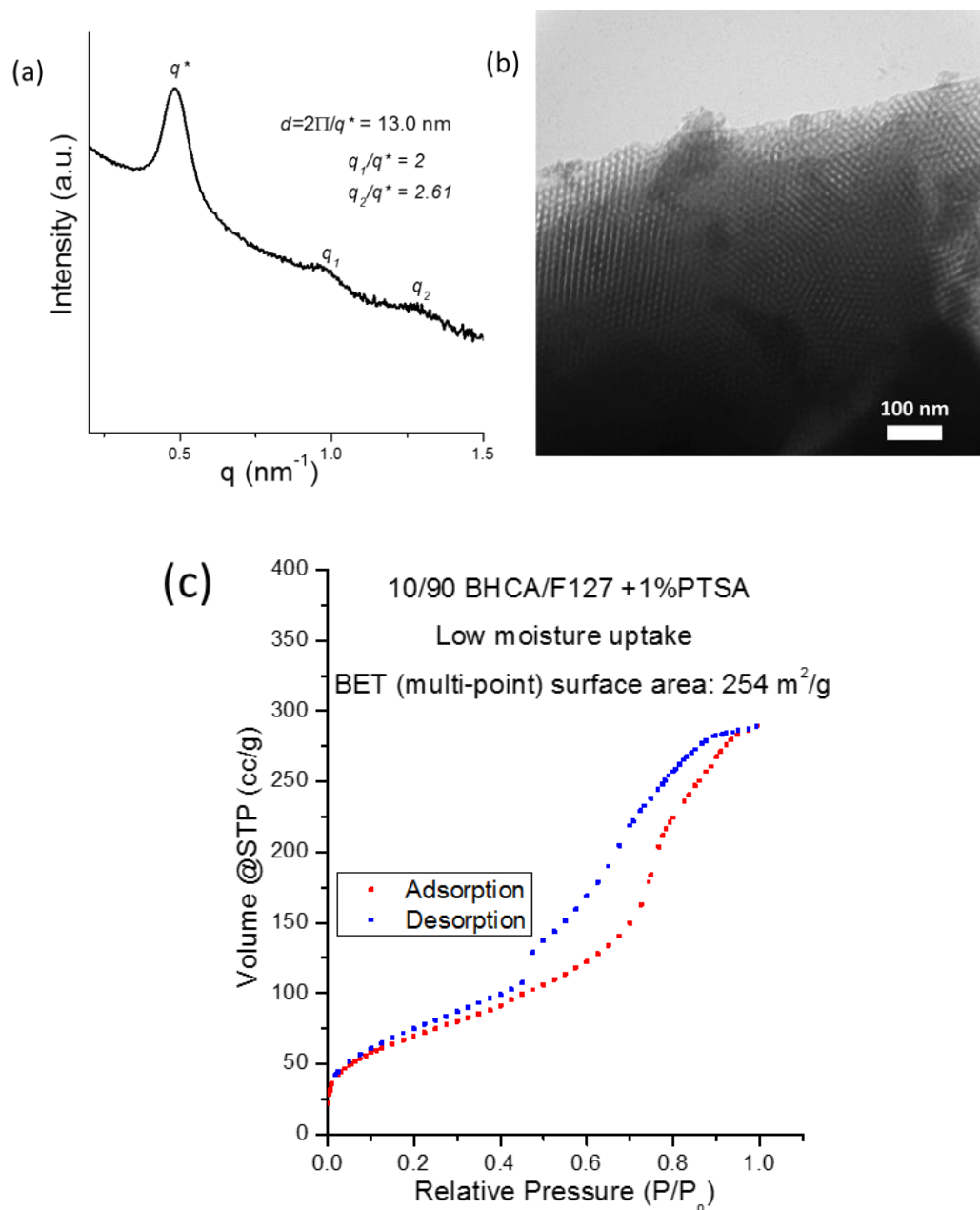
Figure 4.9 (a) SAXS showing long-range order and (b) TEM showing ordered mesoporous structure and (c) nitrogen adsorption/desorption isotherm with BET surface area of mesoporous silica created using 10/90 BHCA/Pluronic® F217 with 1 wt% PTSA. Template was pre-organized by annealing at 80 °C for 12 h and was left in humid reactor for a prolonged period before $CO_2$ injection to infuse TEOS (present in excess amount in reactor).
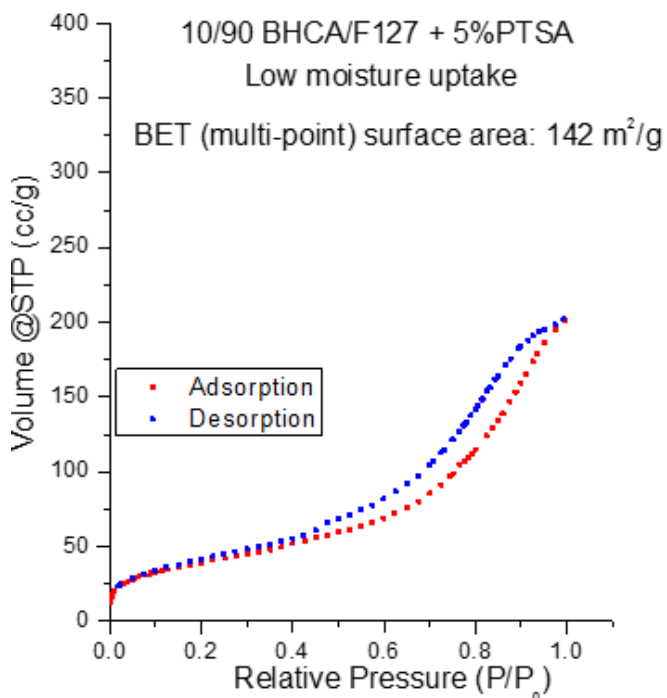
Figure 4.10 Nitrogen adsorption/desorption isotherm with BET surface area of mesoporous silica created using 10/90 BHCA/Pluronic® F217 with 5 wt% PTSA. Template was pre-organized by annealing at 80 °C for 12 h. As soon as reactor was equilibrated to 60 °C, $CO_2$ was injected to infuse TEOS (present in excess amount in reactor).

Driven by these observations, a systematic study was carried to understand the dependence of the extent of silica condensation (per gram of block copolymer template-material) on: first, time period for which the template is left in humid environment before TEOS infusion. Second, amount of TEOS in the reactor. Third, rigidity of the initial polymer template.

Figure 4.11 provides SAXS data of the mesoporous silica created by a 20/80 BHCA/Pluronic® F127 template with 1 wt% PTSA catalyst. Equal masses of packaging-sponge were cut and soaked in 2 wt% solution of BHCA/Pluronic® F127/PTSA and dried in air for 24 h to have a 32 mg of BHCA/Pluronic® F127/PTSA coated on them. The concentration of solutions was kept low (2 wt% instead of 10 wt%) to have a thin coating,

where TEOS can uniformly get infused. Annealed (85 °C; 24 h) and 'not-annealed' samples were placed simultaneously in the reactor along with TEOS and excess of water. The reactor was then sealed and heated to 60 °C for a certain period for template to uptake moisture. Three batches were carried out. TEOS amount was varied from 250 µl to 500 µl to 500 µl and time to uptake moisture was varied from 2 h to 2 h to 8 h between the batches. Reactor was then pressurized rapidly (in less than 5 min) to 1800 psi. 2 h soak time was observed, after which reactor was depressurized and samples were weighed for mass uptake. Samples were calciend and SAXS was performed.

Form Figure 4.11 it can be see that well-ordered mesoporous structure can be produced in all pre-organized (annealed) templates. Samples fabricated form template that were not pre-organized also showed impressive ordering in final silicate structure, because of the ordering caused by rapid formation of silicic acid in moisture rich plasticized-templates. The amount of silica condensed per gram of template (mentioned in Figure 4.11 alongside the graphs) was significantly higher in case of not-annealed templates compared to annealed templates. This important observation can be explained by the rigidity of the matrix. Since the microphase separated morphologies are more rigid than phase-mixed (as discussed in Chapter 2 of this dissertation), the rate of TEOS infusion inside them is slower and hence condensation of silicate is less. By comparing mass uptake between the batches with different amount of TEOS, but exposed to humid environment for the same time period before $CO_2$ injection (Figure 4.11a and b), it can be seen that weight gain in 500 µl
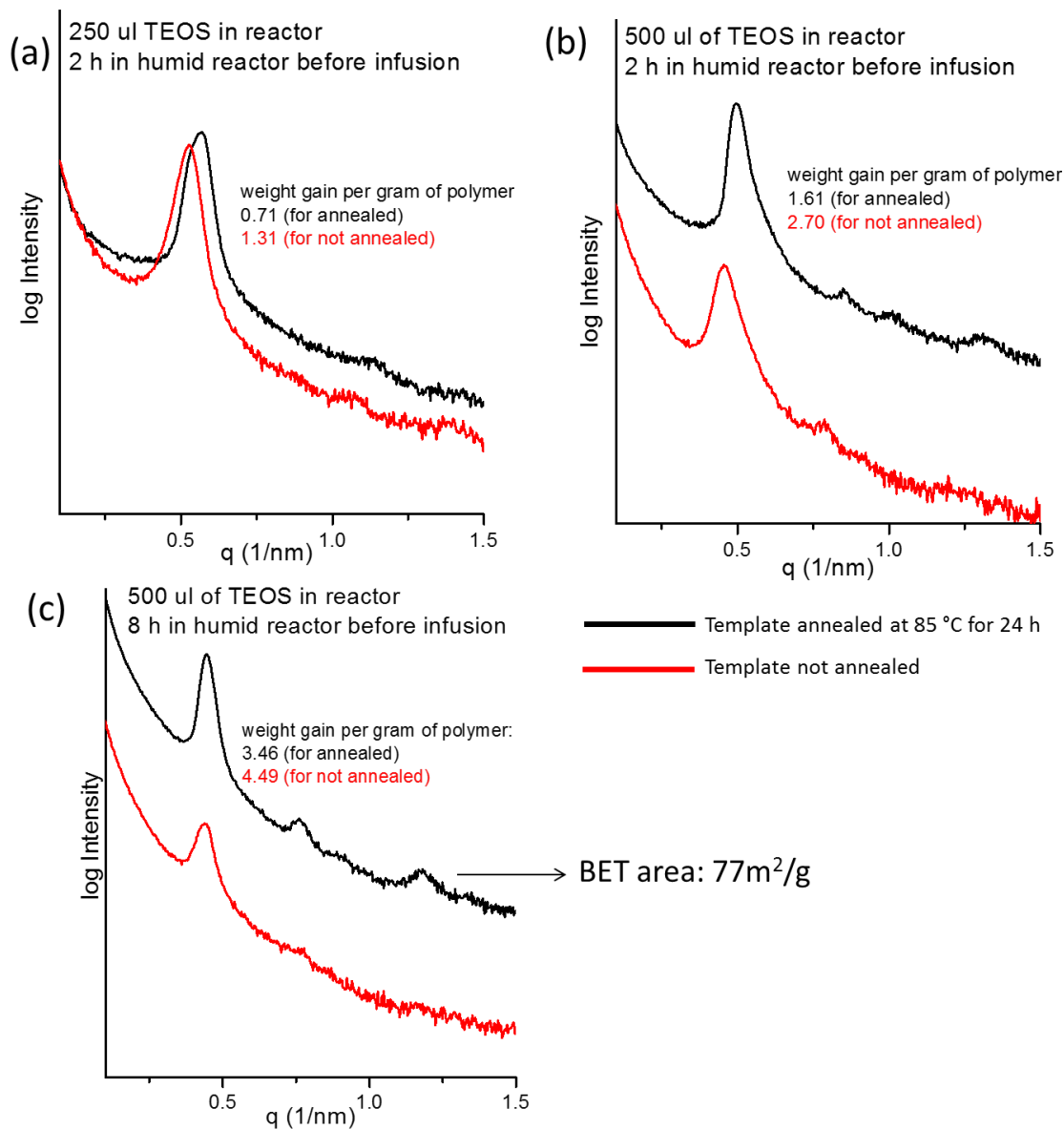
Figure 4.11 (a-c) SAXS of various mesoporous silica samples created using a 32 mg of 20/80 BHCA/Pluronic® F127 template doped with 1% PTSA supported on macroporous sponge.

TEOS batch was more than twice the weight gain in 250 μl TEOS batch. Samples soaked for 8 h in humid closed reactor gained weight 1.5-2 times that of the samples soaked for 2 h for the same amount of TEOS in the reactor. BET surface area (obtained through nitrogen adsorption/desorption isotherm) of sample from template kept for 8 h in humid reactor

along with 500 µl TEOS was 77 m$^2$/g. Although the mesoporous silicate structure is well-ordered (sharp and narrow primary peak and multiple secondary peak in SAXS) it has low surface area because of excessive condensation of silicate within the template and on the surface as pore-less skin layer. Considering density of silica ~2.2 g/cc and of template ~1 g/cc, any degree of condensation leading to more than 1.5 times of template weight will result in approximately 70 % volume increase in template after infusion. None of the samples showed a 70% increase in d-spacing of cylindrical morphology after the infusion step. Note that the above approximation is lenient, as the density of infused silica which is not completely in condensed from will still be lower, and will occupy more volume. Therefore it can be deduced that pore-less silica is present in the final material when 500 µl TEOS in present reactor. The amount of TEOS was therefore kept well below 500 µl for further experiments when using preheating time of more than an hour in humidified closed reactor.

The thickness of 20/80 BHCA/F127 (1% PTSA) template-coating on macroporous supports were further reduced by using 1 wt% solution. Templates were annealed at 85 °C for 24 h in vacuum oven. The time for which templates were kept in humid closed reactor was fixed as 3 h and reactor was pressurized with $CO_2$ at a very fast rate (pressure was increased to 1800 psi in 2 minutes). A soak time of 1 h was observed before depressurizing the reactor. Faster $CO_2$ injection shall provide uniform condensation of silicate in the template matrix, as opposed to slower injection which will gradually build up TEOS concentration in gas phase and lead to condensation at outer surface at first, which may lead to pore-less silica. Thinner films further promote uniform condensation throughout the template. Lower concentration of TEOS in reactor were investigated so as to have less

degree of condensation of silicate. Figure 4.12 shows SAXS at the various steps of mesoporous silica fabrication process created using the above mentioned conditions with 125 µl of TEOS in the reactor and 12 mg weight of coated template on macroporous support. Mass gain was 17 mg after infusion step, 1.41 times the mass of the template. It can be seen that highly ordered cylindrical morphology is present in the initial template as well as in the calcined mesoporous silica structure. Domain spacing increase from 13.9 nm to 19.2 nm after infusion, suggesting a 38% volume increase after infusion. Figure 4.13(b) shows nitrogen adsorption/desorption isotherms with BET surface area of 233 $m^2$/g, which also included microporous area of 15 $m^2$/g. Mesoporous silica thin films created using $scCO_2$ infusion technique in past is known to have microporous area, which is attributed to porosity created by removal of PEO chains.[170] A total pore volume of 0.31 cc/g was obtained from isotherm. The adsorption isotherm has a sudden step, indicating narrow spore-size distribution. BJH pore size distribution calculated using adsorption isotherm (Figure 4.14) showed monodispersed porosity with 7 nm pore diameter. Figure 4.13a and Figure 4.13c shows nitrogen adsorption/desorption isotherms of mesoporous silica created using same conditions but 25 µl and 250 µl of TEOS respectively. The total surface area of sample created using 25 µl TEOS is 340 $m^2$/g (108 $m^2$/g microporous, 215 $m^2$/g external) and that with 250 µl TEOS is 236 $m^2$/g. High microporous surface area in sample created using 25 µl TEOS is suggestive of low-density crosslinking in PEO phase. In all the three cases, external surface area (area of mesopores) is ~ 200 $m^2$/g.
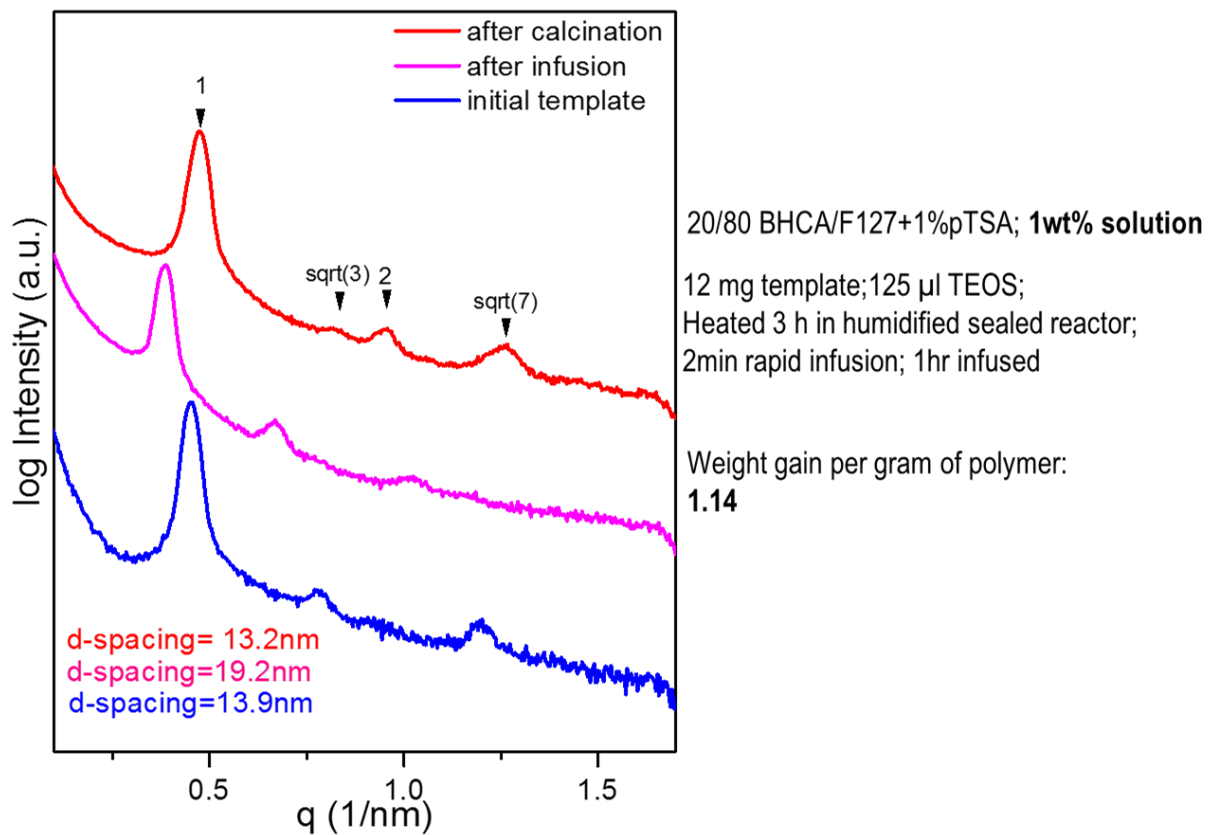
Figure 4.12 SAXS at various steps of mesoporous silica formation using 20/80 BHCA/Pluronic® F127 with 1 wt% PTSA coated on macropoorus sponge as template.

**(a)** 25 µl TEOS — Relative Pressure (P/P$_o$) vs Volume@ STP (cc/g), Adsorption / Desorption

**(b)** 125 µl TEOS — Relative Pressure (P/P$_o$) vs Volume@ STP (cc/g), Adsorption / Desorption

**(c)** 250 µl TEOS — Relative Pressure (P/P$_o$) vs Volume@ STP (cc/g), Adsorption / Desorption

| TEOS | Total surface Area (Micropore+ Mesopore) | Total pore volume |
|------|------------------------------------------|-------------------|
| 25µl | 340m$^2$/g (108+215) | 0.315 cc/g |
| 125µl | 233m$^2$/g (15+207) | 0.309 cc/g |
| 250µl | 236m$^2$/g (37+199) | 0.303 cc/g |
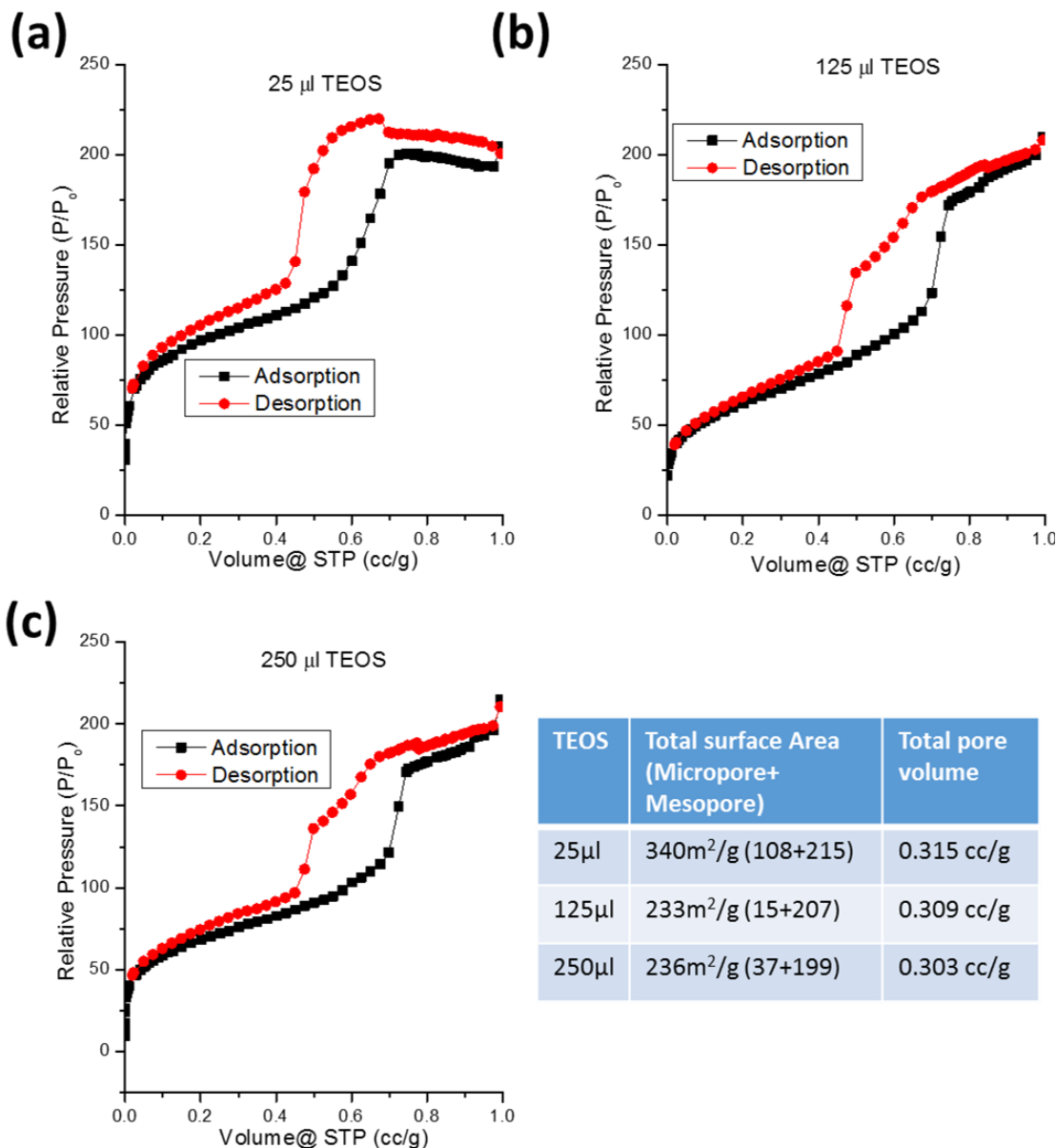
Figure 4.13 Nitrogen adsorption/desorption isotherms of mesoporous silica created using 20/80 BHCA/Pluronic® F127 with 1 wt% PTSA coated on macropoorus sponge as template. Amount of TEOS in the reactor was (a) 25 µl (b) 125 µl and (c) 250 µl. Steep steap in adsorption isotherm and wide hysteresis indicates well-ordered pores with narrow pore-size distribution. Total surface area and pore volume in each case are mentioned in the table.
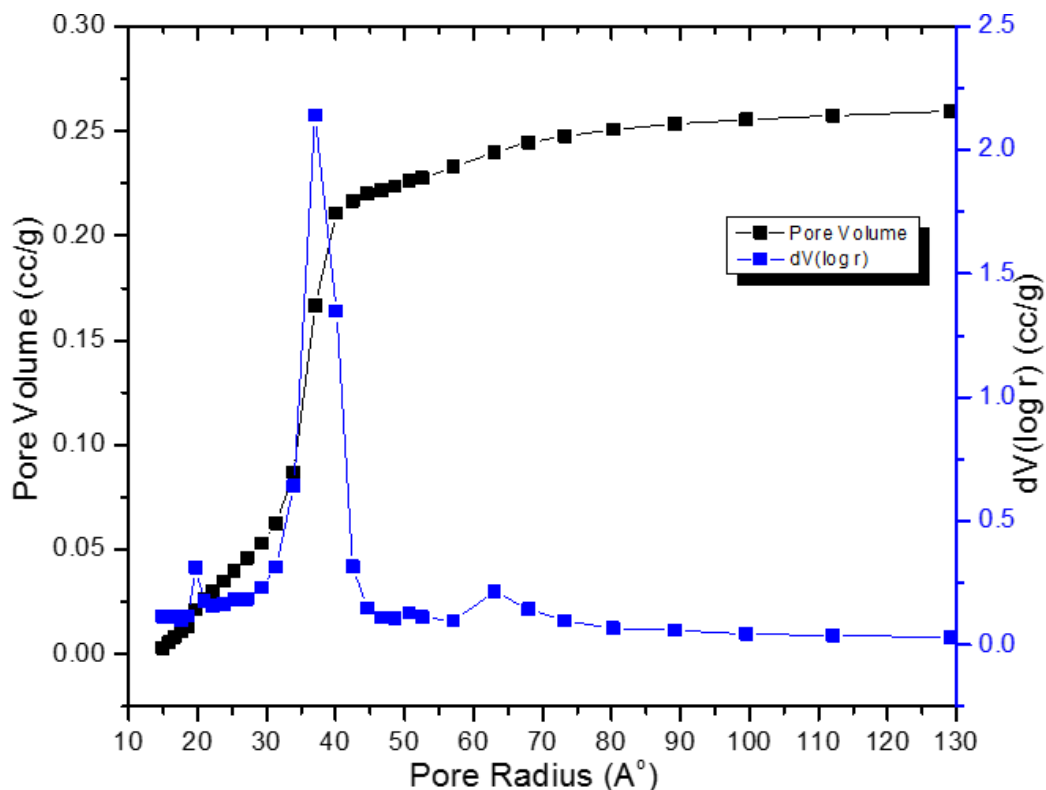
Figure 4.14 BJH pore size distribution obtained from adsorption isotherm in Figure 4.13b (125 µl TEOS batch) with monodispersed pores around 7 nm in diameter.

## 4.4 Conclusion

Hierarchically porous silica with mesopores interconnected by macropores was successfully fabricated using pre-organized Pluronic® /small-molecule-additive/PTSA templates coated on macroporous supports. It was found that for a given thickness of mesopore-template on macroporous support, concentration of acid catalyst (PTSA) in the template, rigidity of the template, amount of TEOS placed in the reactor, and time for which template was kept in the humidified reactor before $CO_2$ injection greatly affected the final mesopore order and specific surface area. Long-rage ordered mesoporous silica with monodispersed pores of 7 nm diameter and ~200 $m^2$/g surface area was successfully fabricated by systematically tuning these parameters.

## 4.5  Acknowledgements

CHAPTER 5

DIRECT AND RAPID SOFT-IMPRINTING OF DIMENSIONALLY

STABLE INORGANIC OXIDE 1D, 2D AND 3D NANOPATTERNS

USING INKS CONTAINING CRYSTALLINE NANOPARTICLES

## 5.1   Introduction and Objectives

Patterned metal oxide and semiconductor films are ubiquitous in functional device architectures. Typical fabrication pathways are subtractive by nature and contain multiple steps, including deposition of a planar film by chemical or physical deposition methods such sputtering or chemical vapor deposition, application of a photoresist, patterning of the resist using optical lithography, development of the resist, etching the metal oxide and stripping of the residual resist. The fabrication sequence is usually carried out in a clean room facility and employs batch processes, some of which operate at elevated temperatures and reduced pressures. Consequently, patterned inorganic film fabrication is often cost, equipment, materials and energy intensive and is not amendable to continuous as opposed to batch fabrication.

The development of additive or direct patterning techniques for metal oxide and semiconductor films, particularly using approaches that are scalable for continuous production and operate at ambient pressure and modest temperatures would be enabling for the low cost production of fully functional printed electronics or for devices that require large active areas. Among the most significant challenges are fabrication rate and integration density. Many printing approaches yield structures with minimum features

103

sizes of tens or hundreds of microns, while acceptable performance thresholds often require features in the deep sub-micron range. For example, features below 250 nm are required for the manipulation of visible light while features below 1 micron are required to approach electronic device integration densities achieved by the semiconductor industry in the 1980s.

Advances towards direct writing and other approaches to directly patterned inorganic device layers have been realized over the past decade. Lewis and co-workers introduced Direct Ink Writing (DIW) a serial writing approach to produce patterned structures via coagulation of polyelectrolyte,[171] colloidal[172] or sol-gel precursor inks[173] printed via extrusion through micron scale nozzles. For example amorphous metal oxide structures could be produced sol-gel inks in arbitrary planar and 3D structures with lateral dimensions on the order of 2 and 4 microns for 1D and 3D structures, respectively. For $TiO_2$ fabrication, calcination of the printed inks to yield anatase resulted in 80% volume shrinkage and minimum feature sizes on the order of 0.25 and 0.5 microns for the 1D and 3D structures.[173] Micron scale inorganic structures can also be produced by first creating a sacrificial organic template structure by DIW using polyelectrolyte inks followed by coating the structure using CVD or another deposition method and removing the template by calcination. Such an approach has been used for the fabrication of silicon woodpile structures, for example.[174] While an effective additive approach, challenges for DIW include rate limitations due to serial writing and direct printing of deep sub-micron features without relying on volumetric shrinkage of precursor structures.

Nanoimprint (NIL) and soft lithography offer the potential for large area, rapid and scalable patterned film fabrication. Thermal imprint lithography (embossing) and UV-

assisted NIL (light-induced polymerization of a liquid resin in contact with a master) have been scaled for roll-to-roll production and can produce patterned polymer film as dimensions as small as 50 nm at feet-per-minute rates.[175] NIL in combination with thermal/UV induced polymerization of oligomers containing Si, Ti or Zr atoms in order to improve refractive index has been used to imprint optical waveguides and 2D photonic structures).[176,177] Recently, UV-NIL has been employed for the patterning of optical gratings[178] and 3-D photonic crystals[179] using hybrid polymer/nanoparticle resists system of tunable refractive index and nanoparticle loadings of up to 90 wt%.

Direct NIL of complete inorganic crystalline metal oxide films, for example $TiO_2$, ZnO, $BaTiO_3$ and indium tin oxide (ITO) is typically pursued by thermal- or UV-based soft-imprinting of sol-gel precursors, followed by calcination to remove organics and condense the crystalline oxide phase.[180-182] Transition from sol to amorphous gel phase in the soft mold features lead to a height reduction of imprinted features by 40-60%.[182,183] High temperature calcination to obtain crystalline phase from amorphous gels is accompanied with large shrinkage (60-80%) that causes dimensional instability and cracking.[180,181]

Soft imprint lithography can be practiced using a solvent permeable stamps to remove solvent from a resist system, leaving behind solids. Such an approach has been used to pattern lines of metal nanoparticles, including gold (Figure 5.1) that could be subsequently annealed to produce conducting features.[184,185] However, elevated temperatures required post-imprinting to remove high volume of organic ligand covalently attached to the gold nanoparticle leads to excessive shrinkage and feature distortion (18 wt% ligand coverage[184] will lead to 80% volumetric shrinkage considering gold density

approximately 19 times of the organics). These direct imprinting approaches have not been widely applied for the preparation of patterned metal oxide films using metal oxide nanoparticle dispersions.
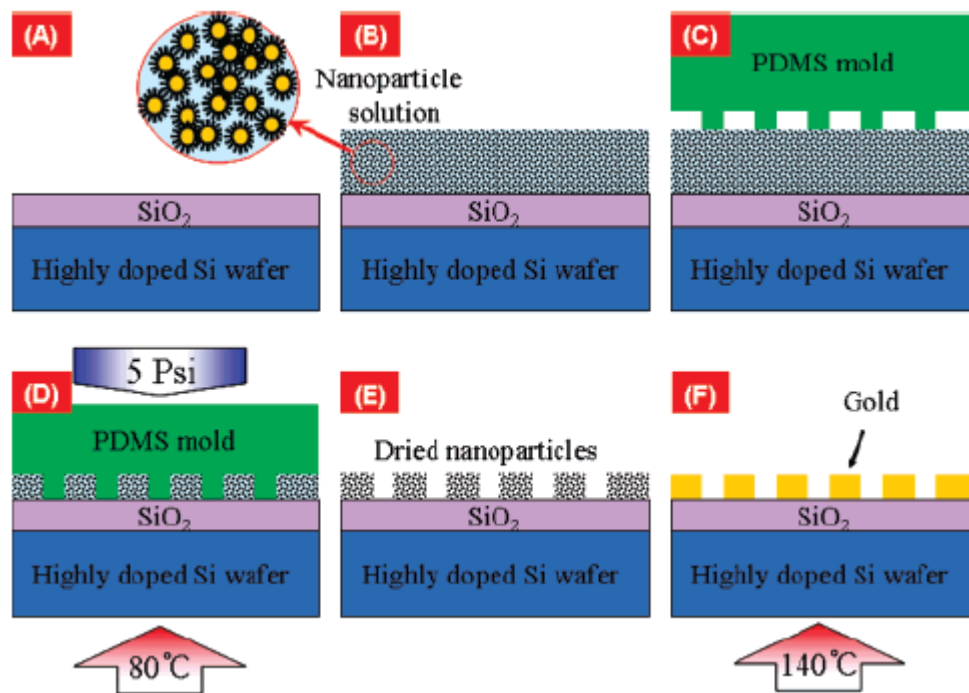


Figure 5.1 Solvent-assisted imprinting of gold nanoparticles using soft PDMS stamp. (A, B) Nanoparticle suspension is dispensed on a silicon substrate. (C, D) PDMS is pressed, solvent permeates through PDMS. (E) Stamp is removed to obtain imprinted nanoparticle lines. (F) Substrate heated to melt nanoparticles to make gold lines. And remove organic ligands.

**Objectives of this research.** Objective of this research is to utilize solvent-assisted soft imprint lithography technique for the direct fabrication on inorganic oxides nanostructures. 1D, 2D and 3D nanopatterns will be fabricated in completely solution processable manner. High-aspect ratio nanostructures and residual layer free nanostructures will be fabricated using soft stamps. The soft imprinting technique will be

optimized to fabricated nanostructures in a rapid fashion. A print-planarize-print strategy will be developed to fabricate 3D inorganic oxide nanostructures.

## 5.2 Experimental

### 5.2.1 Materials

Nanoparticle dispersions: Indium tin oxide (ITO, 30 wt%, 20-30 nm average particle size, $In_2O_3$: $SnO_2$ = 90:10 (wt%) ) nanoparticles dispersion in isopropanol (Nanostructured & Amorphous Materials, Inc.), titanium oxide (anatase, 15 wt%, 5-30 nm average particle size) nanoparticles dispersion in water (Nanostructured & Amorphous Materials, Inc.), titanium oxide (anatase, 20 wt%, 15 nm average particle size) nanoparticles dispersion in 1, 2-propanediol (US Research Nanomaterials, Inc.). Metal Salt Peecursors: Indium(III) nitrate hydrate ($In(NO_3)_3.xH_2O$ 99.99%, Sigma-Aldrich Co., Ltd., USA), tin (IV) acetate ($Sn(CH_3CO_2)_4$, Sigma-Aldrich Co., Ltd., USA), titanium diisopropoxide bis(acetylacetonate) ($(CH3)_2CHO]_2Ti(C5H_7O_2)_2$, 75 wt% in isopropanol, Sigma-Aldrich Co., Ltd., USA). Solvents: N-methyl-2-pyrrolidone (99%, Sigma-Aldrich Co., Ltd., USA), methanol (ACS grade, Fisher Scientific), propylene glycol monomethyl ether acetate (PGMEA, ReagentPlus® 99.5%, Sigma-Aldrich Co., Ltd., USA). For PDMS: (7.0-8.0% vinylmethylsiloxane)–dimethylsiloxane copolymer, trimethylsiloxyl terminated (VDT-731, Gelst), 2, 4, 6, 8-tetramethyltetravinylcyclotetrasuloxane (Fluka-87927, Sigma-Aldrich Co., Ltd., USA), platinum-divinyltetramethyldisiloxane complex in xylene (SIP-6831, Gelest), (25-30% methylhydrosiloxane)-dimethylsiloxane, hydride terminated (Gelest), sylgard 184 silicone elastomer kit (Ellsworth Adhesive). Miscellaneous: norland optical adhesive 60 (NOA60, Norland Products, Inc.), (heptadecafluoro-1,1,2,2-

tetrahydrodecyl)dimethylchlorosilane (Gelest), silicon wafers of (100) orientation (p-type, boron dopant) were purchased from NovaElectronics., quartz microscope slides (Chemglass Life Sciences).

### 5.2.2  PDMS Stamps Fabrication

Patterned PDMS stamp replicas were made by casting PDMS against patterned hard silicon master molds. A self-assembled monolayer (SAM) of fluorine containing molecule is created on silicon masters to reduce their surface energy before replicating PDMS stamps. The silicon maters were cleaned by dipped overnight in concentrated sulfuric acid and flushing with water, followed by treating for 15 minutes in an oxygen plasma cleaner. Cleaned silicon master molds were then placed in a degassed glass jar at 80 °C, to which 1 vol% of heptadecafluoro-1,1,2,2-tetrahydrodecyl)dimethylchlorosilane (Gelest Corp.) is introduced. A 12 h period is observed, during which heptadecafluoro-1,1,2,2-tetrahydrodecyl)dimethylchlorosilane vaporizes and forms a SAM on the silicon master molds.

Sylgard 184 silicone elastomer kit (Ellsworth Adhesive) was used to make PDMS stamps from silicon master with low aspect-ratio line pattern (LW, ~425 nm; LP, ~950 nm; LH, ~480 nm). A 10:1 (by weight) ratio of base to curing agent was thoroughly mixed and about 3 mm thick layer was poured on the hard master molds kept in a polystyrene Petri-dish. Vacuum was pulled (for 5-10 minutes) to remove air inclusions and dissolved gases. PDMS was then cured at 70 °C for 5 h, cut using razor blade and peeled away from the master mold to obtain in patterned stamp form.

Bilayer composite PDMS was used to make stamps from hard silicon master molds bearing high aspect-ratio and densely packed features in line pattern form and square hole-array form. The bilayer stamp consists of a patterned thin layer of hard-PDMS (h-PDMS) backed with a thick soft Sylgard 184 PDMS layer, and were made using a method described elsewhere[186]. A hard-PDMS layer is essential as Sylgard 184 PDMS having insufficient mechanical strength will cause high aspect ratio densely packed features on the stamp to deform and collapse. In a typical process to make h-PDMS, 1.7 g of (7.0-8.0% vinylmethylsiloxane)–dimethylsiloxane copolymer(trimethylsiloxyl terminated, VDT-731, Gelest Corp.) was mixed with one drop of 2, 4, 6, 8-tetramethyltetravinylcyclotetrasuloxane (Fluka-87927, Sigma-Aldrich Co. Ltd.) and 9 µl of platinum-divinyltetramethyldisiloxane complex in xylene (SIP-6831, Gelest). The mixing was done in a 25 ml glass vial for 30 s using a magnetic stirrer. The mixture was then immediately degassed on a Schlenk line by pulling vacuum for 1 min. To the degassed mixture, 0.5 ml of (25-30% methylhydrosiloxane)-dimethylsiloxane (hydride terminated, Gelest Corp.) was drop wise added and stirred for 1 min. At this point the h-PDMS mixture was ready and was immediate spin-coated on patterned silicon master at 1000 RPM for 40 s, followed by heating master on a hot plate at 60 °C for 2 min to cure h-PDMS. Approximately 3 mm thick layer of Sylgard 184 prepolymer mixture (made as described above) was poured on to the still tacky h-PDMS layer and cured at 70 °C for 5 h. The cured bilayer composite PDMS was then cut using a razor blade and peeled away from the master mold to obtain in patterned stamp form.

### 5.2.3 Preparation of NP dispersions for inks.

Solvent exchanged ITO NPs dispersion in NMP is obtained by adding low vapor pressure high boiling point NMP solvent to commercially available ITO dispersion in IPA, followed by forceful evaporation of high vapor pressure low boiling point IPA. Equal weights of ITO (around 30 wt%, 20-30 nm average particle size, $In_2O_3$: $SnO_2$ = 90:10 (wt%) ) NPs dispersion in IPA (Nanostructured & Amorphous Materials, Inc.) and NMP (N-methyl-2-pyrrolidone 99%, Sigma-Aldrich Co. Ltd.) are mixed and dried under a stream of air to reduce the weight of the mixture to half of its original value. The solid content of ITO in the dispersion obtained after solvent exchange, as determined by calcining the NP dispersion at 500 °C for 1 h was found to be 25.9 wt%.

To obtain $TiO_2$ NPs dispersion NMP-methanol solvent mixture, titanium oxide (anatase, 15 wt%, 5-30 nm average particle size) NPs dispersion in water (Nanostructured & Amorphous Materials, Inc.) was mixed with NMP and methanol in 2:1:1 weight ratio and dried under a stream of air to remove majority of solvents (up to 50%). The resulting dried slurry was redispersed in equal amounts of NMP and methanol using vortex-mixing and sonication to obtain 15 wt% $TiO_2$ NPs dispersion, which can be further diluted with methanol if desired. Methanol was found to be important to balance proticity and avoid agglomeration upon removal of majority of water.

To obtain ~3 wt% of $TiO_2$ NPs dispersion in propanediol-methanol solvent mixture, one part (by volume) of titanium oxide (anatase, around 20 wt%, 15 nm average particle size) NPs dispersion in 1, 2-propanediol (US Research Nanomaterials, Inc.) was diluted with 5 parts of methanol (ACS grade, Fisher Scientific).

Small batches (few milliliters) of NPs dispersion were ultrasonicated for a few minutes before using as ink.

### 5.2.4   Preparation of NP/Sol inks.

To prepare NP/sol ITO-ink, ITO NPs dispersion in NMP was mixed with ITO sol in NMP. ITO sol in NMP was prepared by dissolving 0.235 g of tin (IV) acetate $(Sn(CH_3CO_2)_4$, Sigma-Aldrich Co. Ltd.) in 6.75 g of NMP at 80 °C, followed by solubilizing 3.02 g of indium(III) nitrate hydrate $(In(NO_3)_3.xH_2O$ (x = 4.5, as determined by weight loss upon heating in vacuum at 105 °C for 24 h), Sigma-Aldrich Co. Ltd.). Note that the dissolution of tin salt is difficult upon dissolving indium salt in NMP at first. This composition of metal salts will create ITO with $In_2O_3$: $SnO_2 = 90:10$ (wt%) upon calcining the sol at 500 °C.  To prepare 80 NP/20 sol $TiO_2$ ink, 15 wt% $TiO_2$ NPs dispersion in NMP-methanol was mixed with titanium diisopropoxide bis(acetylacetonate) (TPA, $[(CH_3)_2CHO]_2Ti(C_5H_7O_2)_2$, 75 wt% in isopropanol, Sigma-Aldrich Co. Ltd.) in proportions to provide 80:20 (by wt) NPs to TPA in the ink.

### 5.2.5   Characterization

Aggregates size distributions in NP dispersions diluted to 5 wt% solids were measured by dynamic light scattering (Malvern Zetasizer 3000 HSa instrument). Transmission electron microscopy was performed in bright field imaging mode using a JEOL 2000 FX TEM operated at an accelerating voltage of 200 kV. Silicon master was gold sputtered using sputter coater (CR 108) for 60 seconds. Scanning electron microscopy

was performed on a field emission scanning electron microscope (Magellan 400). Thickness measurements of planar films were performed with a surface profilometer (Veeco Dektak 150). Sheet resistance of planar ITO films (on $SiO_2$ (300 nm)/Si wafer) were measured using four-point probe technique (Keithley 2400 instrument) with evaporated gold electrodes for contacts. Transmittance measurements of planar films on quartz substrate were performed on UV-Vis spectrophotometer (Perkin Elmer Lambda 1050 UV/VIS/NIR spectrometer) using integrating sphere accessory. X-ray diffraction (XRD) experiments were performed using X-ray diffractometer (Philips PANalytical X'Pert) equipped with copper Kα X-ray (0.1542 nm) source operating at 45 kV and 40 mA. Average crystallite size by XRD was measured using Scherrer equation. Spectroscopic ellipsomety measurements for determination of refractive index (RI) were performed using a variable-angle spectroscopic ellipsometer from J. W. Woollam Co. (RC2-DI). Ellipsometric data was collected for 55°, 60°, 65° and 70° angles of incidence. RI for ITO was determined by fitting ellipsometric data in 450-1500 nm spectral range with a bilayer model consisting of general oscillator layer on silicon substrate. The fitting was performed using instrument's own VASE-software (Complete EASE$^{TM}$, version 2.30 and the general oscillator model used for fitting comes with the software. RI for $TiO_2$ was determined by fitting ellipsometric data in 380-1500 nm spectral range with a bilayer model consisting of a Cauchy layer on Si substrate. Porosity was calculated using Lorentz-Lorenz effective medium approximation model as[191]:

$$\frac{n_{eff}^2 - 1}{n_{eff}^2 + 2} = (1 - f)\frac{n_c^2 - 1}{n_c^2 + 2}$$

where $n_{eff}$ is the measured RI of the film, $f$ is the volume fraction of the pores (percentage porosity= 100x$f$) and $n_c$ is the RI of dense material in the absence of porosity.

## 5.3 Results and Discussion

We have imprinted metal oxide nanostructures using inks that comprise of stable suspensions of crystalline nanoparticles (NPs) in polar organic solvents, and mixtures of crystalline NPs with metal oxide sol-gel precursor. To demonstrate generality of the imprinting strategy, imprinting is demonstrated for two technologically important metal oxides, ITO and TiO$_2$. A solvent permeable PDMS stamp replicated from a hard master mold is used for imprinting. NP inks were obtained by replacing isopropyl alcohol (IPA) or water in commercially available pH-stabilized NP dispersions with low vapor pressure polar organic solvents, for example N-methyl-2-pyrrolidone (NMP) or a NMP-methanol solvent mixture. Covalently bound NP-ligand based dispersions were avoided because they will lead to deformation in features upon subjecting to high temperatures, required to remove strongly attached ligand. Inks were spin coated for a sufficient amount of time so as to evaporate excessive solvent while maintaining enough fluidity in the film to facilitate soft-imprinting. An overview of the solvent assisted imprinting of NPs for patterned metal oxide films is shown in Figure 5.2. After spin-coating ink, PDMS stamp is gently placed on the film. Good air permeability of the PDMS stamp and capillary forces ensures conformal contact without formation of air inclusions at the interface, resulting in uniform filling of the stamp features with the ink. Ink dries as the solvent permeates through PDMS, creating rigidified NP based nanostructures as guided by the stamp features. Nanostructures obtained after removal of stamp are stable as the strong electrostatic

interaction between the NPs after removal of solvent prevents them from collapsing. The thickness of spin coated films greatly depended upon ambient humidity with higher humidity leading to thinner films. Spin speed and extend of dilution can be adjusted in order to tune residual film thickness under imprinted structures.
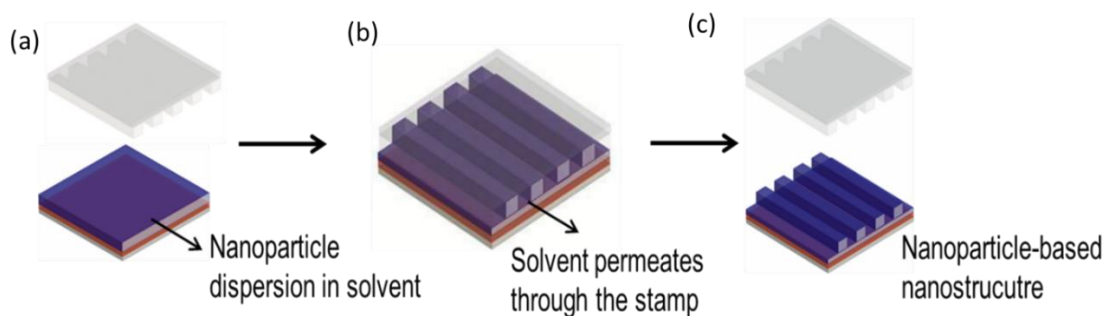


Figure 5.2 Schematics of solvent-assisted NIL for imprinting NP-based nanostructured films: (a) Ink comprising of NP dispersion in an organic solvent is applied on a silicon wafer by spin coating. (b) A patterned PDMS stamp is placed on the ink; solvent permeates through the stamp creating a rigidified NP-based nanostructure as guided by the features in the stamp. (c) Patterned NP-based film is obtained upon removal of the stamp.

### 5.3.1 High Aspect-ration ITO Nanostructures Using Nanoparticle Inks

Ink comprising ITO NPs dispersed in NMP is obtained by replacing isopropyl alcohol (IPA) with NMP in commercially available ITO dispersion in IPA. The choice of solvent is driven by three factors, the solvent should have low vapor pressure to allow a broader time-window to spin-coat and place the stamp by preventing the spin coated film to quickly dry off, it should avoid excessive swelling of PDMS, and it must have similar polarity as of the solvent present in initial dispersion in order to ensure dispersion stability after solvent exchange step. Figure 5.3a shows NP aggregates size distribution in

suspensions before and after exchanging solvent, as obtained by dynamic light scattering (DLS). The average aggregate size before and after changing solvent from IPA to NMP was 49 nm and 54 nm respectively, suggesting that there is negligible further agglomeration of NPs after changing solvent. Figure 5.3b shows optical image of ITO NP suspension in NMP obtained after solvent exchange step, which is stable for over an year with negligible precipitation. Figure 5.3c shows transmission electron microscopy (TEM) image of ITO NPs with majority of the particles below 30 nm in size.
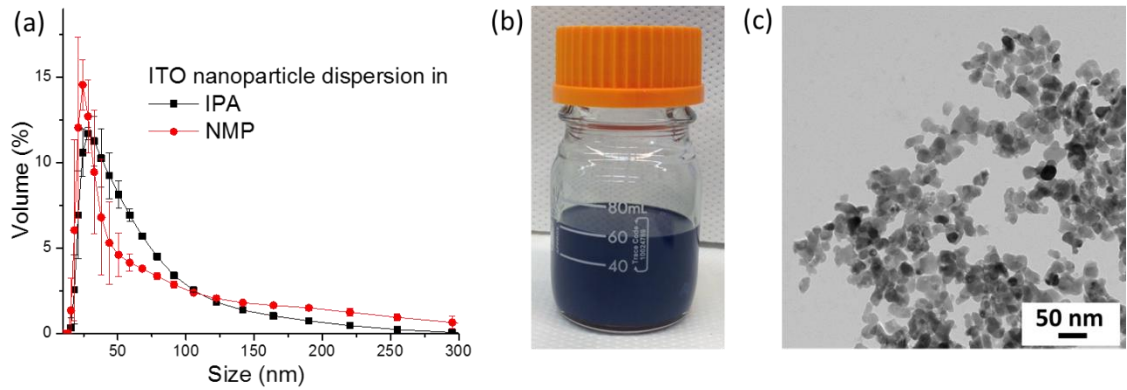


Figure 5.3 a)Particle size distribution of 5 wt% ITO dispersion in IPA (before solvent exchange) and 5 wt% ITO dispersion in NMP (after solvent exchange), as obtained by dynamic light scattering. (b) Digital photograph of ITO dispersion in NMP. (c) TEM image of ITO NPs.
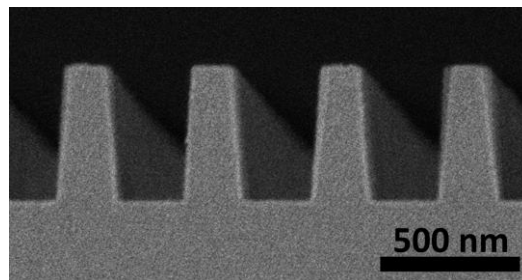


Figure 5.4 Cross section SEM of silicon master mold with gratin pattern used to make bilayer composite PDMS stamps. Line width at the base of the lines (LW), Pitch (P) and Line-height (LH) are ~210 nm, ~450 nm and ~480 nm respectively. Line width at the top of the line is ~150 nm. Sample was gold sputter coated before imaging.
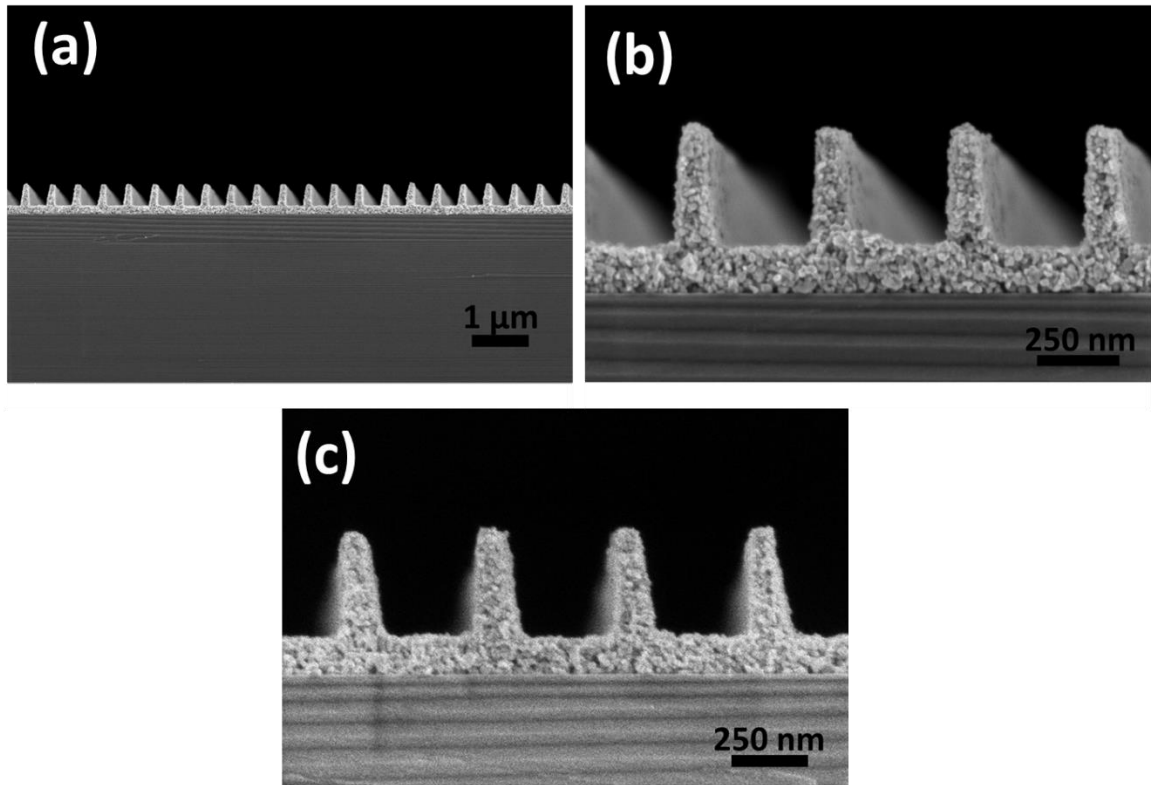
Figure 5.5 SEM images of ITO nanostructures - before and after calcination at 500 °C for 3 h - imprinted using ITO NPs dispersed in NMP. (a), (b) Cross section view of ITO grating pattern (LW, ~130 nm; LP, ~450 nm; LH, ~380 nm) imprinted with a composite PDMS stamp made using Si master mold shown in Figure 3. (c) Line pattern after heating at 500 °C for 1 h (LW, ~130 nm; LP, ~450 nm; LH, ~365 nm). Angle of tilt in (a-c) is less than 4° and in.

Figure 5.5 and Figure 5.6 shows SEM images of indium tin oxide (ITO) nanostructures imprinted using crystalline ITO NP-based ink and a patterned bilayer composite-PDMS stamp. The composite-PDMS stamp consists of thin layer of patterned hard-PDMS (h-PDMS) backed by a thick layer of Sylgard-184 PDMS.[186] ITO dispersion in NMP was spin coated and a patterned composite PDMS stamp was gently placed on the

spin-coated 'wet' film. Stamp was removed after the solvent permeates through it, leaving behind dried patterned film comprised of NPs.

Figure 5.5a and Figure 5.5b shows the cross-section SEM images at two different length scales of ITO grating structure imprinted with a square inch sized composite PDMS tamp made using hard silicon master mold shown in Figure 5.4. Line-width at the base of the lines (LW), line pitch (LP) and line height (LH) of printed grating structure are ~130 nm, ~450 nm and ~380 nm respectively, whereas the LW , P and LH of the silicon master from which patterned composite PDMS stamp is made are ~210 nm, ~450 nm and ~480 nm respectively. The reduction in the printed features height is due to the volumetric shrinkage accompanied by removal of solvent through PDMS after placing the stamp for imprinting. The imprinted features are uniform in size and shape throughout the pattern. Once the imprinting is achieved, these crystalline NP-based features maintain structural integrity upon heating at elevated temperatures, which is often required during calcination and annealing of metal oxides in order to improve their physical properties, for example conductivity in the case of ITO. Figure 4(c) shows cross-section view of the grating structure (LW, ~130 nm; P, ~450 nm; LH, ~365 nm) after heating at 500 C for 1 h, providing a line height shrinkage of ~4%. Figure 7c shows X-ray diffraction (XRD) pattern for planar ITO NP-based thin film before and after heat treatment at 500 °C, confirming Bragg reflections corresponding to cubic $In_2O_3$ (space group $Ia\overline{3}$) crystal structure. Average crystallite size before and after heat treatment as determined by the line broadening of primary (222) reflection using Scherrer equation was 14.6 nm and 16.2 nm respectively, suggesting that shrinkage upon heating is mostly due to the removal of residual organic material in the films.
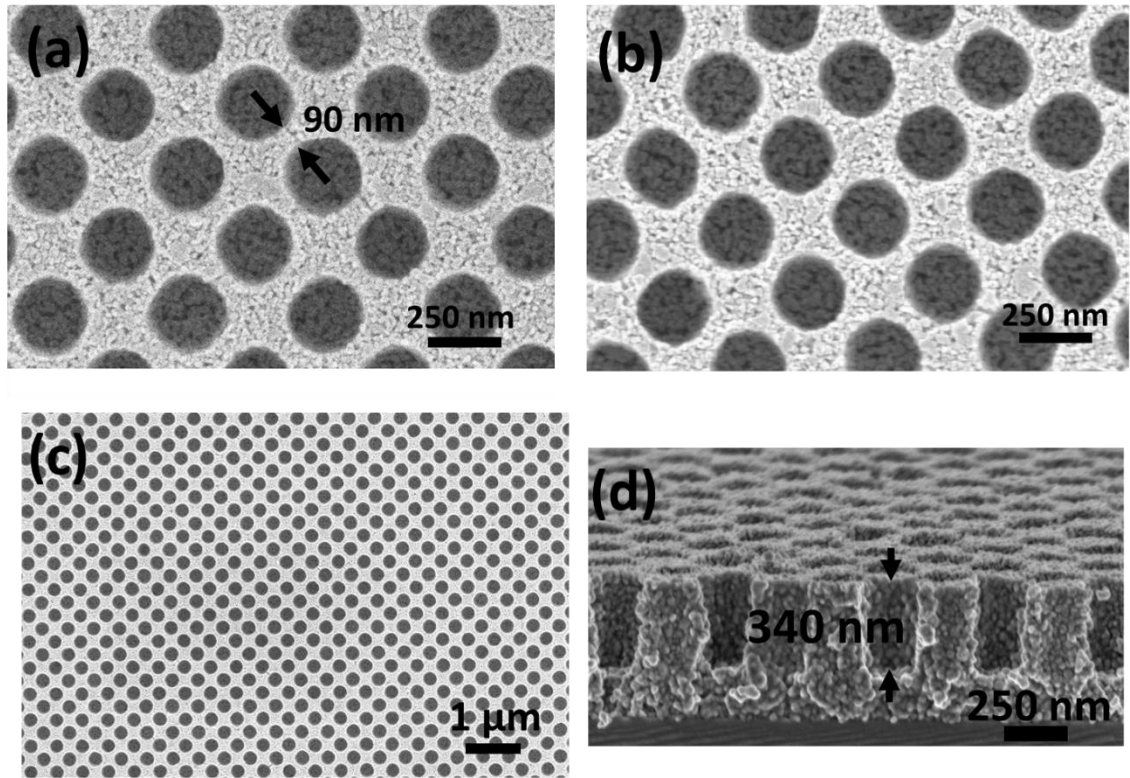
Figure 5.6 SEM images of ITO nanostructures - before and after calcination at 500 °C for 3 h - imprinted using ITO NPs dispersed in NMP. (a) Top SEM image of ITO via features imprinted in square array pattern (hole radius (HR), ~125 nm; hole pitch (HP), ~340 nm; hole depth (HD), ~355 nm) imprinted from ITO NPs dispersed in NMP using a composite PDMS stamp. (b), (c) Top view of via features after heating at 500 °C for 1 h (HR, ~122 nm; HP, ~340 nm; HD, ~340 nm). (d) shows cross section view of via features after heating at 500 °C.
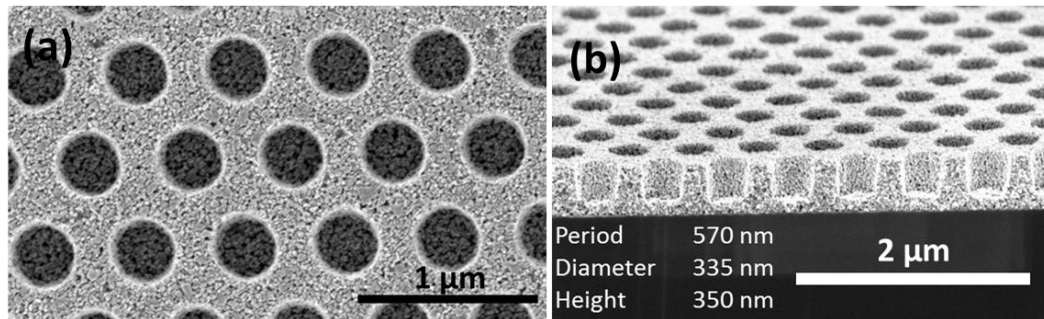


Figure 5.7 (a) Top view (b) Tilted view of a hexagonal hole array pattern imprinted using ITO NPs dispersed in NMP as ink.

Figure 5.6a shows via structures with hole radius (HR) ~125 nm, center to center distance between nearest holes, i.e. hole pitch (HP) ~340 nm and hole depth (HD) ~355 nm imprinted in a square array pattern. The imprinted structure therefore has a minimum hole-wall thicknesses of ~90 nm, suggesting that closely packed sub-100-nm features can also be imprinted using this strategy. Figure 5.6b and Figure 5.6c shows top view at two different magnifications and Figure 5.6c shows cross-section of via pattern after heating at 500 °C for 1 h. The HR, HP and HD of 500 °C heated sample were 125 nm, 330 nm and 340 nm respectively, suggesting a low linear-shrinkage of less than 5%. The surface area of these high aspect-ratio lines and holes patterns is ~2.7 folds and ~4.3 folds of their projected area respectively. Such high surface area transparent conductive oxides nanopatterns are useful for many applications, for example as solar cell electrodes for improved device effeciency.[187,188] The residual ITO layer at the base of the patterns is desirable for such an application. Figure 5.7 shows a hexagonally arranged via pattern imprinted using ITO NPs dispersed in NMP.
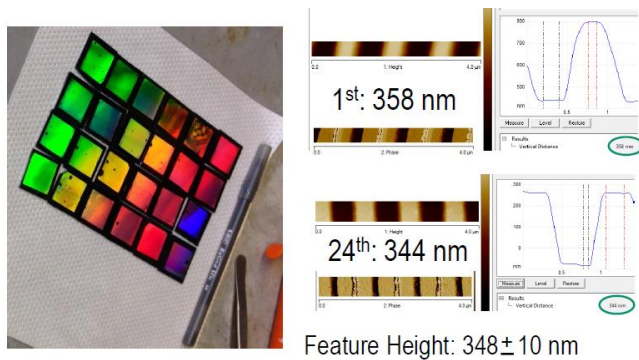


Figure 5.8 Digital photograph of 24 ITO grating line pattern samples of size 2.54 cm x 2.54 cm imprinted at 120 °C with 15 seconds imprint time per sample (Left). Line-height measurement of first and last sample using AFM, with line height of all 24 samples between 348+/-10 nm (Right). Color variation in the image arise due to different interference colors produced by the grating patterns at different viewing angles.

### 5.3.2 Rapid Nanoimprinting of ITO Using Inks Containing Nanoparticles

Dynamics of pattern generation depend on the rate of solvent removal via diffusion into the PDMS stamp, which can result in prolonged imprint times at room temperature. The diffusion rate can be improved by imprinting at moderately high temperatures. To assess the speed and reproducibility for creating the patterned nanostructures, we imprinted 24 consecutive 2.54 cm x 2.54 cm array pattern of ITO gratings (LW, ~320 nm; LP, ~1 µm; LH, ~350 ± 10 nm) using a single PDMS stamp (LW, ~475 nm; LP, ~950 nm; LH, ~475 nm) at 120 °C. Ink was spin coated on Si wafers for 2 minutes and stamp was placed. Samples were then instantly heated at 120 °C for 15 seconds and the stamp was removed to obtain the patterned nanostructure. Figure 5.8 shows the digital photograph of the 24 samples; line height for all samples as measured by atomic force microscopy varied between 348+/-10 nm and line height of the corresponding Si master mold was ~480 nm. Such low imprinting times are crucial for high volume manufacturing of nanostructures.

### 5.3.3 ITO Nanostructures Using Inks Containing Nanoparticles and Sol

Imprinting into the inks comprising high loading of crystalline ITO NPs in ITO sol made using metal salt precursors also offers good dimensional stability and rapid processibility. Ink prepared by mixing ITO NP suspension in NMP and ITO sol (indium nitrate and tin (IV) acetate solution in NMP) in a proportion to provide '$x$' wt% ITO solid content from NP and '100-$x$' wt% from sol upon calcination at 500 °C is denoted by '$x$ NP/100-$x$ sol ITO-ink', and its corresponding films are denoted by '$x$ NP/100-$x$ sol ITO'. Figure 6 shows ITO gratings imprinted using 80 NP/20 sol ITO-ink. The composite PDMS stamp used for imprinting was made using hard silicon master mold shown in Figure 5.4.

The ink was spin coated for a prolonged period of time to evaporate majority of solvent prior to placement of the stamp. Unlike NP films, NP and sol films remained wet even several hours after spin coting as stable sol keeps the film viscous after removal of the majority of solvent. The stamp was gently pressed against the wet film followed by heating the substrate at 150 °C for 30 seconds to convert viscous sol into rigidified xerogel. Imprinted pattern was obtained after removal of the stamp. Extend of sol to xerogel conversion within solvent permeable stamp was slower at lower temperatures with imprinting at 120 °C for 30 seconds resulted in distorted (due to low rigidity) features and imprinting at room temperature required more than 48 h to form rigid features. Figure 5.9a shows as-imprinted gratings at 150 °C with ~385 nm tall lines. The pattern was then calcined at 500 °C for 1 h (Figure 5.9b) to remove residual organic material and convert xerogel into crystalline phase, which resulted in line height reduction to 355 nm (~8% linear shrinkage) . Figure 5.10c shows XRD for the calcined planar 100 sol ITO and 80 NP/20 sol ITO thin films indicating a crystalline morphology with average crystallite size 7.6 nm and 16.2 nm respectively. Inks with lower ITO sol content, for example 90 NP/10 sol ITO-ink, resulted in rigid films after spin coating for several minutes. Such inks therefore required solvent-assisted imprinting, akin to patterning complete NP-based films as described earlier.
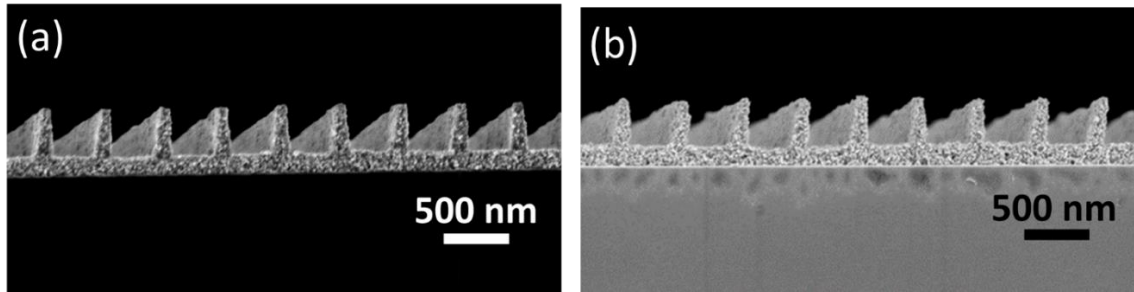
Figure 5.9 (a) ITO gratings imprinted in 30 seconds at 150 °C using an ink prepared by mixing ITO NP suspension and ITO sol-gel precursor solution in a proportion to provide 80 wt% ITO content from NPs suspension and 20 wt% from sol-gel solution. Height of imprinted features is ~385 nm. Imprinted was performed with a composite PDMS stamp made using hard silicon master mold shown in Figure 3. (b) Grating pattern upon calcination at 500 °C for 1 hr. The structure height is reduced to ~355 nm (approximately 8% shrinkage).

The relative proportions of crystalline NPs and sol in the ink determines dimensional stability upon calcination. Figure 5.10a shows reductions in film thickness measured using mechanical profilometer of room temperature dried planar films upon calcination at 500 C for 1 h. Films with greater than 80 wt% ITO content from NPs yielded thickness reductions of less than 20%. Films fabricated using NPs and sol showed lower sheet resistance compared to the films fabricated using only NPs. To measure sheet resistance, planar films were calcined for 1 h at 500 °C in air and annealed for 3 h at 300 °C in a stream of nitrogen to increase concentration of oxygen vacancies. Sheet resistance of a 200 nm thick 80 NP/20 sol ITO film was 400-450 Ω/sq. Sheet resistance of a 95 NP/5 sol ITO, 100 NP ITO and 100 sol ITO films with similar thicknesses (180-230 nm) were 2,000 Ω/sq and 9,000 Ω/sq and 200-250 Ω/sq respectively. Tremendous improvement in conductivity by adding sol to provide just 20% ITO content from sol can be attributed to reduced porosity of the films, and superior quality of ITO from sols compared to the ITO form NPs. Porosity in NP-based films arise from the interstitial voids between assembled

122

NPs upon removal of the solvent, which can strongly vary with the size distribution of NPs in the film.
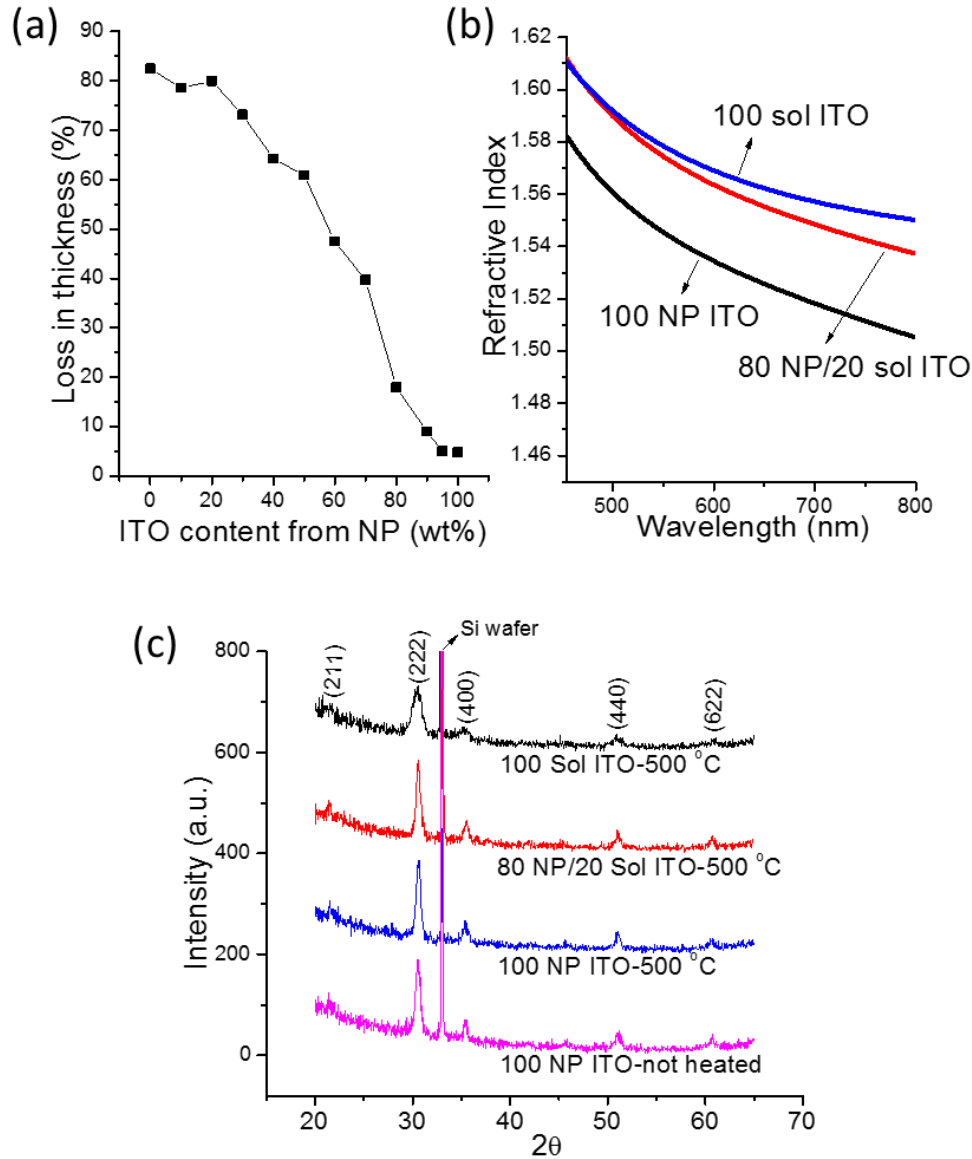


Figure 5.10 a) Shrinkage in planar ITO thin films composed of different amounts of ITO from NPs and sol-gel precursor (based on solid content contributed by the two components upon calcination at 500 °C). Initial thickness is measured after drying the spin coated planar film at room temperature for 72 h. Percentage loss in thickness is determined after calcination at 500 C for 1 h. (b) Refractive index of 500 °C calcined planar ITO thin films. (c) XRD diffractograms of planar ITO thin films with Bragg reflections corresponding to the cubic In2O3 crystal structure.

To compare porosity in the thin films, RI was characterized using spectroscopic ellipsometry. RI fitting was performed by minimizing mean-square error (MSE) using general oscillator layer model for ITO that came with the spectrometer's own software. Figure 5.10b shows RI between 450-800 nm for 500 °C calcined 100 NP ITO, 80 NP/20 sol ITO and 100 sol ITO thin films on Si substrate. Thickness of the films, RI at 633 nm and MSE values are shown in Table 5.1. The small MSE values (less than 20) signifies good fitting of RI data. Considering RI of dense ITO as 1.858 at 633 nm,[189,190] porosity as calculated using Lorentz-Lorenz effective medium approximation model[191] is 31.5% for 100 NP ITO, 28.3% for 80/20 ITO and 27.6% for 100 sol ITO films. While slightly reduced porosity in ITO films prepared with sol content will decrease their resistivity, the staggering improvement in conductivity of the sol-based films is attributed to the better quality of ITO form homemade sol compared to the NP dispersion supplied by the vendor. Sheet resistance of our films are also superior or comparable to that reported by other researchers using solution processable NP[192, 193] and sol-gel based techniques.[194-196] Planar ITO films made by NP –based ink and NP/Sol-based ink showed excellent optical transparency with above 90% (Figure 5.11a) transmittance in the visible range, which also suggest that there is no precipitation of large aggregates during film formation by these methods.

Table5.1 Fitted thickness, MSE and RI of planar ITO films on Si substrate calcined at 500 °C for 1 h.

|                  | Thickness (nm) | MSE | RI at 633 nm |
| ---------------- | -------------- | --- | ------------ |
| 100 NP ITO       | 114            | 9.7 | 1.528        |
| 80 NP/20 sol ITO | 166            | 11  | 1.558        |
| 100 sol ITO      | 74             | 12  | 1.564        |
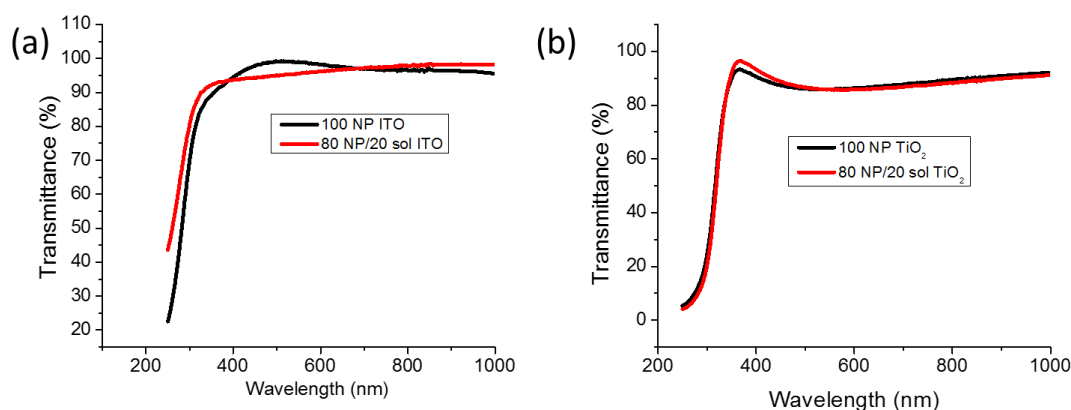
Figure 5.11 (a) Transmittance of ITO thin films on quartz. (b) Transmittance of $TiO_2$ thin films on quartz

### 5.3.4   $TiO_2$ Nanostructures Using Inks Containing Nanoparticles and Sol

To further extent solvent assisted NP-based imprinting to other metal oxides, imprinting of $TiO_2$ nanostructures is demonstrated. $TiO_2$ NP dispersions for inks were obtained by replacing water in commercially available acid-stabilized aqueous $TiO_2$ (anatase phase) NP dispersion with a NMP-methanol solvent mixture. The particle size distribution in suspensions, as shown in Figure 5.12a of $TiO_2$ aggregates before (8.7 nm) and after (7.9 nm) solvent change from water to NMP- methanol mixture remained almost same. Figure 8b shows optical image of NP suspension in NMP- methanol mixture, which is stable for over an year with negligible precipitation. Figure 5.12a shows TEM image of drop-casted $TiO_2$ NPs with the majority of particles below 8 nm.
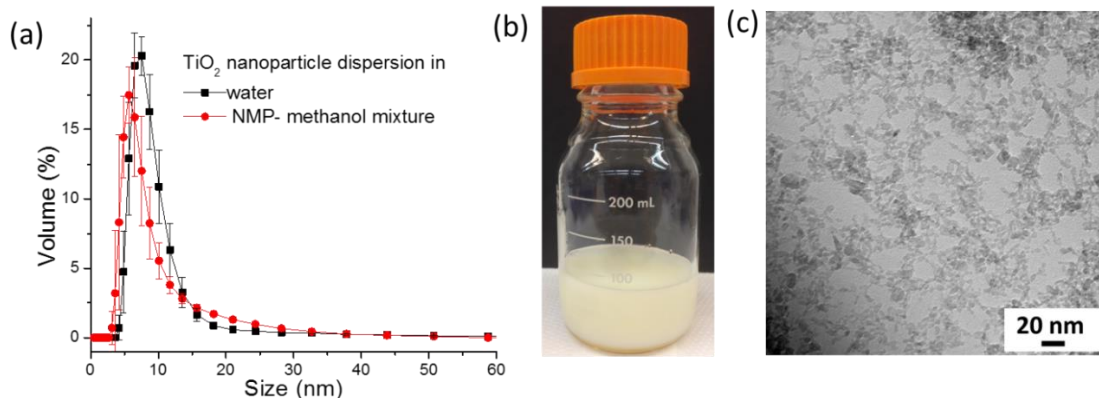
Figure 5.12 Particle size distribution of 5 wt% TiO$_2$ dispersion in water (before solvent exchange) and in NMP- methanol mixture (after solvent exchange), as obtained by dynamic light scattering. (b) Digital photograph of TiO$_2$ dispersion in NMP-methanol mixture. (c) TEM image of TiO$_2$ NPs.

Titania nanostructures were imprinted with inks comprised of different proportions of TiO$_2$ NPs dispersion (in NMP-methanol) and TiO$_2$ sol, titanium diisopropoxide bis(acetylacetonate) (TPA) in IPA. Solvent assisted imprinted was performed with a composite PDMS stamp made using master mold shown in Figure 5.4. Samples were subjected to 10 Jcm$^{-2}$ energy dose of 365 nm broadband UV light after placing the stamp for imprinting in order to cure TPA sol into rigid xerogel. Figure 9 shows cross sectional SEM of imprinted features composed of 100% TiO$_2$ NP (100 NP TiO$_2$), 80/20 (by weight) TiO$_2$ NP/TPA (80 NP/20 sol TiO$_2$) and 100% TPA (100 sol TiO$_2$) with feature height of 385 nm, 380 nm and 270 nm respectively, which upon calcination at 500 °C for 3 h reduce to 360 nm (~5% shrinkage), 340 nm (~11% shrinkage) and 140 nm (~49% shrinkage) respectively. Figure 10 (b) shows XRD of planar films before and after calcined at 500 °C for 3 h having anatase-TiO$_2$ reflection with mean crystallite size growing form 3.8 nm to 13.5 nm. The dimensional instability associated with enormous shrinkage observed upon

calcination to obtain a crystalline phase in conventionally used sol-gel based NIL technique lead to distorted features (Figure 5.13f) in contrast to this, low shrinkage upon calcination in features majorly comprising crystalline NPs imprinted using the solvent-assisted NIL technique demonstrated here rendered dimensionally stable nanostructures (Figure 5.13d, Figure 5.13e). Figure 5.13g shows 100 NP $TiO_2$ sample upon heating at 750 °C for 3 h resulted in line height reduction to ~320 nm (~17% shrinkage). XRD on 750 °C treated 100 NP $TiO_2$ film confirmed a transition from anatase- to rutile-$TiO_2$ phase and grain growth to 29.8 nm. Stable nanostructures with low-shrinkage resulting even after phase transition accompanied by significant grain growth in NP-based patterning technique is a promising development over sol-gel based patterning technique.

Planar films of 100 NP $TiO_2$ and 80 NP/20 sol $TiO_2$ showed transmittance greater than 90% in visible regime (Figure 5.11b) suggesting that NPs do not precipitate to form big agglomerates upon evaporation of the solvent during film formation.
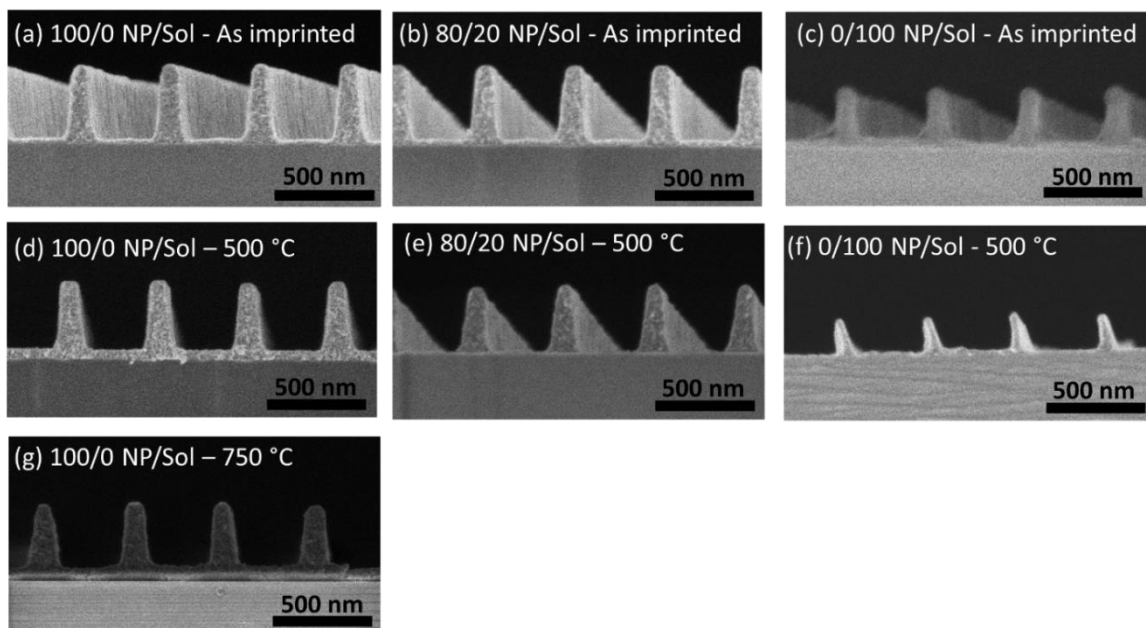
Figure 5.13 Cross-section SEM images of patterned TiO$_2$ gratings imprinted with inks having different weight ratios of TiO$_2$ NPs and UV curable TPA sol. (a-c) As-imprinted gratings; (a) 100 NP (LH, 385 nm), (b) 80 NP/20 sol (LH, 380 nm) (c) 100 sol (LH, 275 nm) imprinted with a composite PDMS stamp (LH, 480 nm) made using hard master mold shown in Figure 3 and cured under UV. (d-f) Gratings upon calcination at 500 $^\circ$C for 3 h; (d) 100 NP (LH, 360 nm), (e) 80 NP/20 sol (LH, 340 nm), (f) 100 Sol (LH, 140 nm). (g) 100 NP grating pattern upon calcination at 750 $^\circ$C for 3 h.

TiO$_2$ due to its high RI and transparency is interesting for its application in photonic devices to manipulate visible light. Figure 10(a) shows measured RI of 3 h-500 $^\circ$C clacined anatase-TiO$_2$ planar films. Cauchy model was used to fit the RI data, which is suitable for TiO$_2$ because of its transparency and low absorbance in the visible spectrum. RI of films containing NPs are lower than film made using only TPA sol. Thickness of the films, MSE values, RI at 633 nm are shown in Table 1. The small MSE values (less tha 20) signifies good fitting of RI data. Considering RI of dense TiO$_2$ as 2.49 at 633 nm[197], porosity as calculated using Lorentz-Lorenz effective medium approximation model[191] is 23.3% in 100 NP TiO$_2$ film, 25.6% in 80 NP/20 sol TiO$_2$ film and 18.5% for 100 sol TiO$_2$ film.

Unlike in case of ITO, RI of $TiO_2$ NP films did not improve by addition of the sol. We believe that the RI in NP based films can be further improved by choosing a dispersion with broader particle size distribution.

Table 5.2 Fitted thickness, MSE and RI of planar $TiO_2$ films on Si substrate calcined at 500 °C for 3 h.

|  | Thickness (nm) | MSE | RI at 633 nm |
|---|---|---|---|
| 100 NP $TiO_2$ | 86 | 7 | 1.960 |
| 80 NP/20 sol $TiO_2$ | 103 | 17 | 1.917 |
| 100 sol $TiO_2$ | 70 | 9 | 2.056 |
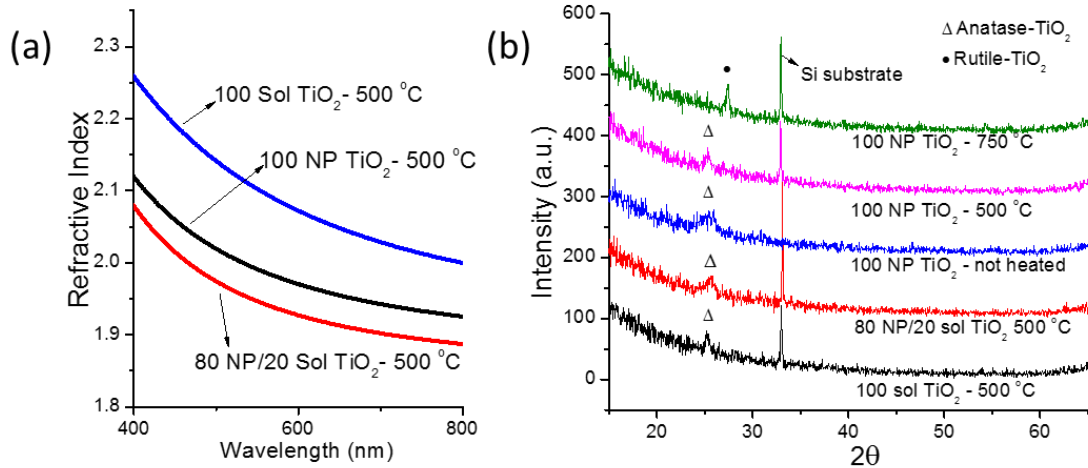


Figure 5.14 Characterization of planar $TiO_2$ thin films made with inks having different weight ratios of $TiO_2$ NPs and UV curable TPA sol (a) Refractive Index of 100 NP, 80 NP/20 sol and 100 Sol films calcined at 500 °C for 3 h. (b) XRD patterns of 100 NP, 80 NP/20 sol and 100 sol films calcined at different temperatures for 3 h.

### 5.3.5 Direct Imprinting of Residual-layer Free Inorganic Oxide Nanostructures

Many applications require free-standing features without a residual layer. By taking the advantage of low surface energy of the stamp, inks with low viscosity and appropriate advancing and receding contact angle on the stamp material can be dragged on

129

the surface of the stamp to fill the recesses without leaving any residue on the surface[198]. Such discontinuous wetting approach has been used to fill different elastomeric stamps with metal oxide sols, followed by imprinting on the substrate to achieve a residual-layer free pattern[180, 185]. The rate of dragging of the ink, and the swelling of the stamp encountered due to an additional thick layer of solvent applied between stamp and substrate in order to pull out depressed solidified-ink from stamp-recesses on to the substrate can limit the imprinting speed in this method.[185]

In contrast to discontinuous wetting of the stamp, residual-layer free direct imprinting can be practiced by application of modest pressure to squeeze-out low viscosity ink from between stamp/substrate interface during the imprinting process. Imprinting of gold features with minimal residual layer have been optimized using a low viscosity and surface tension gold NP suspension in α-terpineol and a 5 PSI imprint pressure. This technique has also recently been optimized to imprint residual-free patterns of organic small molecules, which are further polymerized by thermal initiation.[199,200] Here we take a similar approach to demonstrate residual-layer free imprinting of titania lines. The ink comprise of ~3 wt% $TiO_2$ NP dispersion in propanedio-methanol solvent mixture, obtained upon diluting 20 wt% $TiO_2$ NP stock dispersion in propanediol by methanol. The ink was spin-coated (at 3,000 RPM) on silicon wafer in a 70-80% relative humidity environment for about 2 minutes after which PDMS stamp (LW, ~425 nm; LP, ~950 nm; LH, ~480 nm) was placed and gently pressed with hand. Substrate was then heated to 120 °C for 15 seconds and the stamp was removed to obtain residual-layer free line pattern (Figure 11) with ~300 nm line height. In our case, high relative humidity was found to be important to obtain high quality residual-layer free imprints. High humidity leads to thinner NP-based

films suggesting that the interaction of ink with substrate is weaker at higher humidity, which will enable easy dewetting of the ink at stamp/substrate interface during the imprinting process. It is also found that ultrasonication right before the use was essential to reduce the viscosity of dispersion and achieve minimum residual-layer.
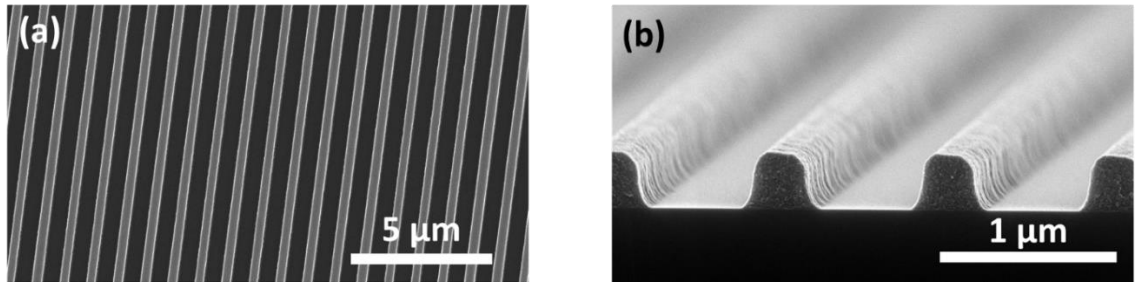


Figure 5.15 (a) Top view and (b) Tilted view of a residual layer-free $TiO_2$ grating pattern
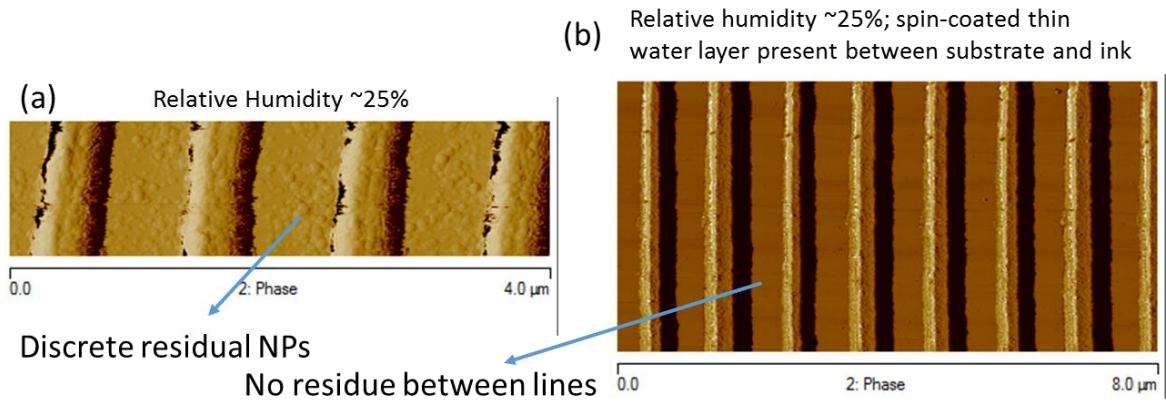


Figure 5.16 $TiO_2$ lines imprinted at 25% relative humidity using $TiO_2$ NPs suspension in propanediol-methanol. (a) Ink normally imprinted showing residue (b) Thin film of water spin coated on wafer before spin-coating ink, leaving no residue.

Figure 5.16a shows AFM image of lines imprinted at low humidity (25% RH). Discrete residual NPs between the lines can clearly be seen in the phase image. Residual free imprinting at low humidity could also be achieved by spin coating a water on wafer,

followed by quickly spin-coating ink on top of it, such that thin water film is present between ink and substrate. Spin coating ink after 3 seconds of spin-coating water rendered uniformly spun films without defects. The thin film of ink was then imprinted using PDMS stamp. This trick mimic's high humidity environment where thin layer of water molecules is adsorb over the silicon surface. AFM of lines printed even at 25% RH showed no residue. (Figure 5.16b).

ITO nanostructures with minimal residual layer were also imprinted by dispensing a 5µl drop of 3 wt% ITO NPs in IPA ( cannot be spin-coated for imprinting, as IPA evaporates quickly) and pressing PDMS stamp with 3 kg weight at its center (stamp area 1 square inch). Figure 5.17 shows imprinted ITO grating liens with a few NPs between them. The imprinted pattern is non-uniform at a macro scale because pressure was not evenly distributed. Using a thermal nanoimprinting or hydraulic press tool, pressure can be uniformly distributed to get high quality residual-layer free imprinted structures.
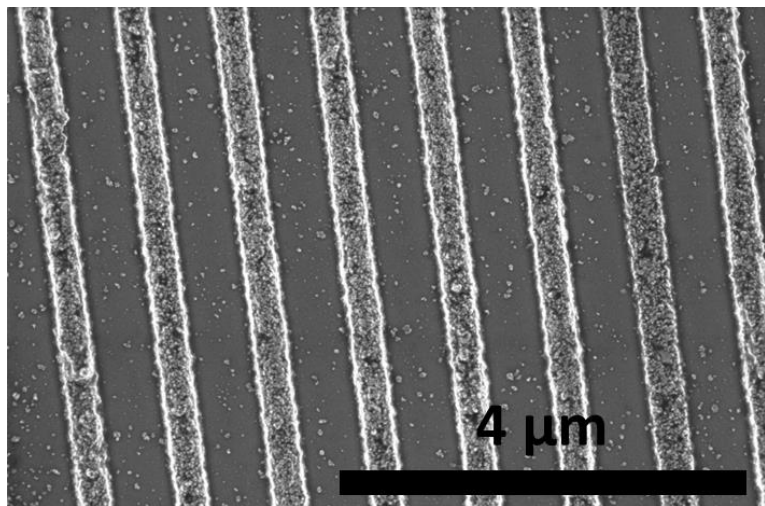


Figure 5.17 Imprinted ITO lines with no residual-layer but a few discrete NPs between the lines.

### 5.3.6 Indirect Imprinting of Residual-layer Free Inorganic Oxide Nanostructures

To imprint completely residual-layer free grating lines of ITO, an indirect imprinting method utilizing a sacrificial polymer nanostructure as template is developed. Figure 5.18 shows schematics of the method developed.
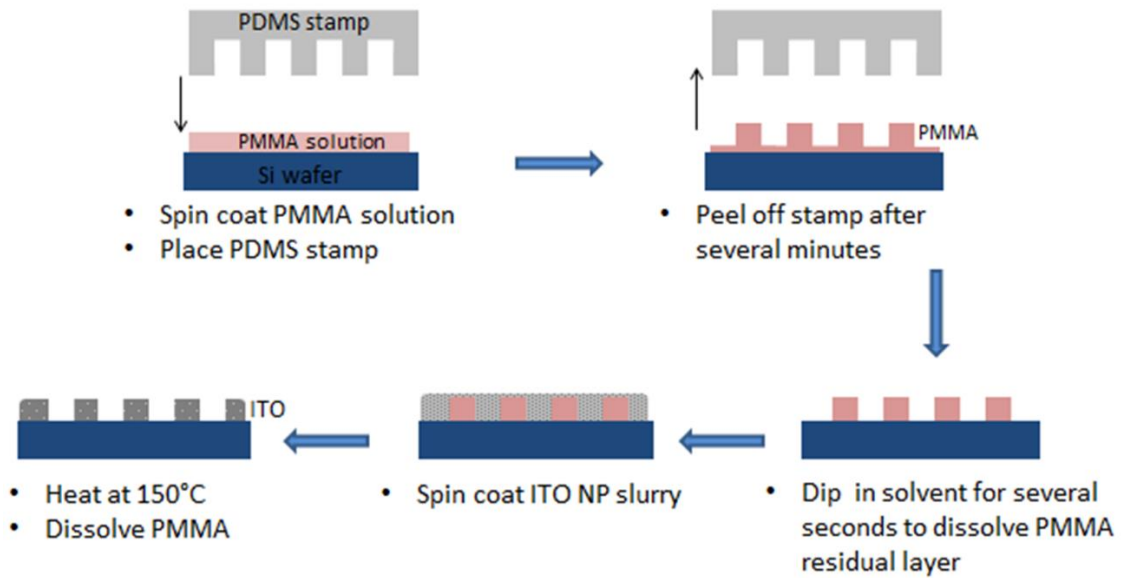


Figure 5.18 Schematics for the fabrication of all solution processable residual-layer free ITO grating lines by using poly (methyl methacrylate) grating lines as a sacrificial template.

In a typical process 996 kg/mol poly (methyl methacrylate) (PMMA) is spin coated on Si wafer from a 2.75 wt% solution in PGMEA at 2,600 rpm for 5 seconds. A PDMS stamp (LW, ~425 nm; LP, ~950 nm; LH, ~480 nm) is placed on the spin-coated film to perform solvent-assisted imprinting. Stamp is peeled off after placing the wafer at 60 °C for 2 minutes. The obtained PMMA pattern is then baked at 100 °C for 30 minutes to remove residual solvent and densify PMMA. The residual-layer between the grating lines, as determined by AFM is less than 25 nm. To remove the residual layer, wafer is dipped for 90-120 seconds (at room temperature) into a flask containing toluene (~50 ml) while

stirring the solvent using a magnetic bar. Soon after taking out of the toluene flask, wafer is flushed with a squirt of fresh toluene followed by IPA and dried under a jet of nitrogen. Baking the pattern before dipping into toluene was found to be necessary to avoid distortion of the lines and fast dissolution of them material during the toluene treatment. Time for which pattern is treated with toluene to get rid of residual-layer is sensitive to the ambience temperature, with a slight drop in temperature requiring longer treatment times. Figure 5.19 shows AFM and SEM images of the pattern obtained after toluene treatment with line height 230-280 nm. Thickness of the residual-layer between the lines after toluene treatment, as determined using AFM was below 5 Å (Figure 5.20), which is negligible.
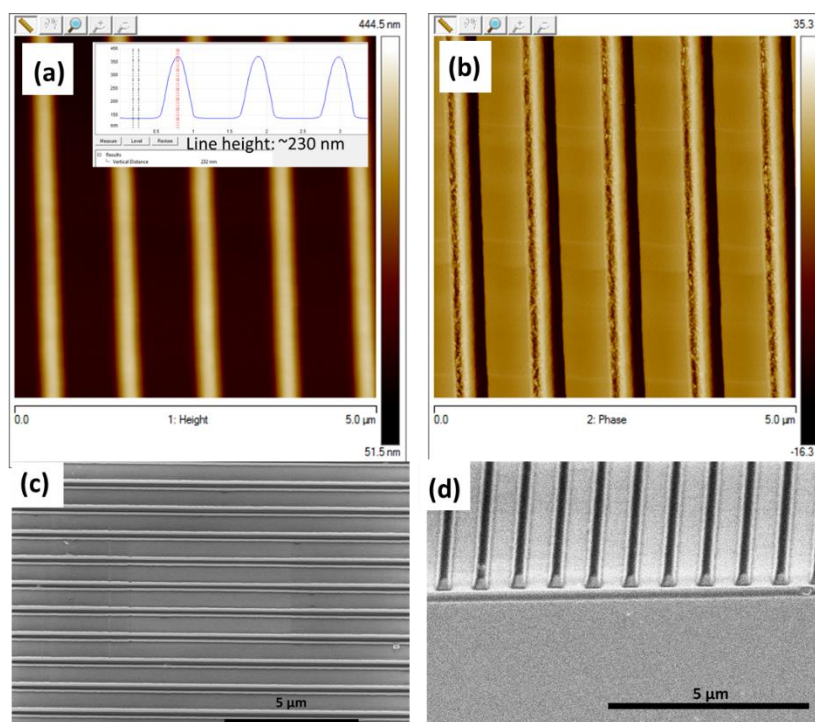


Figure 5.19 (a) AFM height image, (b) AFM phase image (c) top SEM image and (d) 45° tilted SEM image of residual-layer free PMMA grating pattern obtained after toluene treatment.
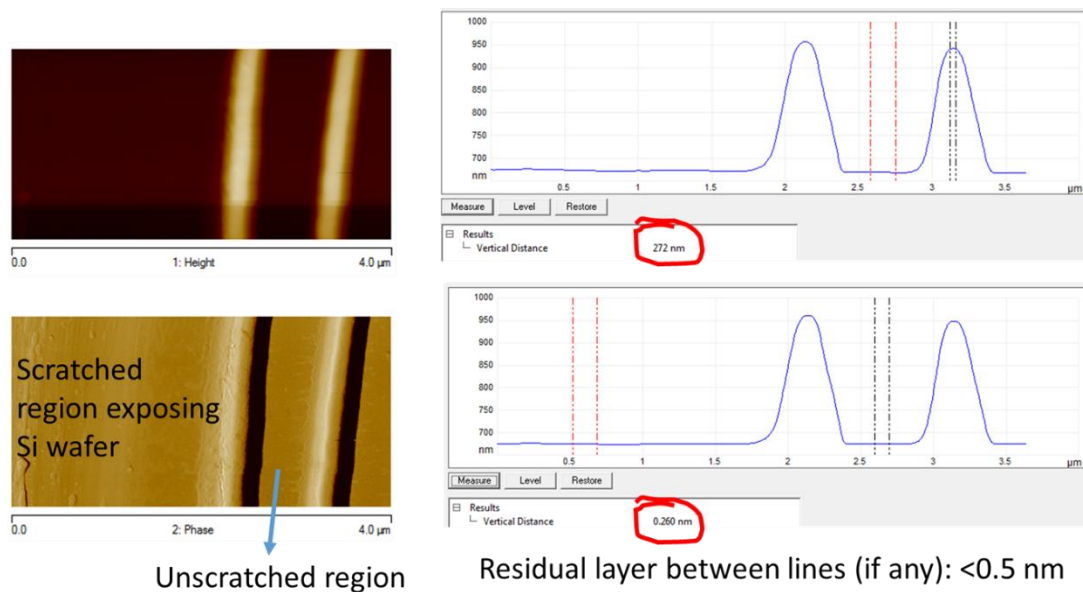
Figure 5.20 AFM height and phase images of PMMA pattern scratched to determine residual layer thickness after treating with toluene. Thickness of the remaining residual layer is below 0.5 nm, which is negligible.

In the next step, 3-5 wt% ITO in IPA is spin coated at 3,000 RPM on top of the residual-layer free PMMA pattern. ITO is uniformly coated on PMMA grating lines and in between the lines where there is no PMMA. The wafer is then heated at 150 °C for 30 minutes to improve adhesion between the nanoparticles and the wafer surface. Finally, residual layer free ITO-grating pattern is obtained by dissolving PMMA grating lines in NMP for 5 minutes along with sonication. Figure 5.21 shows SEM images at different magnifications of thus obtained residual-layer free ITO pattern. The pattern has lines in place of the spaces in the initial residual-layer free PMMA pattern, and spaces in place of the initial PMMA lines.
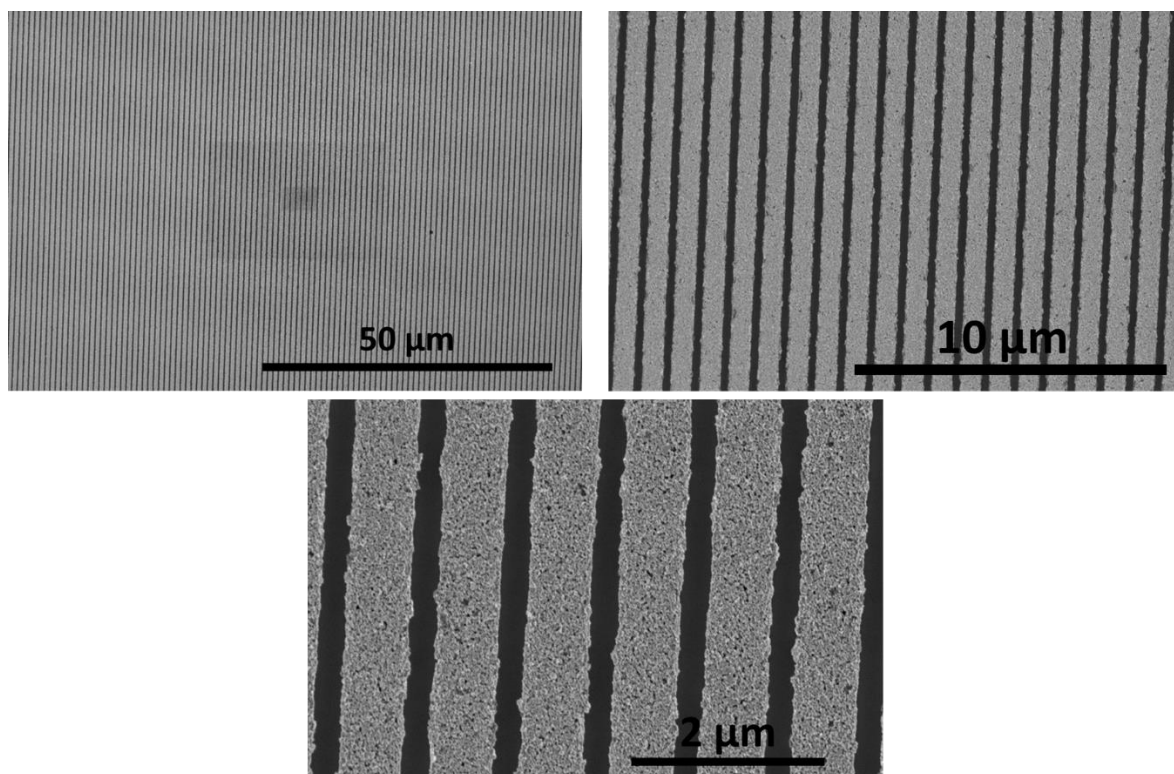
Figure 5.21 Residual-layer free ITO grating lines obtained by indirect imprinting method, utilizing residual-layer free PMMA pattern as a sacrificial template.

### 5.3.7 3D Inorganic Nanostructures Using Solvent-assisted Soft Lithography

The ability to print features with minimal residual layer has enabled the fabrication of three dimensional nanostructures using a simple print-planarize-print approach (Figure 5.22). The first grating layer on Si wafer is imprinted using ~3 wt% $TiO_2$ NPs dispersion in propanediol-methanol solvent mixture as ink and a PDMS stamp (LW, ~425 nm; LP, ~950 nm; LH, ~480 nm) in 60-80% relative humidity environment. Imprinting time is 10 seconds at 120 °C. The height of the imprinted line can be tuned between 250-300 nm by simply varying spin speed (about 2,000-3,000 RPM) or the concentration of the ink. In the second step the structure is planarized with a UV-crosslikable low viscosity organic

thiolene-acrylate prepolymer (NOA60, Norland Products Inc.) by spin-coating from a 20 wt% NOA 60 solution in propylene glycol monomethyl ether acetate (PGMEA) solvent followed 10 wt% NOA60 solution in PGMEA, with UV curing after each spin coating step. A low power oxygen plasma treatment before coating each planarization layer is found to improve the quality of the quality of planarization layer. The low viscosity of NOA60 allows effective planarization (grating height reduce to 2-5 nm as measured by AFM) while leaving a thin residual layer atop of the first grating structure (100- 150 nm). The imprinting and planarization process is then simply repeated for desired number of layers. Finally the organic planarization layer is removed by calcining at elevated temperature. Since crosslinked organic layers do not flow when heated, patterned inorganic layers remains unperturbed when they come in contact. Figure 5.23a and Figure 5.23b shows a bilayer and a tetralayer with ~240 nm grating-width at the top of the grating line following calcination to remove the planarization layer. Figure 5.23c shows the bilayer after annealing at 850 °C for 1 h with grating width reduce to ~200 nm. The structure remains stable despite conversion of $TiO_2$ from initial anatase to rutile phase, as indicated by XRD (Figure 5.24), and coarsening of the NP crystallites to 34.2 nm. Figure 5.23c shows the tetralayer after calcination at 1000 °C for 1 h with XRD (Figure 5.24) suggesting highly crystalline rutile morphology with sharp higher order peaks.

3D inorganic metal oxide nanostructures

Planarized using UV crosslinkable polymer
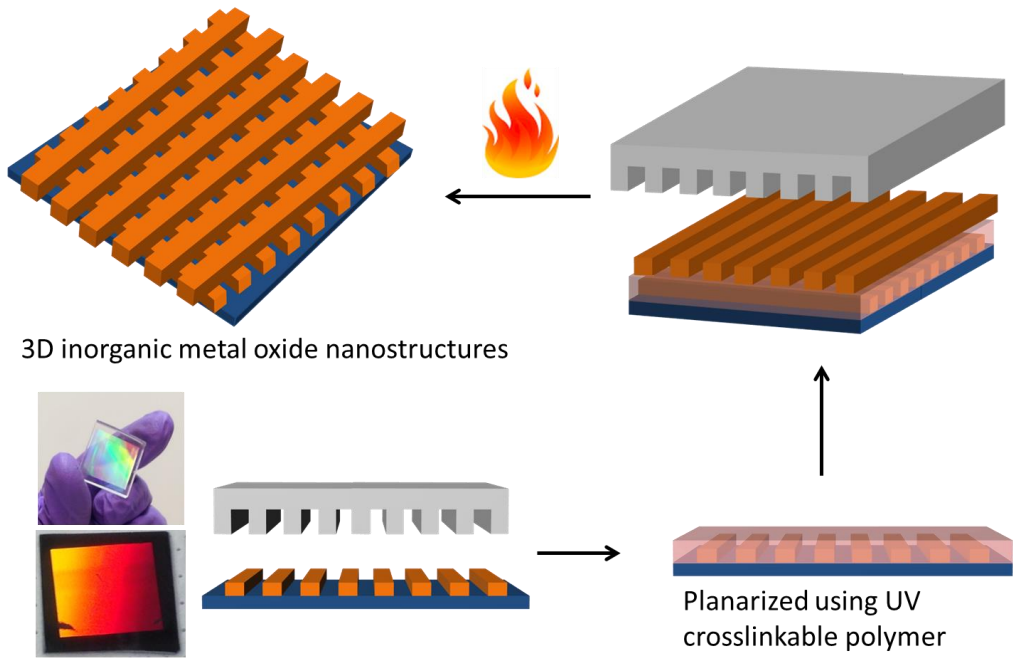
13

Figure 5.22 Schematics of fabrication of a 3D metal oxide nanostructure by a print-planarize-print approach followed by calcination to remove organic planarazing layer.

Figure 5.25 shows other complex 3D shapes, with lines on pillars and high density 2D alternating lines and pillars pattern and ladder shaped patterns that can be fabricated using print-planarize-print approach. The first imprinted layer was of pillar pattern and the second imprinted layer was of line pattern. NOA 60 planarization layer was used in between. Pattern was obtaind upon calcination to remove planarizing layer.
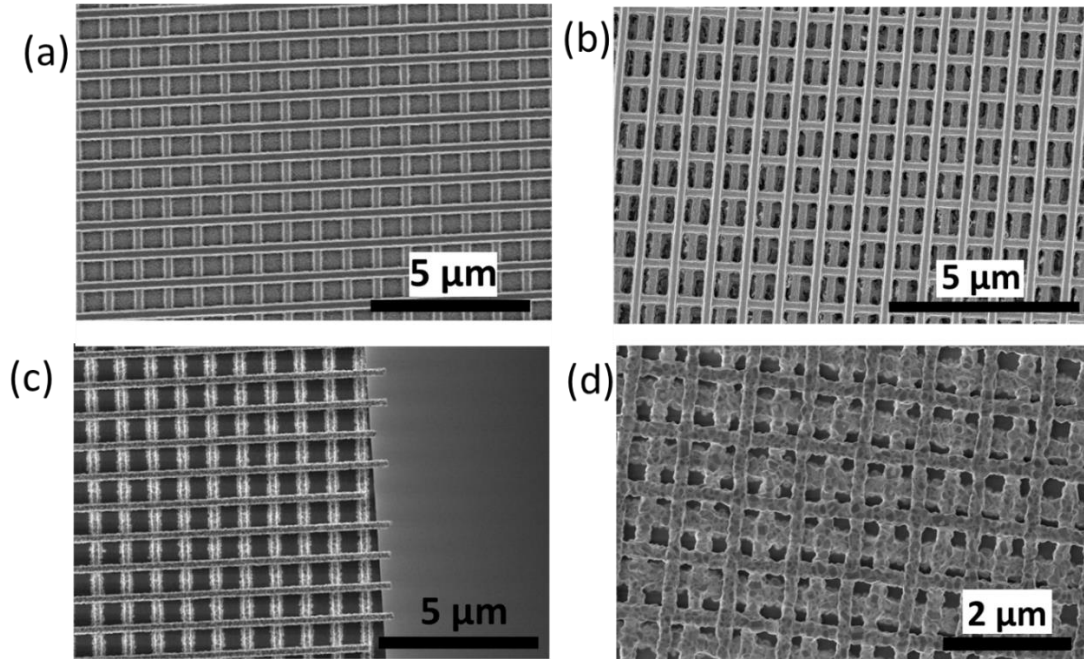
Figure 5.23 TiO$_2$ 3D nanostructures fabricated using print-planarize-print approach. (a) Bilayer and (b) tetralayer after removal of organic planarizing layer by calcination. (c) Bilayer heated to 850 °C for 1 h. (d) Tetralayer heated at 1000 °C for 1 h.
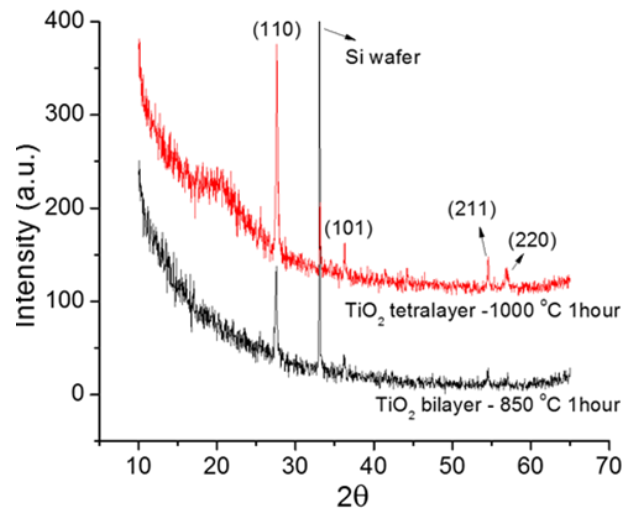


Figure 5.24 XRD showing rutile reflections of TiO$_2$ bilayer and tetralayer after annealing at 850 °C and 1000 °C respectively.
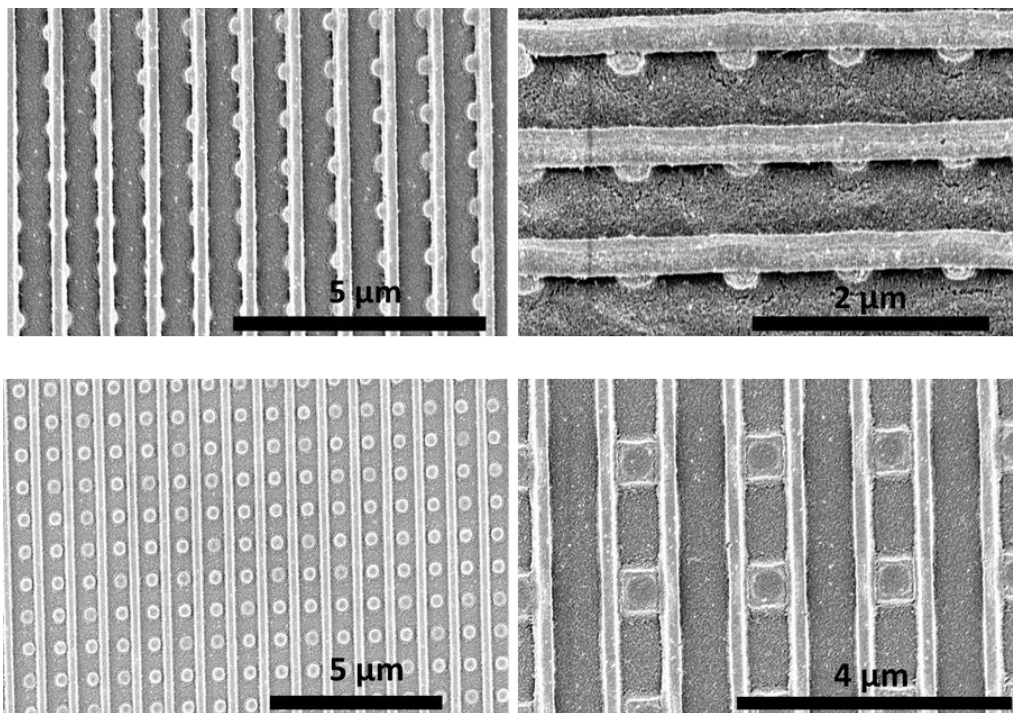
Figure 5.25 Various complex 3D and 2D pattern fabricated using print-planrarize-print approach.

## 5.4 Conclusion

We have shown that a variety of high aspect ratio crystalline inorganic oxide nanostructures can be directly fabricated by practicing solvent/thermal/UV-assisted soft nanoimprint lithography on inks containing oxide nanoparticles. Our nanoparticle based soft imprinting technique is capable of producing large area nanopatterns in a rapid fashion. The low-shrinkage at elevated temperatures observed in crystalline nanoparticle based nanopatterns (less than 5% in some cases) is a significant development over previously explored sol-gel based methods that suffer from enormous shrinkage when imprinted xerogels is heated to obtain a crystalline morphology. The porosity in nanoparticle based features is comparable to that obtained by sol-gel based methods. The technique is also

extended to generate residual-layer free nanopatterns and 3D nanopatterns by using a print-planarize-print approach.

Recent progress is the design and synthesis of a myriad of NPs with well controlled size below 15 nm, size distribution and surface chemistry by solvothermal and hydrothermal techniques provides a palette of starting materials for broad ranges of applications.

## 5.5   Acknowledgements

# BIBLIOGRAPHY

[1]     Leibler, L. *Macromolecules* **1980**, *13*, 1602-1617.

[2]     Bates, F. S.; Fredirckson, G. H. *Annu. Rev. Phys. Chem.* **1990**, *41*, 525-557.

[3]     Bates, F. S.; Fredirckson, G. H. *Phys. Today* **1999**, *52(2)*, 32-38

[4]     Hong, S.W.; Huh, J.; Gu, X.; Lee, D. H.; Jo, W. H.; Park, S.; Xu, T.; Russell, T. P. *PNAS* **2012**, *109*, 1402-1406.

[5]     Ruiz, R.; Kang, H. M.; Detcheverry, F. A.; Dobisz, E.; Kercher, D. S.; Albrecht, T. R.; de Pablo, J. J.; Nealey, P. F. *Science* **2008**, *321*, 936–939.

[6]     Bita, I.; Yang, J. K. W.; Jung, Y. S.; Ross, C. A.; Thomas, E. L.; Berggren, K. K. *Science* **2008**, *321*, 939–943.

[7]     Cheng, J. Y.; Ross, C. A.; Chan, V. Z.; Thomas, E. L.; Lammertink R. G. H.; Vancso, G. J. *Adv. Mater.* **2001**, *13*, 1174-1178.

[8]     Lopes, W. A.; Jaeger, H. M. *Nature* **2001**, *414*, 735-738.

[9]     Kim, H.-C.; Jia, X.; Stafford, C. M.; Kim, D. H.; McCarthy, T. J.; Tuominen, M.; Hawker, C. J.; Russell, T.P. *Adv. Mater.* **2001**, *13*, 795-797.

[10]    La, Y. H.; In, I.; Park, S. M.; Meagley, R. P.; Leolukman, M.; Gopalan, P.; Nealey, P. F.   *J. Vac. Sci. Technol. B* **2007**, *25*, 2508–2513.

[11]    Park, M.; Harrison, C.; Chaikin, P. M.; Register, R. A.; Adamson, D. H. Block. *Science* **1997**, *276*, 1401-1404.

[12]    Pai, R. A.; Humayun, R.; Schulberg, M. T.; Sengupta, A.; Sun, J.-N.; Watkins, J. J. *Science* **2004**, *303*, 507–510.

[13]    Tirumala, V. R.; Pai, R. A.; Agarwal, S.; Testa, J. J.; Bhatnagar, G.; Romang, A. H.; Chandler, C.; Gorman, B. P.; Jones, R. L.; Lin, E. K.; Watkins, J. J. *Chem. Mater.* **2007**, *19*, 5868–5874.

[14]    Nagarajan, S.; Li, M. Q.; Pai, R. A.; Bosworth, J. K.; Busch, P.; Smilgies, D. M.; Ober, C. K.; Russell, T. P.; Watkins, J. J. *Adv. Mater.* **2008**, *20*, 246–251.

[15]    Jeong, U.; Kim, H.-C.; Rodriguez, R. L.; Tsai, I. Y.; Stafford, C. M.; Kim, J. K.; Hawker, C. J.; Russell, T. P. *Adv. Mater.* **2002**, *14*, 274-276.

[16]    Chan, V. Z.-H.; Hoffman, J.; Lee, V. Y.; Iatrou, H.; Avgeropoulos, A.; Hadjichristidis, N.; Miller, R. D.; Thomas, E. L. *Science* **1999**, *286*, 1716-1719.

[17]   Urbas, A. et al. *Advanced Materials* **2000***, 12***,** 812-814.

[18]   Urbas, A.; Fink, Y.; and Thomas, E. L. *Macromolecules* **1999***, 32***,** 4748-4750.

[19]   Bockstaller, M. R., Mickiewicz, R. A., and Thomas, E. L. *Advanced Materials* **2005**, *17*,1331-1349.

[20]   Bates, F. **S.;** Rosedale, J. H.; Fredrickson, G. H. *J. Chem. Phys.* **1990,** *92*, 6255.

[21]   Bates, F. S. *Macromolecules* **1984**, *17*, 2607-2613.

[22]   Balsara, N. P.; Perahia, D.; Safinya, C. R.; Tirrell, M.; Lodge, T. P. *Macromolecules* **1992**, *25*, 3896-3901.

[23]   Winter, H. H.; Scott, D. B.; Gronski, W.; Okamoto, S.; Hashimoto, T. *Macromolecules* **1993**, *26*, 7236-7244.

[24]   Fredrickson, G. H.; Bates, F. S. *Annu. Rev. Mater. Sci.* **1996**, *26*, 501-550.

[25]   Yamaguchi, D.; Hashimoto, T.; Han, C. D.; Baek, D. M.; Kim, J. K.; Shi, A.-C. *Macromolecules* **1997**, *30*, 5832-5842.

[26]   Hahn, H.; Chakraborty, A. K.; Das, J.; Pople, J. A.; Balsara, N. P. *Macromolecules* **2005**, *38*, 1277-1285.

[27]   Han, C. D.; Baek, D. M.; Kim, J. K. *Macromolecules* **1990**, *23*, 561-570.

[28]   Kasten, H.; Stuhn, B. *Macromolecules* **1995***, 28*,4777

[29]   Hajduk, D. A.; Grunmer, S. M.; Erramilli, S.; Register, R. A.; Fetters, L. J. *Macromolecules* **1996**, *29*, 1473.

[30]   Folkes, M. J.; Keller, A. *Polymer* **1971**, *12*, 222.

[31]   Voronov, V. P.; Buleiko, V. M.; Podneks, V. E.; Hamley, I. W.; Fairclough, J. P. A.; Ryan, A. J.; Mai, S. M.; Kiao, B. X.; Booth, C.; *Macromolecules* **1997***, 30*, 6674.

[32]   Joo, J.; Shim, J.; Seo, H.; Jung, N.; Wiesner, U.; Lee, J.; Jeon, S. *Anal. Chem.* **2010**, *2*, 3032−3037.

[33]   Ogawa, M.; Kuroda, K.; Mori, J.-i. *Chem. Commun.* **2000**, 2441−2442.

[34]   Kageyama, K.; Tamazawa, J.-i.; Aida, T. *Science* **1999**, *285*, 2113−2115

[35]   Liu, A. M.; Hidajat, K.; Kawi, S.; Zhao, D. Y. *Chem. Commun*. **2000**, 1145−1146.

[36]   Nooney, R. I.; Kalyanaraman, M.; Kennedy, G.; Maginn, E. J. *Langmuir* **2000**, *17*, 528−533.

[37]   Liu, X.; Wang, R.; Xia, Y.; He, Y.; Zhang, T. *Sens. Lett.* **2011**, *9*, 698−702.

[38]   Domansky, K.; Liu, J.; Wang, L.-Q.; Engelhard, M. H.; Baskaran, S. *J. Mater. Res.* **2001**, *16*, 2810−2816.

[39]   Mellaerts, R.; Mols, R.; Kayaert, P.; Annaert, P.; Van-H, J.; Van-D, M; Martens, J. A.; Augustijns, P. *Int. J. Pharm.* **2008**, 357, 169–179.

[40]   Mellaerts, R.; Mols, R.; Jammaer, J. A.G.; Aerts, C. A.; Annaert, P.; Van-H. J.; Van-D. M. G.; Augustijns, P.; Martens, J. A. *Eur. J. Pharm.* **2008**, *69*, 223–230.

[41]   Gomez-Vega, J. M.; Iyoshi, M.; Kim, K. Y.; Hozumi, A.; Sugimura, H.; Takai, O. *Thin Solid Films* **2001**, 615−620.

[42]   Wang, X.-P.; Li, X.; Onuma, K.; Ito, A.; Sogo, Y.; Kosuge, K.; Oyane, A. *J. Mater. Chem*. **2010**, *20*, 6437−6445.

[43]   Crossland, E. J. W.; Nedelcu, M.; Ducati, C.; Ludwigs, S.; Hillmyer, M. A.; Steiner, U.; Snaith, H. J. *Nano Lett.* **2008**, *9*, 2813−2819.

[44]   Crossland, E. J. W.; Kamperman, M.; Nedelcu, M.; Ducati, C.; Wiesner, U.; Smilgies, D. M.; Toombes, G. E. S.; Hillmyer, M. A.; Ludwigs, S.; Steiner, U.; Snaith, H. J. *Nano Lett.* **2008**, *9*, 2807−2812.

[45]   Jose, R.; Thavasi, V.; Ramakrishna, S. *J. Am. Ceram. Soc.* **2009**, *92*, 289−301.

[46]   O'Regan, B.; Gratzel, M. *Nature* **1991**, *353*, 737−740.

[47]   Hendricks, N. R.; Watkins, J. J.; Carter, K. *J. Mater. Chem*., **2011**, *21*, 14213-1418.

[48]   Park, D.-H.; Nishiyama, N.; Egashira, Y.; Ueyama, K. *Ind. Eng. Chem. Res*. **2001**, *40*, 6105−6110.

[49]   Guliants, V. V.; Carreon, M. A.; Lin, Y. S. *J. Membr. Sci.* **2004**, *235*, 53−72

[50]   Beck, J. S.; Vart, J. C.; Roth, W. J.; Leonowicz, M. E.; Kresge, C. T.; Schmitt, K. D.; C. T-W.; Olson, D. H.; Sheppard, E. W.; McCullen, S. B.; Higgins, J. B., Schlenkert, J. L. *J. Am. Chem. Soc*., **1992**, *114*, 10834-10843

[51]   Kresge, C.T; Leonowicz, M. E.; Roth, W. J.; Vartuli, J.C.; Beck, J.S., *ibid*. **1992**, *359*, 710

[52] J. S. Beck *et al.*, *J. Am. Chem. Soc.* **1992***, 114*, 10834

[53] Zhao, D.; Feng, J.; Huo, Q.; Melosh, N.; Fredrickson, G. H.; Chmelka, B.; Stucky, G. D. *Science* **1998**, *279*, 548-552.

[54] Pai, R. A.; Humayun, R.; Schulberg, M. T.; Sengupta, A.; Sun, J. N.; Watkins, J. J. *Science* **2004,** *303*, 507.

[55] Nagarajan, S; Bosworth, J. K.; Ober, C. K.; Russell, T. P.; Watkins, J. J. *Chem. Mater.* **2008,** *20,* 604–606.

[56] John, J.; Tang, Y.; Rothstein, J. P.; Watkins, J. J.; Carter, K. R.,. *Nanotechnology* **2013***,* 24, (50), 505307.

[57] Park, J. Y.; Hendricks, N. R.; Carter, K. R. *Langmuir* 27, (17), 11251-11258

[58] Demko, M. T.; Cheng, J. C.; Pisano, A. P. *ACS applied materials & interfaces* **2012**, *6*, 6890–6896

[59] Kim, Enoch, Xia, Younan and Whitesides, G. M. *Nature* **1995**, *376*, 581–584

[60] Demko, M. T.; Brackbill, T. P.; Pisano, A. P. *Langmuir* **2012**, *28*, 9857–63.

[61] Demko, M. T.; Brackbill, T. P.; Pisano, A. P. *Langmuir* **2012**, *28*, 9857–63

[62] Kim, E.; Xia, Y.; Zhao, X.; Whitesides, G. M. *Advanced Materials* **1997**, *9*, 651–654

[63] Lee, M. H.; Huntington, M. D.; Zhou, W.; Yang, J.; Odom, T. W. *Nano letters* **2011**, *11*, 311–315.

[64] Black, C. T. A*pplied Physics Letters* **2005***, 87,* 163116

[65] Black, C.T.; Guarini, K.W.; Milkove, K. R.; Baker, S. M.; Russell, T. P. and Tuominen, M. T. *Applied Physics Letters* **2011***, 79,* 409-411.

[66] Bladon, P.; Griffin, A. C. *Macromolecules* **1993**, *26*, 6604-6610.

[67] Alexander, C.; Jariwala, C. P.; Lee, C. M.; Griffin, A. C. *Macromol. Symp.* **1994**, *77*, 283-293.

[68] Lehn, J.-M. *Macromol Symp.* **1993**, *69*, 1-17.

[69] Fouquey, C.; Lehn, J.-M.; Levelut, A.-M. *Adv. Mater.* **1990**, *2*, 254–257.

[70] Kihara, H.; Kato, T.; Uryu, T.; Fréchet. J. M. J. *Chem. Mater.* **1996**, *8*, 961-968.

[71] Kihara, H.; Kato, T.; Uryu, T.; Fréchet. J. M. J. *Liq. Cryst.* **1998**, *24*, 413-418.

[72] Kato, T.; Fréchet, J. M. J. *Macromolecules* **1989**, *22*, 3818-3819.

[73] Araki, K.; Kato, T.; Kumar, U.; Fréchet, J. M. J. *Macromol. Rapid Commun.* **1995**, *16*, 733-739.

[74] Bazuin, C. G.; Brandys, F. A. *Chem. Mater.* **1992**, *4*, 970-972.

[75] Brandys, F. A.; Bazuin, C. G. *Chem. Mater.* **1996**, *8*, 83-92.

[76] Stewart, D.; Imrie, C. T. *J. Mater. Chem.* **1995**, *5*, 223-228.

[77] Malik, S. Dhal, P. K.; Mashelkar, R. A. *Macromolecules* **1995**, *28*, 2159-2164.

[78] Ruokolainen, J.; Makinen, R.; Torkkeli, M.; Makela, T.; Serimaa, R.; ten Brinke, G.; Ikkala, O. *Science* **1998**, *280*, 557-560.

[79] Ruokolainen, J.; Saariaho, M.; Ikkala, O.; ten Brinke, G.; Thomas, E. L.; Torkkeli, M.; Serimaa, R. *Macromolecules* **1999**, *32*, 1152-1158.

[80] Chao, C. Y.; Li, X.; Ober, C. K. *Pure Appl. Chem.* **2004**, *76*, 1337-1343.

[81] Ruokolainen, J.; ten Brinke, G.; Ikkala, O. *Adv. Mater.* **1999**, *11*, 777-780.

[82] Bondzic, S.; Wit, J. d.; Polushkin, E.; Schouten, A. J.; ten Brinke, G.; Ruokolainen, J.; Ikkala, O.; Dolbnya, I.; Bras, W. *Macromolecules* **2004**, *37*, 9517-9524.

[83] Tung, S. H.; Kalarickal, N. C.; Mays, J. W.; Xu, T. *Macromolecules* **2008**, *41*, 6453–6     462.

[84] van Zoelen, W.; Asumaa, T.; Ruokolainen, J.; Ikkala, O.; ten Brinke, G. *Macromolecules* **2008**, *41*, 3199–3208.

[85] Osuji, C.; Chao, C.-Y.; Bita, I.; Ober, C. K.; Thomas, E. L. *Adv. Funct. Mater.* **2002**, *12*, 753-758

[86] Daga, V. K.; Watkins, J. J. *Macromolecules* **2010**, *43*, 9990-9997.

[87] Tirumala, V. R.; Romang, A.; Agarwal, S.; Lin, E. K.; Watkins, J. J. *Adv. Mater.* **2008**, *20*, 1603-1608.

[88] Lin, Y.; Daga, V. K.; Anderson, E. R.; Gido, S. P.; Watkins, J. J. *J. Am. Chem. Soc.* **2011**, *133*, 6513–6516.

[89]    Kothari, R.; Winter, H. H.; Watkins, J. J., *Macromolecules* **2014**, 47, (22), 8048-8055

[90]    Huang, C. I.; Chen, J. R.. *Journal of Polymer Science Part B: Polymer Physics* **2001,** 39, (21), 2705-2715.

[91]    Bates, F. S. *Macromolecules* **1984**, *17*, 2607-2613.

[92]    Balsara, N. P.; Perahia, D.; Safinya, C. R.; Tirrell, M.; Lodge, T. P. *Macromolecules* **1992**, *25*, 3896-3901.

[93]    Winter, H. H.; Scott, D. B.; Gronski, W.; Okamoto, S.; Hashimoto, T. *Macromolecules* **1993**, *26*, 7236-7244.

[94]    Fredrickson, G. H.; Bates, F. S. *Annu. Rev. Mater. Sci.* **1996**, *26*, 501-550.

[95]    Yamaguchi, D.; Hashimoto, T.; Han, C. D.; Baek, D. M.; Kim, J. K.; Shi, A.-C. *Macromolecules* **1997**, *30*, 5832-5842.

(96)    Hahn, H.; Chakraborty, A. K.; Das, J.; Pople, J. A.; Balsara, N. P. *Macromolecules* **2005**, *38*, 1277-1285.

[97]    Winter, H. H.; Three Views of Viscoelasticity for Cox-Merz Materials. *Rheol Acta* **2009**, *48*, 241-243.

[98]    CS ChemDraw Ultra 11.0 Software

[99]    Gilli, P.; Pretto, L.; Bertolasi, V.; Gilli, G.  *Acc. Chem. Res.* **2009**, *42*, 33-44

[100]   Vairam, S.; Govindarajan, S. New Hydrazinium. *Thermochimica Acta* **2004**, *414*, 263-270.

[101]    Brown, H.C.; Baude, E. A.; Nachod, F. C. *Academic Press, New York* **1955.**

[102]   Haruta, M.; Yamada, N.; Kobayashi, T.; Lijima, S. *J. Catal.* **1989** , *115* , 301

[103]   Haruta, M.; Tsuboda, S.; Kobayashi, T.; Kagehiama, H.; Genet, M. J.; Demon, B.; *J. Catal.* **1993**, 144, 175

[104]   Polshettiwar, V.; Len, C.; Fihri, A. *Coord. Chem. Revs.* **2009**, *253,* 2599

[105]    Polshettiwar, V.; Molnar, A. *Tetrahedron* **2007**, *63*, 6949

[106]   Hirai, H.; Nakao, Y.; Toshima, N. J.;  *Macromol. Sci. Chem.* **1978**, *A12*, 1117

[107]   Chen, G.; Guo, C.-Y.; Huang, Z.; Yuan, G., *Chem. Eng. Res. Design.* **2011**, *89,* 249

[108]   Tucker C. E.; Vries, J. G. de, *Top. Catal.* **2002** , *19* , 111

[109]  Kim S. – W.; , Kim, M.; Lee, W. Y.; Hyeon, T. *J. Am. Chem. Soc.* **2002** , *124* , 7642

[110]  Yashima, M; Falk, L. K. L.; Palmqvist, A. E. C.; Holmberg, K. *J. Colloid Interfac. Sci.* **2003**,*268*, 348

[111]  Schauermann, S.; Hoffmann, J.; Johanek, V.; Hartmann, J.; Libuda, J.; Freund, H.-J. *Angew. Chem.* **2002**, *114*, 2643

[112]  Kaneda, K.; Higushi, M.; Himanaka, T. *J. Mol. Cat. A: Chem.* **2001**, *63*, L33

[113]  Choi, K. - M., Akita, T.; Mizugaki, T.; Ebitani, K.; Kaneda, K. *New J. Chem.* **2003**, *27*, 324

[114]  Wagner, M.; Köhler, K.; Djakovitch, L.; Mühler, M. *Top. Catal.* **1999** , *13* , 319

[115]  Köhler, K.; Djakovitch, L.; Wagner, M. *Catal. Today* **2001**, *66*, 105

[116]  M. Haruta, *J. New Mater. Electrochem. Syst.* **2004** , *7* , 163

[117]  Beller, M.; Zapf, A., in *Handbook of Organopalladium Chemistry for Organic Synthesis*, Vol. 1, Negishi E.-I. (Ed.), Wiley, Hoboken, **2002** , p. 1209

[118]  Baumeister, P.; Meyer, W.; Oertle, K; Seifert, G.; Seifert, H., *Chimia* **1997**, *51*, 144

[119]  Chen, W.; Cai, W.; Zhang, L.; Wang, G.; Zhang, L. *J. Colloid Interface Sci.* **2001**, *238*, 291-295

[120]  Wakayama, H.; Setoyama, N.; Fukushima, Y. *Adv. Mater.* **2003**, *15*, 742-745

[121]  Mukherjee, P.; Patra, C. R.; Ghosh, A.; Sastry, M.; Kumar, R. *Chem. Mater.* **2002**, 14, 1678

[122]  Mukherjee, P.; Patra, C. R.; Kumar, R.; Sastry, M.;  *PhysChemComm.* **2001**, *4,* 24

[123]  Ghosh, A.; Patra, C. R.; Mukherjee, P.; Sastry, M.; Kumar, R. *Microporous Mesoporous Mater.* **2003**, *58*, 201-211.

[124]  Hirai, T.; Okubo, H.; Komasawa, I. *J. Colloid Interface Sci.* **2001**, *235*, 358-364.

[125]  Rioux, R. M.; Song, H.; Hoefelmeyer, J. D.; Yang, P.; Somorjai, G. A. *J. Phys. Chem. B* **2005**, *109*, 2192–2202.

[126]  Hornyak, G.; Kroll, M.; Pugin, R.; Sawitowski, T.; Schmid, G.; Bovin, J.-O.; Karsson, G.; Hofmeister, H.; Hopfe, S. *Chem.sEur. J.* **1997**, *3*, 1951-1956.

[127] Gupta, G.; Shah, P. S.; Zhang, X.; Saunders, A. E.; Korgel, B. A.; Johnston, K. P. *Chem. Mater.* **2005**, *17*, 6728–6738.

[128] Gupta, G.; Stowell, C. A.; Patel, M. N.; Gao, X.; Yacaman, M. J.;Korgel, B. A.; Johnston, K. P. *Chem. Mater.* **2006**, *18*, 6239–6249.

[129]  King, N. C.; Blackley, R. A.; Zhou, W; Bruce, D. W. *Chem. Commun.*, **2006**, 3411-3413.

[130] King, N. C.; Blackley, R. A.; Wears, M. L.; Newman, D. M.; Zhou, W.; Bruce, D. W. *Chem. Commun.*, **2006,** 3414–3416.

[131] Song, H.; Rioux, R. M.; Hoefelmeyer, J. D.; Komor, R.; Niesz, K.; Grass, M.; Yang, P.; Somorjai, G. A. *J. Am. Chem. Soc.* **2006**, *128*, 3027–3037.

[132] Song, H.; Rioux, R. M.; Hoefelmeyer, J. D.; Komor, R.; Niesz, K.; Grass, M.; Yang, P.; Somorjai, G. A. *J. Am. Chem. Soc.* **2006**, *28*, 3027–3037.

[133] Ko´nya, Z.; Puntes, V. F.; Kiricsi, I.; Zhu, J.; Alivisatos, A. P.; Somorjai, G. A. *Nano Lett.* **2002**, *2*, 907.

[134] Gupta, G.; Patel, M.; Ferrer, D.; Heitsch, A. T.; Korgel, B. A.; Johnston, K. P. *Chem. Mater.* **2008,** *20,* 5005–5015.

[135] Wang, X.; Tilley, R. D.; Watkins, J. J. *Langmuir* **2014**, *30*, 1514−1521.

[136] Hendricks, N. R.; Kothari, R.; Wang, X.; Watkins, J. J., *Journal of Materials Chemistry C* 2, (29), 5938-5943

[137] Bagshaw, S. A. *Chemical Communications* **1999**, 1785–1786.

[138] Yuan, Z.-Y.; Blin, J.-L.; Su, B.-L. *Chemical Communications* **2002**, 504–505.

[139] Sun, J.; Shan, Z.; Maschmeyer, T.; Moulijn, J. A.; Coppens, M.-O. *Chemical Communications* **2001**, 2670–2671

[140] Wang, X.; Dou, T.; Xiao, Y. *Chemical Communications* **1998**, 1035–1036.

[141] El Haskouri, J.; Ortiz de Zárate, D.; Guillem, C.; Latorre, J.; Caldés, M.; Beltrán, A.; Beltrán, D.; Descalzo, A. B.; Rodríguez-López, G.; Martínez-Máñez, R.; Marcos, M. D.; Amorós, P. *Chemical Communications* **2002**, 330–331.

[142] Okabe, A.; Niki, M.; Fukushima, T.; Aida, T. *Journal of Materials Chemistry* **2005**, *15*, 1329.

[143] Zhang, X.; Guo. C.; Wang, X.; Wu, Y. *Journal of Wuhan University of Technology-Mater. Sci. Ed.* 2012, 27, 1084-88.

[144] Xiao, F.-S. *Catalysis Surveys from Asia* **2004**, *8*, 151–159.

[145] Pérez-Pariente, J.; Díaz, I.; Agúndez, J. *Comptes Rendus Chimie* **2005**, *8*, 569–578.

[146] Huang, L.; Wang, Z.; Sun, J.; Miao, L.; Li, Q.; Yan, Y.; Zhao, D. *Journal of the American Chemical Society* **2000**, *122*, 3530–3531.

[147] Wang, Y. J.; Tang, Y.; Ni, Z.; Hua, W. M.; Yang, W. L.; Wang, X. D.; Tao, W. C.; Gao, Z. *Chemistry Letters* **2000**, 510–511.

[148] Dong, A.; Wang, Y.; Tang, Y.; Zhang, Y.; Ren, N.; Gao, Z. *Advanced Materials* **2002**, *14*, 1506–1510.

[149] Yang, P.; Deng, T.; Zhao, D.; Feng, P.; Pine, D.; Chmelka, B. F.; Whitesides, G. M.; Stucky, G. D. *Science* **1998**, *282*, 2244–2246.

[150] Velev, O. D.; Jede, T. A.; Lobo, R. F.; Lenhoff, A. M. *Chemistry of Materials* **1998**, *10*, 3597–3602.

[151] Antonietti, M.; Berton, B.; Göltner, C.; Hentze, H.-P. *Advanced Materials* **1998**, *10*, 154–159.

[152] Holland, B. T.; Abrams, L.; Stein, A. *Journal of the American Chemical Society* **1999**, *121*, 4308–4309.

[153] Holland, B. T.; Blanford, C. F.; Do, T.; Stein, A. *Chemistry of Materials* **1999**, *11*, 795–805.

[154] Vaudreuil, S.; Bousmina, M.; Kaliaguine, S.; Bonneviot, L. *Advanced Materials* **2001**, *13*, 1310–1312.

[155] Sen, T.; Tiddy, G. J. T.; Casci, J. L.; Anderson, M. W. *Chemical Communications* **2003**, 2182–2183.

[156] Carn, F.; Colin, A.; Achard, M.-F.; Deleuze, H.; Sellier, E.; Birot, M.; Backov, R. *Journal of Materials Chemistry* **2004**, *14*, 1370–1376.

[157] Zhang, H.; Hardy, G. C.; Rosseinsky, M. J.; Cooper, A. I. *Advanced Materials* **2003**, *15*, 78–81.

[158] Sen, T.; Tiddy, G. J. T.; Casci, J. L.; Anderson, M. W. *Microporous and Mesoporous Materials* **2005**, *78*, 255–263.

[159] Caruso, R. A.; Antonietti, M. *Advanced Functional Materials* **2002**, *12*, 307–312.

[160] Huerta, L.; Guillem, C.; Latorre, J.; Beltrán, A.; Beltrán, D.; Amorós, P. *Chemical Communications* **2003**, 1448–1449.

[161] Maekawa, H.; Esquena, J.; Bishop, S.; Solans, C.; Chmelka, B. F. *Advanced Materials* **2003**, *15*, 591–596.

[162] Giunta, P. R.; Washington, R. P.; Campbell, T. D.; Steinbock, O.; Stiegman, A. E. *Angewandte Chemie* **2004**, *43*, 1505–1507.

[163] Zhao, D.; Yang, P.; Chmelka, B. F.; Stucky, G. D. *Chemistry of Materials* **1999**, *11*, 1174–1178.

[164] Davis, S. A.; Burkett, S. L.; Mendelson, N. H.; Mann, S. *Nature* **1997**, *385*, 420-423.

[165] Fukushima, Y.; Wakayama, H. *The Journal of Physical Chemistry B* **1999**, *103*, 3062–3064.

[166] Wakayama, H.; Fukushima, Y. *Chemical Communications* **1999**, 391–392.

[167] Wakayama, H.; Fukushima, Y. *Chemistry of Materials* **2000**, *12*, 756–761.

[168] Wakayama, H.; Itahara, H.; Tatsuda, N.; Inagaki, S.; Fukushima, Y. *Chemistry of Materials* **2001**, *13*, 2392–2396.

[169] Daga, V. K.; Watkins, J. J. *Macromolecules* **2010**, *43*, 9990–9997

[170] Vogt, B. D.; Pai, R. A.; Lee, H.-J.; Hedden, R. C.; Soles, C. L.; Wu, W.-l.; Lin, E. K.; Bauer, B. J.; Watkins, J. J., *Chemistry of materials* **2005,** 17, (6), 1398-1408

[171] Gratson, G. M.; Xu, M.; Lewis, J. A.,. *Nature* **2004,** 428, (6981), 386-386.

[172] Lewis, J. A.. *Current Opinion in Solid State and Materials Science* **2002,** 6, (3), 245-250.

[173] Duoss, E. B.; Twardowski, M.; Lewis, J. A.,. *Advanced Materials* **2007,** 19, (21), 3485-3489.

[174] Gratson, G. M.; García-Santamaría, F.; Lousse, V.; Xu, M.; Fan, S.; Lewis, J. A.; Braun, P. V. *Advanced Materials* **2006,** 18, (4), 461-465.

[175] John, J.; Tang, Y.; Rothstein, J. P.; Watkins, J. J.; Carter, K. R.,. *Nanotechnology* **2013**, 24, (50), 505307.

[176]   Schueller, O. J. A.; Whitesides, G. M.; Rogers, J. A.; Meier, M.; Dodabalapur, A. *Applied Optics* **1999,** 38, (27), 5799-5802.

[177]   Kim, W.-S.; Yoon, K. B.; Bae, B.-S., *Journal of Materials Chemistry* **2005,** 15, (42), 4535-4539.

[178]   Jo, H.-B.; Byeon, K.-J.; Lee, H.; Kwon, M.-H.; Choi, K.-W. *Journal of Materials Chemistry* **2102**, 22, (38), 20742-20746.

[179]    Beaulieu, M. R.; Hendricks, N. R.; Watkins, J. J. *ACS Photonics* **2014**, 1, (9), 799-805.

[180]   Hampton, M. J.; Williams, S. S.; Zhou, Z.; Nunes, J.; Ko, D.-H.; Templeton, J. L.; Samulski, E. T.; DeSimone, J. M. *Adv. Mater* **2008,** 20, (14), 2667-2673.

[181]    Ganesan, R.; Dumond, J.; Saifullah, M. S. M.; Lim, S. H.; Hussain, H.; Low, H. Y., *ACS Nano* **2012**, 6, (2), 1494-1502.

[182]    Hwang, J. K.; Cho, S.; Dang, J. M.; Kwak, E. B.; Song, K.; Moon, J.; Sung, M. M., *Nature nanotechnology* 5, (10), 742-748.

[183]    Li, M.; Tan, H.; Chen, L.; Wang, J.; Chou, S. Y., Large area direct nanoimprinting of SiO2 andTiO2 gel gratings for optical applications. *Journal of Vacuum Science & Technology B* **2003,** 21, (2), 660-663

[184]   Ko, S. H.; Park, I.; Pan, H.; Grigoropoulos, C. P.; Pisano, A. P.; Luscombe, C. K.; Frechet, J. M. J., *Nano letters* **2007,** 7, (7), 1869-1877

[185]    Hwang, J. K.; Cho, S.; Dang, J. M.; Kwak, E. B.; Song, K.; Moon, J.; Sung, M. M., *Nature nanotechnology* **2010**, 5, (10), 742-748

[186]    Odom, T. W.; Love, J. C.; Wolfe, D. B.; Paul, K. E.; Whitesides, G. M., *Langmuir* **2002,** 18, (13), 5314-5320.

[187]   Wang, F.; Subbaiyan, N. K.; Wang, Q.; Rochford, C.; Xu, G.; Lu, R.; Elliot, A.; D' Souza, F.; Hui, R.; Wu, J., *ACS applied materials & interfaces* **2012***,* 4, (3), 1565-1572.

[188]   Manca, M.; Beke, S.; De Marco, L.; Pareo, P.; Qualtieri, A.; Cannavale, A.; Brandi, F.; Gigli, G. *The Journal of Physical Chemistry C* **2014***,* 118, (30), 17100-17107

[189]    Konig, T. A. F.; Ledin, P. A.; Kerszulis, J.; Mahmoud, M. A.; El-Sayed, M. A.; Reynolds, J. R.; Tsukruk, V. V. *ACS nano* **2014***,* 8, (6), 6182-6192.

[190]  Refractive Index Reference – Online Sopra Material Database

[191]   Hutchinson, N. J.; Coquil, T.; Navid, A.; Pilon, L., *Thin Solid Films* 518, (8), 2141-2146.

[192]   Cheong, D.-S.; Yun, D. H.; Kim, D. H.; Han, K. R.. *Journal of the Korean Ceramic Society* **2011***,* 48, (6), 516-519.

[193]   Cho, Y.-S.; Kim, H.-M.; Hong, J.-J.; Yi, G.-R.; Jang, S. H.; Yang, S.-M.. *Colloids and Surfaces A: Physicochemical and Engineering Aspects* **2009,** 336, (1), 88-98

[194]   Su, C.; Sheu, T. K.; Chang, Y. T.; Wan, M. A.; Feng, M. C.; Hung, W. C., *Synthetic Metals* **2005,** 153, (1), 9-12.

[195]   Sunde, T. O. L. v.; Garskaite, E.; Otter, B.; Fossheim, H. E.; SÃ¦terli, R.; Holmestad, R.; Einarsrud, M.-A.; Grande, T. *Journal of Materials Chemistry* **2012** 22, (31), 15740-15749.

[196]   Kim, S.-S.; Choi, S.-Y.; Park, C.-G.; Jin, H.-W. *Thin Solid Films* **1999,** 347, (1), 155-160

[197]   Refractive index database at Filmetrics.com

[198]   Jackman, R. J.; Duffy, D. C.; Ostuni, E.; Willmore, N. D.; Whitesides, G. M., *Analytical chemistry* **1998,** 70, (11), 2280-2287

[199]  Auner, C.; Palfinger, U.; Gold, H.; Kraxner, J.; Haase, A.; Haber, T.; Sezen, M.; Grogger, W.; Jakopic, G.; Krenn, J. R., *Organic Electronics* **2010***,* 11, (4), 552-557

[200]  Auner, C.; Palfinger, U.; Gold, H.; Kraxner, J.; Haase, A.; Haber, T.; Sezen, M.; Grogger, W.; Jakopic, G.; Krenn, J. R.,. *Organic Electronics* **2009,** 10, (8), 1466-1472.